

RESEARCH TRIANGLE INSTITUTE

N 7 3 3 2 7 3 9

NASA CR-132310

STUDY OF METEOROID DETECTION SYSTEMS
APPLICABLE TO THE OUTER PLANETS MISSIONS

By

A. D. Brooks
C. D. Parker
Research Triangle Institute

Dr. L. K. Monteith
North Carolina State University

**CASE FILE
COPY**

Prepared under Contract No. NAS1-11692
RESEARCH TRIANGLE INSTITUTE
Research Triangle Park, N. C.

for Langley Research Center

NATIONAL AERONAUTICS AND SPACE ADMINISTRATION

ABSTRACT

This study has been concerned with the investigation and recommendation of modifications to the Pioneer 10/11 Meteoroid Detection Experiment to allow it to be used for Outer Planet Missions. Both pressurized cells and metal-oxide silicon (MOS) penetration detectors are considered. Both the sensors systems and the electronics are treated. Investigation of the calibration and characterization of the MOS penetration detector is reported.

TABLE OF CONTENTS

<u>Section</u>		<u>Page</u>
	LIST OF ILLUSTRATIONS	iv
	LIST OF TABLES	vii
I	INTRODUCTION AND SUMMARY	1
II	PRESSURE CELL MDE	3
	Pioneer 10/11 Configuration	3
	Outer Planets Thermal Considerations	6
	Response-Time Considerations	10
	Pressure Cell Instrumentation	10
	Fuse Characterization	13
	Magnetic Core Isolation	18
III	CAPACITOR (MOS) IMPACT DETECTOR MDE	23
	Impact Detector Characteristics	23
	Impact Detector Fabrication	25
	Impact Detector Instrumentation	29
	Conclusions	32
IV	CALIBRATION OF MOS DETECTOR	33
	Hypervelocity Micro-Particle Impact Experiments	34
	Sonic Micro-Particle Impact Experiments	44
	Micro-Particle Accelerators	44
	Vacuum-Operated Particle Accelerator	47
	Pressure-Operated Particle Accelerator	47
	Particle Suspension and Dispersion Methods	47
	Alumina Particle Generation Methods	54
	Methylene Blue Generation Methods	54
	Diocetylphtholate Generation Method	54
	NaCl Generation Method	54
	Electronic Readout Techniques	58
	Experimental Results and Analysis	58
	Fabrication of MOS Sensors Elements	58
	Experimental Design	60
	Interpretation of Data	63
	Threshold for MOS Discharge	74
	Conclusion	77
	REFERENCES	81
	APPENDIX A	83

LIST OF ILLUSTRATIONS (continued)

<u>Figure</u>		<u>Page</u>
19	Sketch Showing Capacitor Array Interconnection Details	28
20	Simplified Block Diagram of the Impact Detector Experiment	29
21	Simplified Block Diagram of the Capacitor-Type Impact Experiment	31
22	MOS Capacitor Discharge Characteristics When Biased at 60 Volts and Impacted by Hypervelocity Micro-Particles. (Data from MOS Units: 10,000 Å SiO ₂ - 500 Å Al, 10,000 SiO ₂ - 1000 Å Al, 10,000 SiO ₂ - 2000 Å Al, 10,000 SiO ₂ - 570 Å Au.)	38
23	MOS Capacitor Discharge Characteristics When Biased at 25 Volts and Impacted by Hypervelocity Micro-Particles. (Data from MOS Unit: 10,000 Å SiO ₂ - 2000 Å Al.)	39
24	MOS Capacitor Discharge Characteristic When Biased at 25 Volts and Impacted by Hypervelocity Micro-Particles. (Data from MOS Unit: 10,000 Å SiO ₂ - 1000 Å Al.)	40
25	MOS Capacitor Discharge Characteristic When Biased at 25 Volts and Impacted by Hypervelocity Micro-Particles. (Data from MOS Unit: 10,000 Å SiO ₂ - 500 Å Al.)	41
26	MOS Capacitor Discharge Characteristic When Biased at 25 Volts and Impacted by Hypervelocity Micro-Particles. (Data from MOS Unit: 4000 Å SiO ₂ - 2000 Å Al.)	43
27	MOS Capacitor Discharge Characteristic When Biased at 25 Volts and Impacted by Hypervelocity Micro-Particles. (Data from MOS Unit: 10,000 Å SiO ₂ - 570 Å Au.)	45

LIST OF ILLUSTRATIONS (continued)

<u>Figure</u>		<u>Page</u>
28	MOS Capacitor Discharge Characteristic When Biased at 32 Volts and Impacted by Hypervelocity Micro-Particles. (Data from MOS Unit: 4000 Å SiN_3 - 500 Å Al.)	46
29	Vacuum Nozzle Particle Accelerator	48
30	Sampling Rate of the Vacuum Nozzle Particle Accelerator	49
31	Air Stream Velocity of the Vacuum Nozzle Particle Accelerator	50
32	Pressure-Operated Particle Accelerator	51
33	Sampling Rate of the Pressure-Operated Particle Accelerator	52
34	Air Stream Velocity of the Pressure-Operated Particle Accelerator	53
35	Alumina Particle Size Distribution	55
36	Spray Gun Type Particle Dispersion Unit	56
37	Schematic Diagram of the Fluid Atomization Aerosol Generator	57
38	Schematic of the Recharge Pulse Detection Circuit	59
39	Cross Section of MOS Capacitor	61
40	MOS Array Micro-Particle Detector	62
41	Data Collection System	64
42	Histogram of Particle Distribution	66
43	Correlation Between Climet and MOS (1000 Å SiO_2)	72
44	Correlation Between Climet and MOS (1000 Å SiO_2)	73
45	Correlation Between Climet and MOS (700 Å SiO_2)	75
46	MOS Counts with Changes in Air Stream Velocity	76
47	Particle Distribution for Momentum Threshold Model	78

LIST OF TABLES

<u>Table</u>		<u>Page</u>
I	MOS Particle Detection Sensors	35
II	Calibration Data for MOS Units Impacted by Sonic-Velocity Micro-Particles	67

STUDY OF METEOROID DETECTION SYSTEMS
APPLICABLE TO THE OUTER PLANETS MISSIONS

By

A. D. Brooks

C. D. Parker

Research Triangle Institute

Dr. L. K. Monteith

North Carolina State University

SECTION I

INTRODUCTION AND SUMMARY

A Meteoroid Detection Experiment (MDE) has been developed for the Pioneer 10/11 Missions through the Asteroid Belt and to the vicinity of the planet Jupiter. The objective of the study discussed herein was to investigate and recommend modifications to the Pioneer 10/11 MDE which will allow it to be reliably used with either pressurized cells or capacitor-type detectors on interplanetary missions to the outer planets. At the time this report is being written, Pioneer 10 has completed its transit of the Asteroid Belt and is approximately nine months from Jupiter encounter. Pioneer 11 is beginning a similar journey, having been launched on April 5, 1973. The MDE deployed on Pioneer 10 has functioned as designed and provided much new data on the meteoroid environment in interplanetary space between Earth and Jupiter. Pioneer 11 carries a similar experiment. The characteristics of the Pioneer 10/11 MDE have been described, and the MDE has been demonstrated to be suitable for long-term deployment in interplanetary space (Refs. 1,2).

The limited weight and electrical power capabilities of the Pioneer spacecraft imposed weight and power restrictions on all spacecraft systems and experiments, and similar restrictions will apply to the outer planets missions. In order to meet the weight and power allocations for the Pioneer MDE, certain compromises were made in the MDE capabilities. These include a low response time that could result in inaccuracies under certain conditions and a significant loss of sensor area with each meteoroid penetration event. These compromises are likely to be less acceptable on a mission to the outer planets and should be circumvented as much as possible. Additionally, the thermal characteristics of the Pioneer 10/11 MDE pressurizing gas are unsatisfactory for planets beyond Jupiter and some thermal control is required. It is essential that any improvements in the MDE be achieved without significant weight and power penalties.

These investigations have yielded several modifications to the Pioneer MDE design that significantly enhance its applicability to the outer planets missions. Helium has been demonstrated to have suitable Paschen characteristics as a pressurizing gas, and its use is compatible

with the thermal environments of the outer-most planets. Thus, the added weight and/or power required for thermal control is circumvented through the use of helium. Changes in the transducer excitation circuitry that utilize space compatible, high reliability fuses and greatly enhance the response time of the MDE and also simplify the monitoring circuitry were investigated. To insure that some cells remain active throughout the mission, the Langley Research Center (LRC) has developed a retractable bumper to shield a pressure panel until the bumper is released to expose the panel during a later portion of the mission profile.

The capacitor-type, meteoroid impact detectors such as deployed on the MTS and other earlier, earth orbiting spacecraft have been further developed. These detectors have the advantage of increased sensitivity, and the loss of sensor area with each meteoroid impact is negligible. Further development of these detectors is continuing; however, electronic circuitry for monitoring these detectors has been designed.

SECTION II

PRESSURE CELL MDE

Pioneer 10/11 Configuration

The Pioneer 10/11 MDE has been described in previous reports (Refs. 1, 2). It consists of 234 gas cells pressurized with a mixture of Argon and Nitrogen, and each pressure cell is instrumented with a pair of electrodes such that the pressurized cell-electrode assembly functions as a cold-cathode discharge tube. A suitable voltage is applied across the electrodes. The particular mixture of Argon and Nitrogen used to pressurize the cell was selected for its desirable Paschen characteristics over the temperature range of the Jupiter missions. A fully pressurized cell will not conduct current between the electrodes. However, when gas leaks from a penetrated cell to the vacuum of space, the cell pressure decreases until the cell "breaks down" or "fires" to conduct significant current. As the pressurizing gas continues to leak to the vacuum of space, cell pressure continues to decrease and cell conduction again becomes negligible. Figure 1 illustrates the Paschen characteristics of a hypothetical cold-cathode discharge tube and its exploitation as a meteoroid penetration detector. For a given gas, electrode geometry and finish, temperature, etc., the firing voltage of the tube varies with pressure as illustrated in Figure 1. If the pressure cell is sealed at P_1 and a voltage V_1 is applied across the electrodes, for example, no conduction occurs across the electrodes. If pressure decreases to P_{hi} as it will in a penetrated cell, the cell "fires" to conduct current. As pressure continues to decrease, the cell passes through the conduction region corresponding to V_1 until the pressure reaches P_{10} . At pressures below P_{10} , no further conduction can occur.

In addition to having suitable Paschen characteristics over the entire range of expected temperatures, other requirements are necessary for pressure cells to be useful in an MDE. It is important that the pressurizing gas not liquefy or freeze at the lowest possible temperature. As temperature decreases in a pressure cell, the gas pressure will also decrease in a predictable manner. Gas density in the cell will remain approximately constant, however, and gas density is a more reasonable abscissa for the Paschen curve than pressure. If the gas condenses to a liquid at some low temperature, the vapor pressure will continue to decrease with temperature in a manner that is known for most gases. However, it is not known how the Paschen characteristics are influenced by the gas condensing to a liquid; and a gas, a liquid, or both may occupy the vicinity of the electrodes. The gaseous region would be at a lower density, and the liquid region at a higher density. Because of the uncertainty of the characteristics of a liquefied cell, it is concluded that the possibility of its occurrence should be avoided or thoroughly investigated.

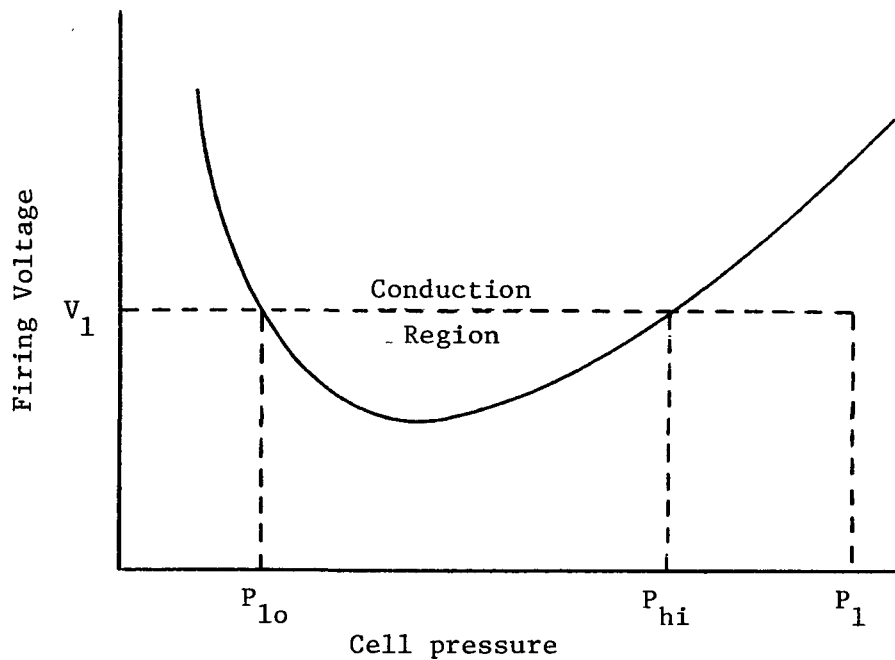


Figure 1. Paschen Characteristics of a Hypothetical Cold-Cathode Discharge Tube

It is necessary that the electronics limit the power that a conducting cell can dissipate. This was accomplished in the Pioneer 10/11 experiment by the relaxation oscillator circuit illustrated in Figure 2. Energy to fire a pressure cell was stored on the capacitor, and the $10^7 \Omega$ resistor restricted current to a value such that the pressure cell could not continue in a conductive state. When a cell "fired," the capacitor discharged through the conduction cell until it could no longer support conduction, and the conduction ceased. The capacitor then recharged until the cell could fire again. The recovery time or deionization time of the cell was negligible when compared with the recharge R-C time constant.

Weight allotted to the Pioneer 10/11 MDE was such that individual electrical leads between each of the 234 cells and the electronics unit in the spacecraft could not be afforded. To reduce the number of electrical leads to an acceptable number, the cells were connected into groups of paralleled cells. As illustrated in Figure 2, each oscillator circuit supplied 18 paralleled pressure cells. Moreover, several of the oscillator circuits were paralleled and monitored by one of two counters. Since many cells were connected in parallel and a penetrated cell could oscillate for

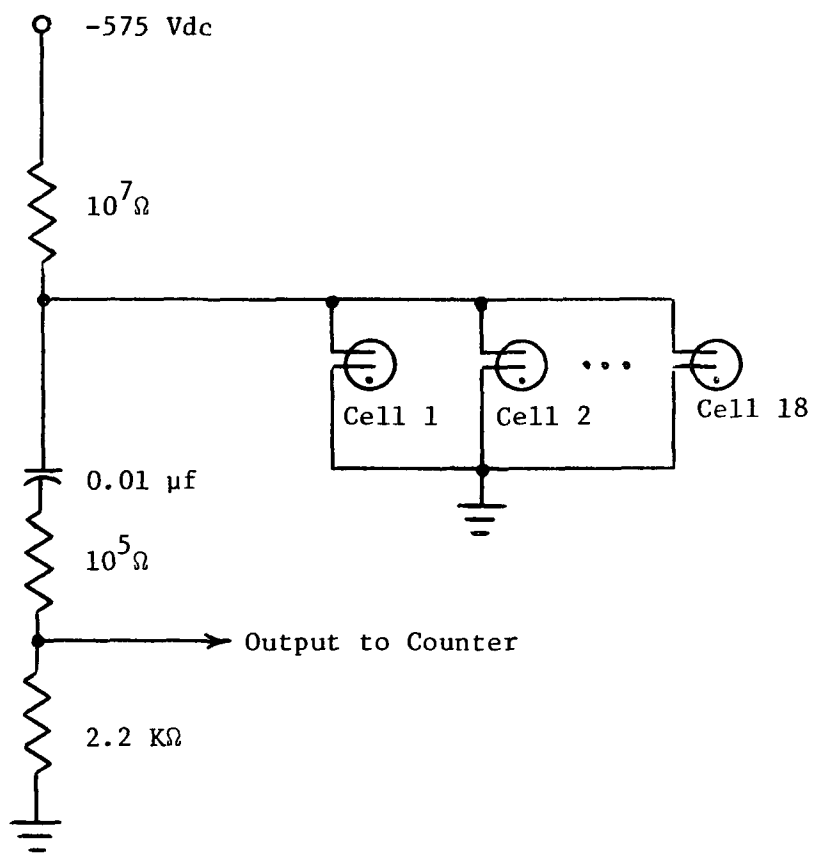


Fig. 2. Circuit for Energizing Pioneer 10/11 Pressure Cells

a long time, it was necessary for the electronic system that monitored the MDE to register the firing of a cell and essentially turn OFF for a preset period of time to ignore further firings of the same cell. Because many cells were paralleled and the electronic counters could not distinguish between paralleled cells, it was possible for the firing of a second cell to go undetected if it closely followed an earlier penetration. Furthermore, it was essential for the OFF time to be long compared to the probable oscillating time of a leaking cell. Otherwise, the still firing cell would erroneously register as a second penetration event. For Pioneer 10/11, this combination of factors restricted the response time--i.e., the OFF period of a counter--of the MDE to 84 minutes. This long response time is the Pioneer 10/11 compromise of most concern and is to be improved for the Outer Planets Missions.

Outer planets thermal considerations. - The thermal profile of a mission to the outer planets beyond the orbit of Jupiter will reach much lower temperatures than the Pioneer 10/11 missions. The low temperature extreme considered in the Pioneer 10/11 MDE design was the temperature of liquid nitrogen (-195°C), and the particular ratio of nitrogen to argon used to pressurize the MDE cells is such that the mixture remains gaseous at the reduced cell pressure corresponding to liquid nitrogen (LN_2) temperature. At some distance beyond Jupiter, temperatures below LN_2 will be encountered, and the Pioneer 10/11 MDE gas is likely to condense to a liquid. Consequently, it is essential that some thermal control be added to maintain the pressurizing gas above a minimum value or that another pressurizing gas be used. Since any thermal control system will increase weight and/or power requirements, the use of a different pressurizing gas is preferable. Of all the noble gases, helium (He) is the only gas likely to be suitable for an outer planets MDE. Consequently, the Paschen characteristics of the Pioneer 10/11 MDE cell with He as the pressurizing gas were investigated at room temperature and at LN_2 temperature. The experimental apparatus and procedures used for these investigations were identical to those used for the Pioneer 10/11 investigations and are described in Reference 1. The results of these investigations are summarized below.

Figure 3 includes all of the liquid nitrogen temperature data points for the Paschen characteristics of the Pioneer 10/11 pressure cells pressurized with He gas. These data are from multiple experiments on three separate transducers and were taken over a period of approximately three weeks. Figure 4 includes similar data for room temperature results. The data spread is comparable to that observed for the Pioneer 10/11 MDE gas and is due to the same causes, i.e., geometry variations, a rough finish on the electrodes, and the statistical nature of the firing process. This spread can be significantly reduced by controlling the geometry and polishing the electrodes, for example; however, the characteristics evident in Figures 3 and 4 are suitable for the outer planets MDE.

Figure 5 is an envelope that would include all of the room temperature and liquid nitrogen temperature data observed during these experiments, i.e., all of the data included in Figures 3 and 4. These results suggest

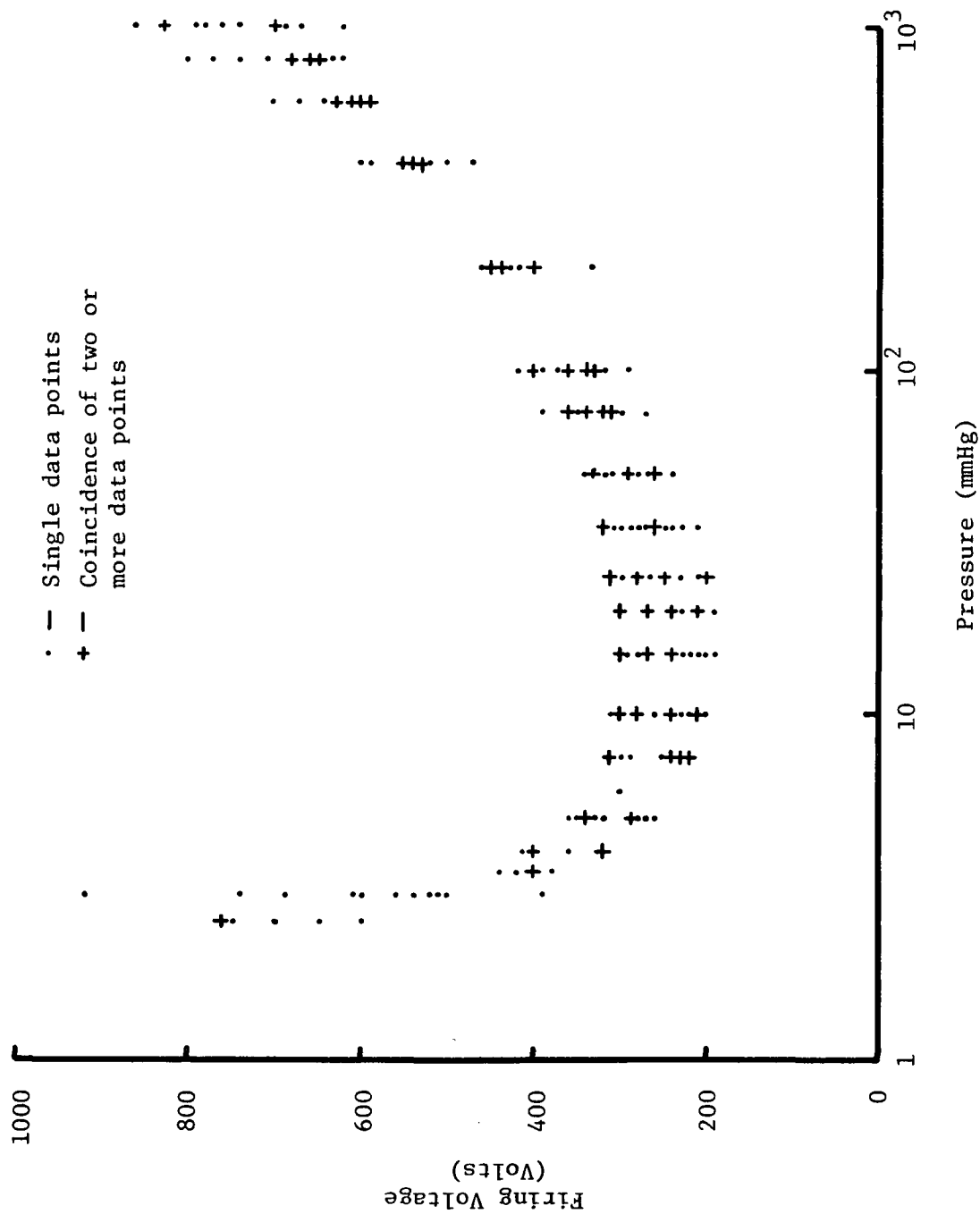


Figure 3. Liquid Nitrogen Temperature Paschen Characteristics of the Pioneer MDE Pressure Cell with Helium Gas

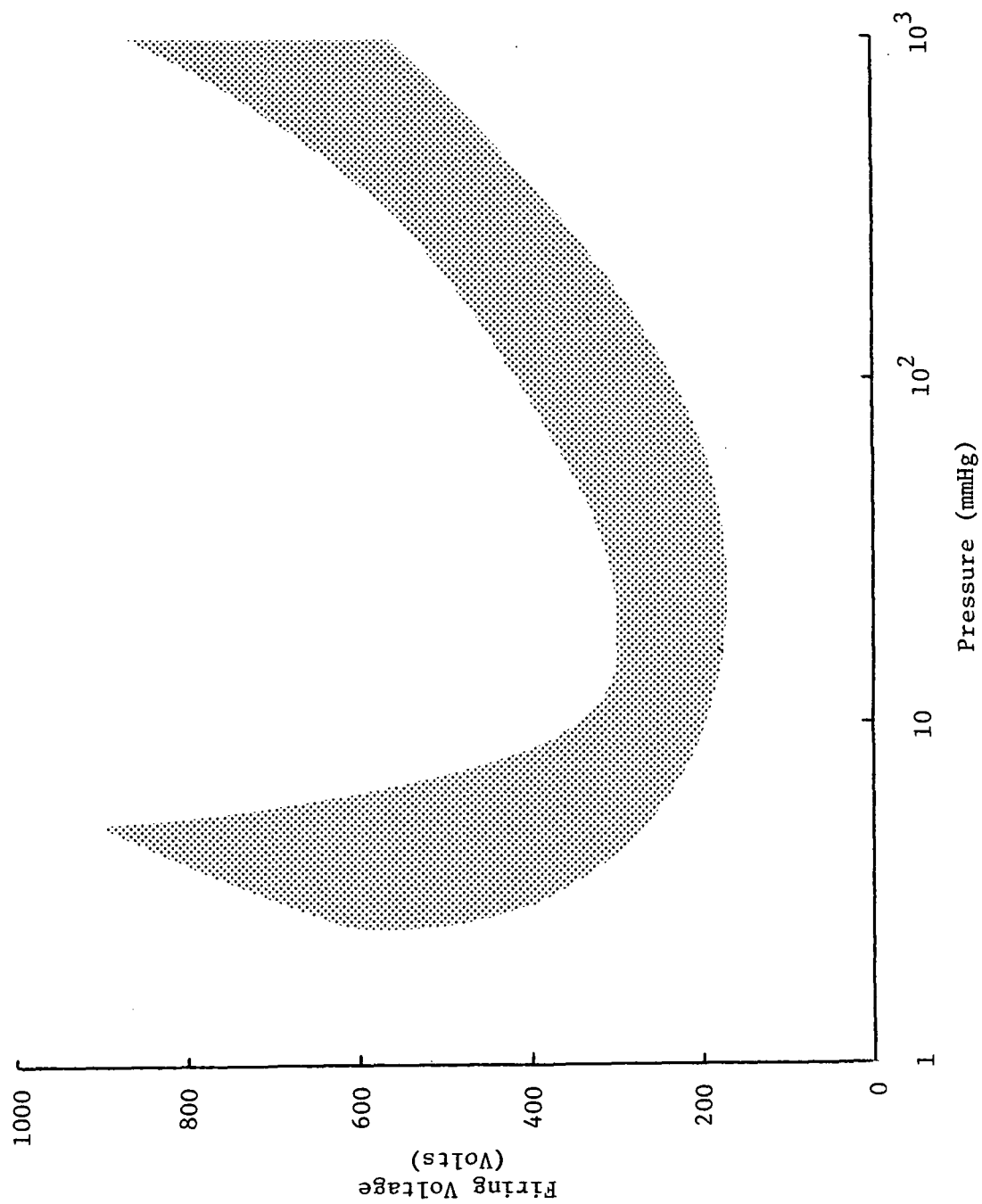


Figure 5. Envelope of All Paschen Curve Data at Both Room and LN₂ Temperatures

an initial sealing pressure of 1,500 mmHg (29 PSIA) and an excitation voltage of 400 Vdc, for example. There are other suitable combinations of voltage and pressure. Prior to a commitment to an outer planets mission, it would be necessary to extend the low temperature characterization of the pressure cells to temperatures below that of liquid nitrogen.

Figure 6 is the current-voltage characteristic of a helium filled pressure cell in the conductive region. The cell pressure was approximately 400 mmHg, and the temperature was room temperature.

Response-time considerations. - The 84-minute response-time characteristic of the Pioneer 10/11 MDE is an undesirable feature imposed by limited weight and power capabilities of the Pioneer spacecraft. Since many pressure cells are energized in parallel and gated to one of only two counters, it was necessary to cause a counter that detected an event to not count subsequent events in the paralleled cells until the cell that advanced the counter ceased to fire. Otherwise, a single penetration event could advance a counter many times (Ref. 1). What is required is a means of isolating a penetrated cell from paralleled cells such that the counter need not be turned OFF for a significant period of time.

The 84-minute response time (OFF time) of the Pioneer 10/11 configuration is a compromise between the probability of counting a single event twice and missing a count because the counter was OFF when the event occurred. The capability of registering several counts per minute is considered a reasonable design goal for the outer planets mission (Ref. 3).

The response-time of the pressure cell MDE will be determined by the associated instrumentation. The turn-ON (ionization) and turn-OFF (deionization) times of the cold cathode discharge sensor will be short relative to instrumentation time constants. Deionization times are typically hundreds of microseconds, for example, and ionization times are even shorter.

Pressure Cell Instrumentation

An instrumentation design for an outer planets, Pressure-cell MDE must reflect consideration of power, weight and volume allocation, and the number and type of spacecraft/MDE interfaces. The instrumentation design described in this section assumes that power, weight, volume, and interface allocations for an outer planet MDE will be limited and comparable to those for the Pioneer 10/11 Jupiter mission. The pressure panels/cells are assumed to be identical, except for the pressurizing gas, and the circuitry is also similar to the Pioneer 10/11 configuration. The design can be readily modified to accommodate any difference that may occur for a given outer planets mission. The objective in utilizing certain Pioneer 10/11 features--i.e., the Pressure panels--is to optimize the use of flight qualified hardware and minimize subsequent flight qualification activities.

The block diagram of Figure 7 illustrates the instrumentation required for an outer planets MDE. It is assumed that the spacecraft interfaces

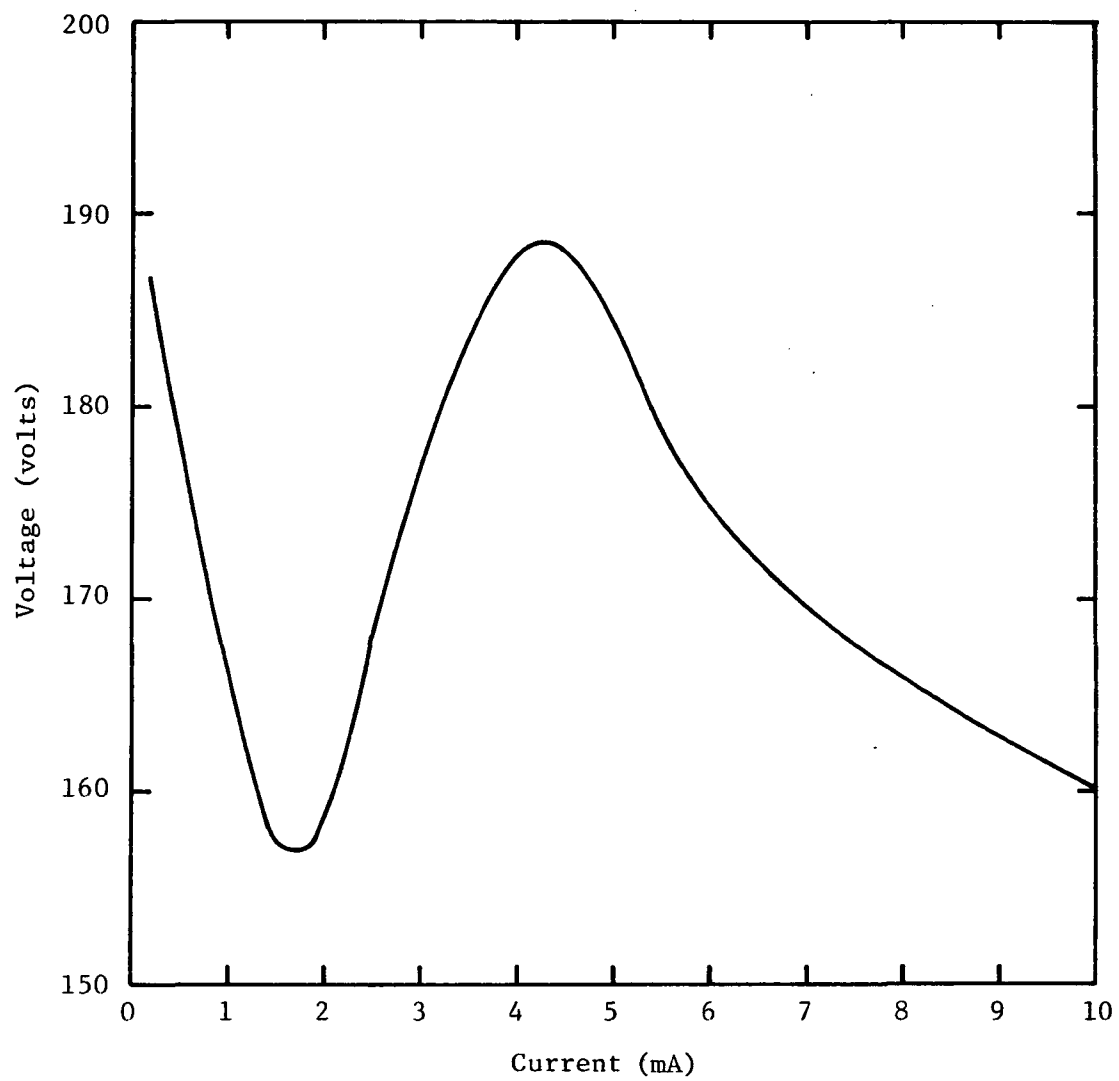


Figure 6. Current-Voltage Characteristics of a MDE Pressure Cell

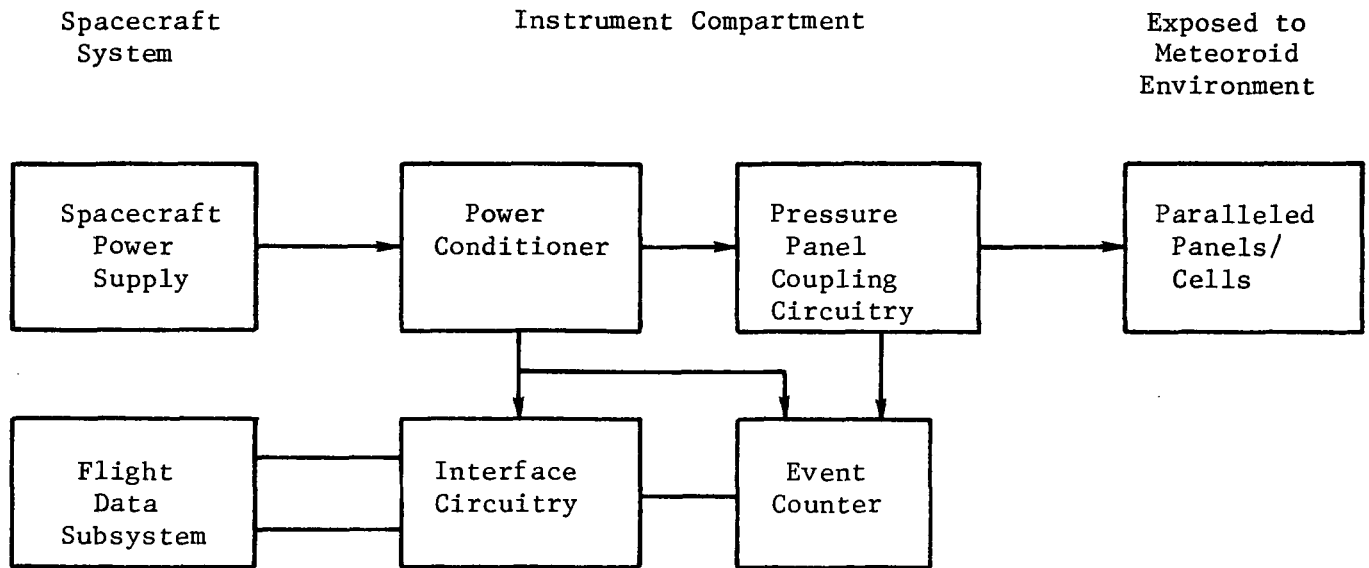


Figure 7. Conceptual Block Diagram of a Pressure Cell MDE.

will be similar to the Pioneer 10/11 interfaces--i.e., a single voltage supply will be provided by the spacecraft and a flight data subsystem will function to read-out the MDE data. A power converter changes the single voltage available from the spacecraft to the several levels required by the MDE and includes an ON-OFF feature controlled by spacecraft command. The power converter is very similar to the Pioneer 10/11 converter. The pressure panel coupling circuitry interconnects the pressure panels to the high voltage supply from the power converter and provides a signal to advance the event counter when a pressure cell is fired. For the outer planets missions, it is desirable that this circuitry function to isolate a pressure cell after its initial firing event but continue to monitor other pressure cells without interruption. This would eliminate the 84 minute OFF-time characteristic of the Pioneer 10/11 configuration and significantly enhance the MDE response time. The event counter is a simple recycling counter that does not include the time delay feature characteristic of the Pioneer counters, and the interface circuitry multiplexes the parallel counter outputs to the flight data subsystem as a serial word upon spacecraft command.

The MDE instrumentation design suggested herein differs from the Pioneer 10/11 configuration principally in the pressure panel coupling circuitry. This circuitry has been significantly altered to provide the outer planets MDE the desired time response. This circuitry is discussed in the following paragraphs.

Fuse characterization. - An ideal component for isolating a pressure cell that fires is a series fuse that opens during the initial firing of a pressure cell. It is desirable, if not essential, to locate the fuse at each pressure cell so as to avoid routing an individual wire to each pressure cell. The fuse would be exposed to extreme cold, to the vacuum of space, and to the shock and vibration characteristics of a space flight launch. It must reliably withstand this environment without open circuiting and reliably open during a single, pressure-cell firing event.

Fuses suitable for the MDE application are commercially available. One fuse recommended as suitable is a high reliability fuse used for a zero defects program. Its time-current characteristics are certified to 1% AQL by sampling according to MIL-STD-105, inspection level II. It is tested for shock, vibration, seal, and thermal shock by appropriate methods of MIL-STD-202. One such fuse, rated at 5mA, withstands MIL-STD-202 tests as follows: shock, high impact method 207A; vibration, 10 to 2,000 Hz at 10 G's, method 204A; thermal shock, -65°C to +125°C, method 107B, condition B. It is also tested for seal integrity; however, a sealed enclosure would not be desirable for an outer planets mission, and the fuse would purposely be caused to leak to the surrounding vacuum of space. A 2mA fuse is also available that differs from the 5mA fuse in that it is not tested to the high impact shock, method 207A. It is tested, instead, to 50 G's, method 202C. The lower current fuse is preferable provided its mechanical properties are suitable for a specific mission.

The circuitry illustrated in Figure 8 is suitable for the pressure panel coupling function illustrated in Figure 7. It is similar to the pressure-panel circuitry of Pioneer 10/11 except for the fuse in series with each cold-cathode sensor. Any convenient number of cells can be paralleled, and the circuit output can be OR-gated to a simple, recycling counter (i.e., without a time-delay feature). A large valued R_1 will isolate a faulty group of cells and limit power that can be drawn from the power supply. Energy stored on the capacitor must be sufficient to open the fuse during the first firing event of a pressure cell.

Figure 9 is a plot of the time-current characteristics of the 2mA and 5mA high reliability fuses discussed in a preceding paragraph. These curves represent the average total clearing time as a function of current at an ambient temperature of 25°C. (Prior to committing a fuse to a specific outer planets MDE, it will be necessary to determine a distribution of fuse clearing times for the MDE conditions.) Also included in Figure 9 are curves of estimated currents through a fuse as a function of time for different values of circuit parameters in Figure 8. These four curves were calculated for the following assumption: 1) A simple RC circuit was assumed in which the capacitor discharges through a fuse of

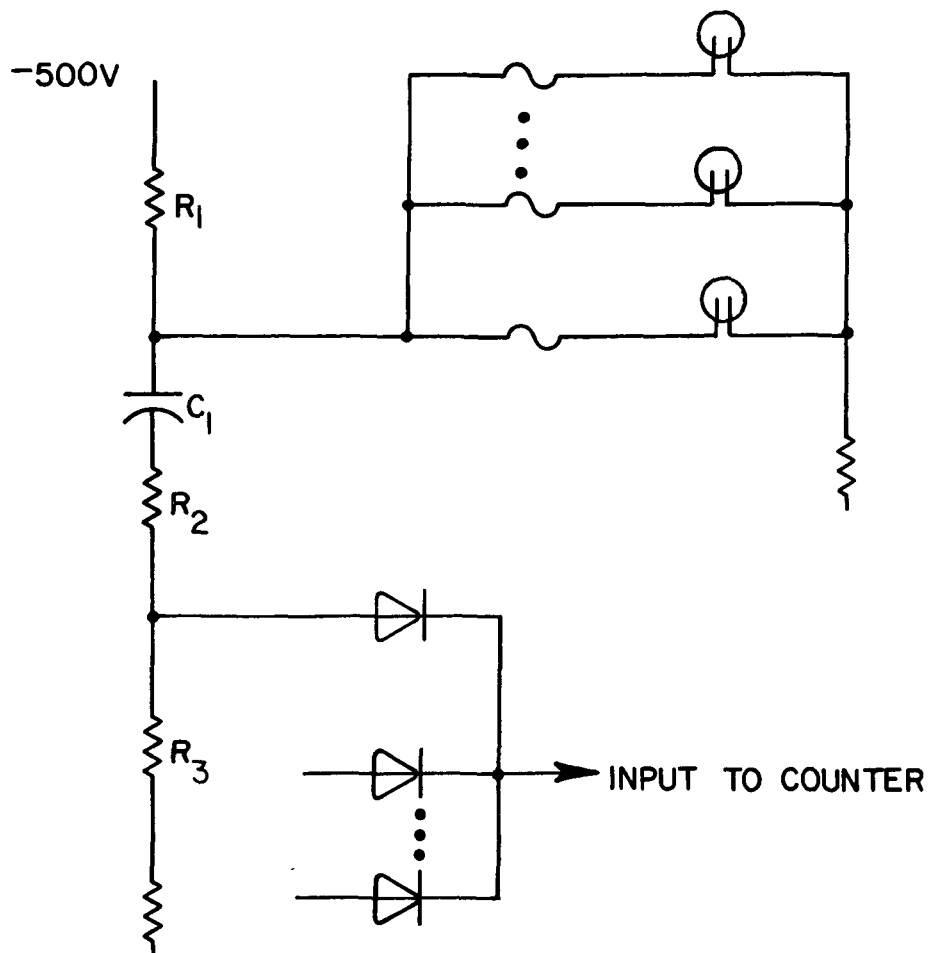


Figure 8. Pressure Panel Coupling Circuitry

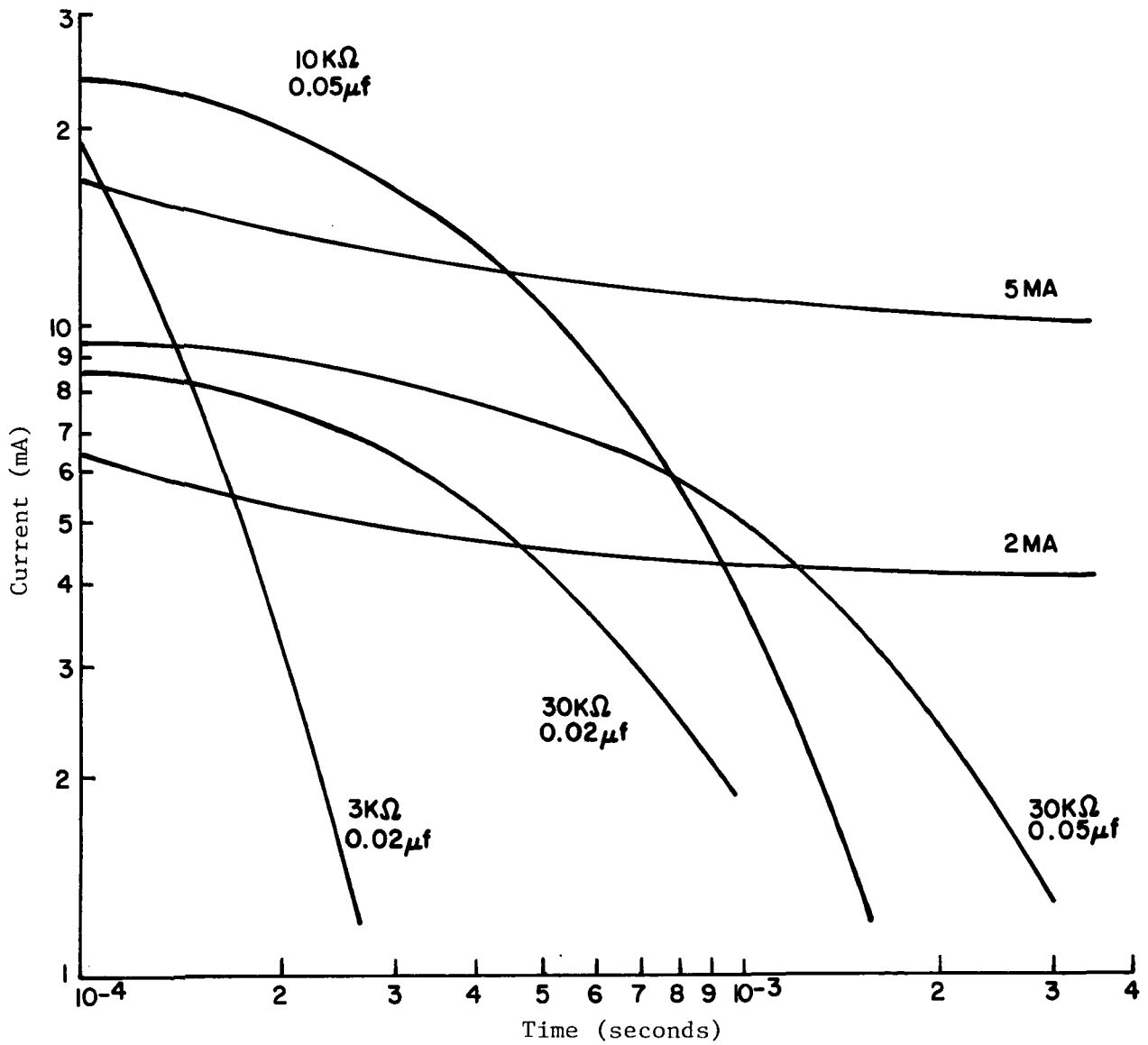


Figure 9. Time-Current Characteristics of the 2 mA and 5 mA High-Reliability Fuses and Fuse Currents Estimates for the Pressure Panel Coupling Circuitry.

negligible resistance and a fixed resistor, 2) no current contributions from the power supply was considered, and 3) a constant, 200 volt drop was assumed across the conducting, cold-cathode tube. (Measured values range from 155 to 190 volts; see Figure 6.) The parameter values included for each curve in Figure 9 correspond to values of R_2 plus R_3 and C_1 in Figure 8 and are reasonable values for an outer planets MDE.

If the circuit current exceeds a fuse time-current characteristic curve in Figure 9, that fuse should open when in series with a cold-cathode tube that fires. These considerations, as illustrated by the curves of Figure 9, lead to the conclusion that the pressure cells of an outer planets MDE can be fused.

A sample of the 5mA fuses were tested in the circuit configuration of Figure 8 at liquid nitrogen temperature. (The sample fuses were not the screened, high reliability units.) The specific circuit parameters were as follow:

Power Supply Voltage	500 volts
R_1	$10^7 \Omega$
R_2	$10^3 \Omega$
R_3	470 Ω
C	0.01 μ f.

The fuse and the cold-cathode tube were immersed in liquid nitrogen. The cold-cathode tube was initially pressurized with helium such that no conduction would occur at 500 volts. The pressure was caused to decrease until a firing event occurred, and the firing events were observed with oscilloscopes. Of seven fuses tested, six opened during the first 50 μ S of the first cold-cathode discharge or firing event. The seventh fuse opened during the second discharge event. These experiments further support the conclusion that the pressure cells can be reliably fused. However, additional investigations are required to characterize a specific fuse at lower temperatures, ascertain its compatibility with the launch and space environment, and finally, experimentally demonstrate the reliability of the fuse.

Figure 10 is a simplified block diagram of a pressure-cell MDE utilizing fuses to isolate a cell that fires. The redundancy scheme included in this illustration is by way of an example. The power converter, event counter, and spacecraft interface circuitry are redundant. This provides two independent systems with six detector panels interfacing with one system and another six detector panels interfacing with the other system. Each panel is interfaced through a parallel R_1 , C, R_2 network; and the outputs across the R_2 's are OR-gated to the event counter for that part of the experiment.

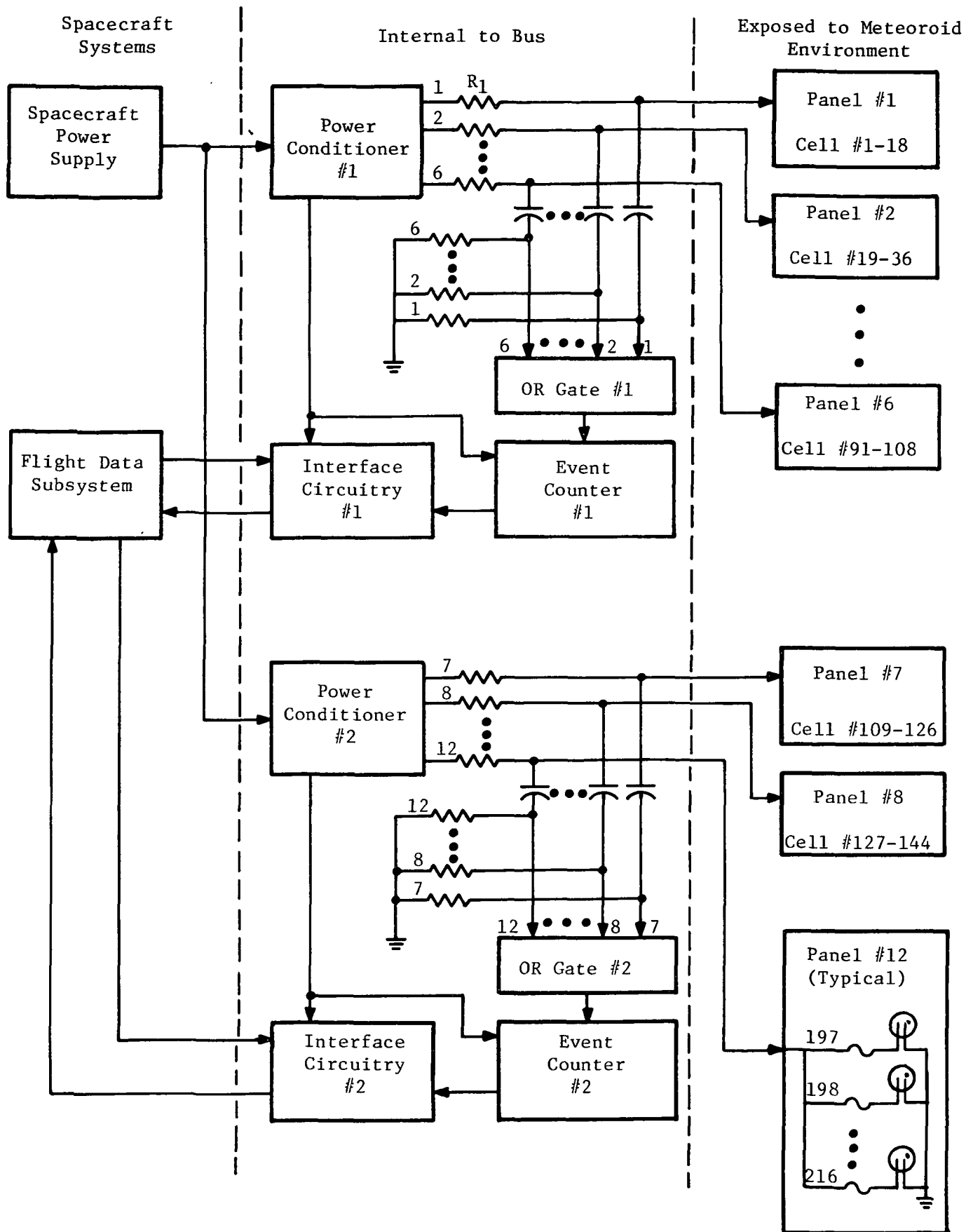


Figure 10. Simplified Block Diagram of the Pressure-Cell Meteoroid Penetration Experiment

The power conditioners, operating from the spacecraft power supply, charge the capacitors through the R_1 resistors. Additionally, they supply logic circuit voltages to the event counters and to the spacecraft interface circuitry. The event counters are recycling counters with parallel readouts. The interface circuitry multiplexes the event counter outputs to read out a serial word upon command from the spacecraft data system.

The energized system is dormant until a meteoroid penetration event occurs. When a pressure cell is penetrated by a meteoroid, the pressurizing gas leaks to the vacuum of space until the critical pressure corresponding to the excitation voltage is reached. At the critical pressure, a cold-cathode discharge occurs across the electrodes in the penetrated cell, and capacitor C discharges through the conductive cell. The discharge current yields an output signal across R_2 to advance the event counter, and the isolating fuse in series with the penetrated cell is caused to open by the discharge current. Resistor R_1 is high-valved so as to isolate the power conditioner from the discharge event and from any component failure beyond the R_1 -C node.

An outer planets MDE with a 5-ft^2 target area of 2-mil thick pressurized cells based on the design illustrated in Figure 10 would weigh approximately 2,400 gms (5.3 lb) including the bumper that shields the pressure cells during the early portion of the flight. The power required, assuming 54L logic, is approximately 500 mW.

Magnetic core isolation. - A tape-wound, square B-H loop core was briefly considered as a means of isolating a penetrated firing transducer from the event counter. This magnetic core isolation concept is illustrated in the circuit of Figure 11. Any number of pressure cells with series square-loop primary winding circuits can be paralleled. In this circuit, a transducer that fires allows the capacitor to discharge through the series primary winding. The discharge resets the previously set core, isolating the secondary from any subsequent firing events. The secondary windings are OR-gated to an event counter. It is necessary for the square-loop cores and the OR-gates (diodes) to be located with the pressure cell if the wiring harness is to be reasonable. Consequently, the cores have to function as square-loop units at very low temperatures for which they have not been characterized.

The B-H loop of a representative miniature, tape-wound, square-loop core was displayed in the circuit of Figure 12, and the results are shown in the oscillograms of Figures 13 and 14. Figure 13 is a room temperature B-H loop, and Figure 14 is a liquid nitrogen temperature loop. It is observed that the residual flux density decreases by approximately 8.5% and the coercive force increases by approximately 15% at liquid nitrogen temperature. The loop remained reasonably square, and should function satisfactorily. These investigations were not completed in view of the obvious superiority of the fuse as an isolating device.

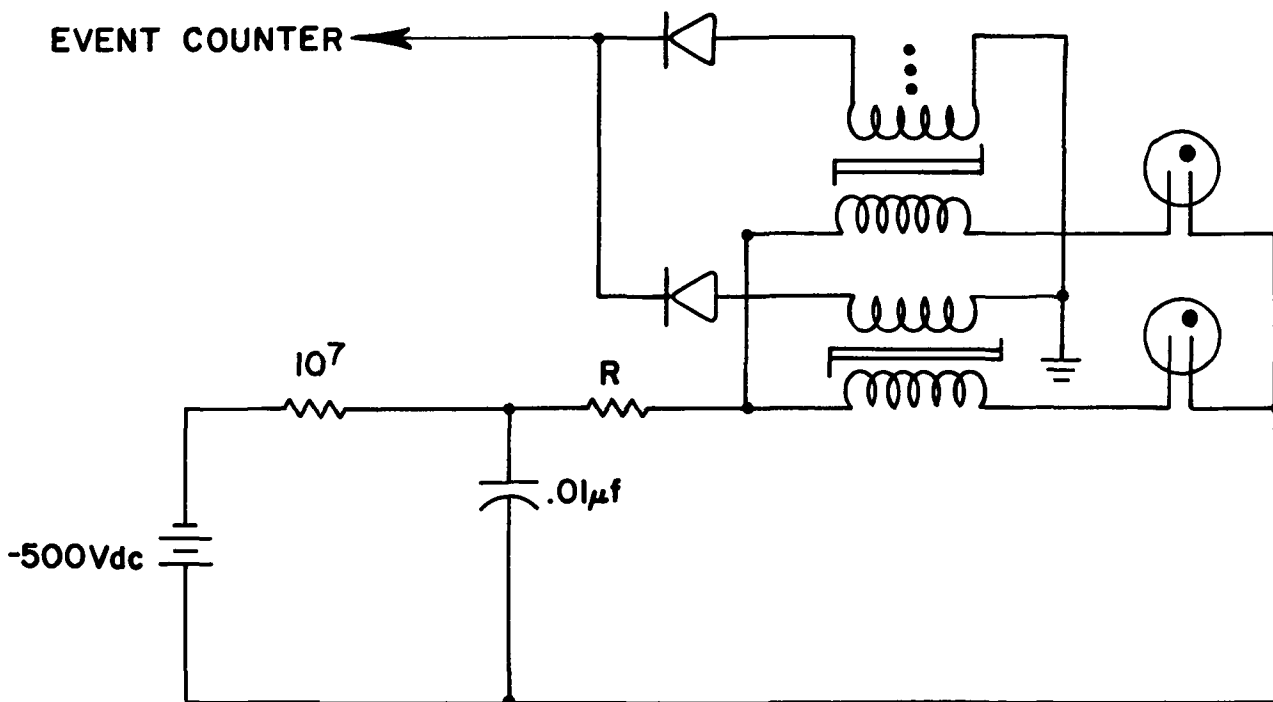


Figure 11. A Conceptual Illustration of the Use of a Square-Loop Core for Isolating a Firing Pressure Cell

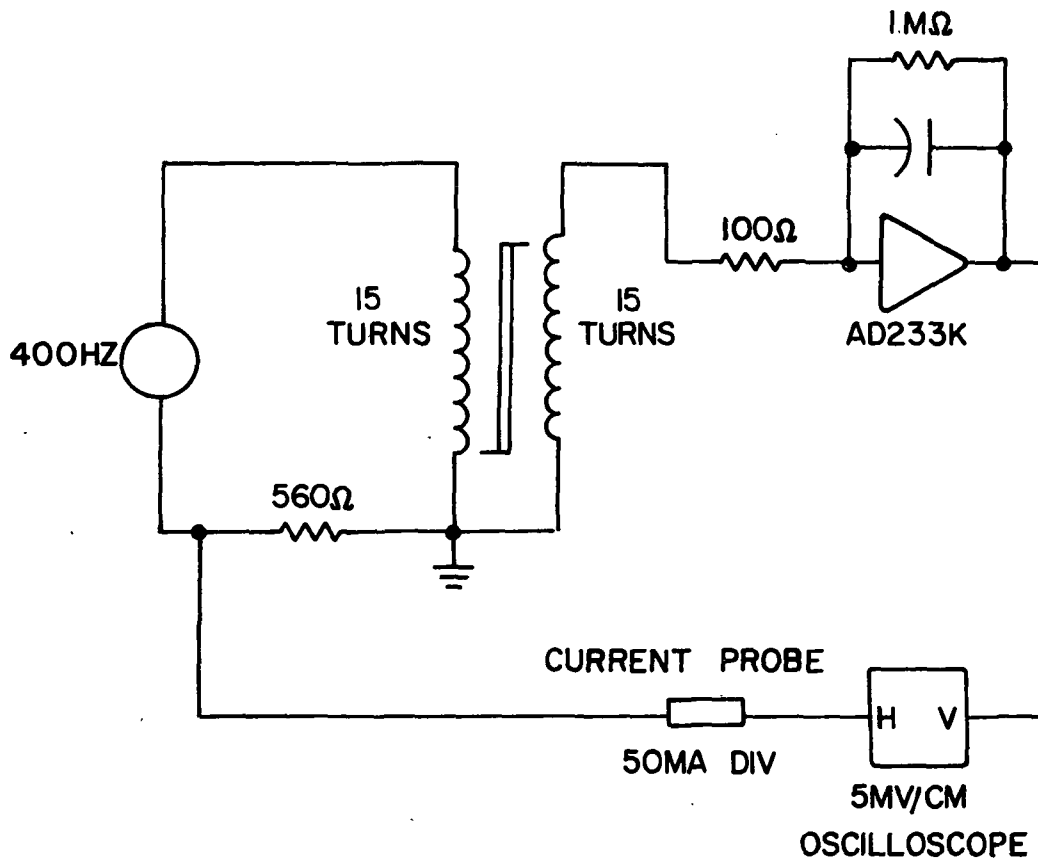


FIG. 12 Circuit for displaying the B-H Characteristics of Magnetic Core.

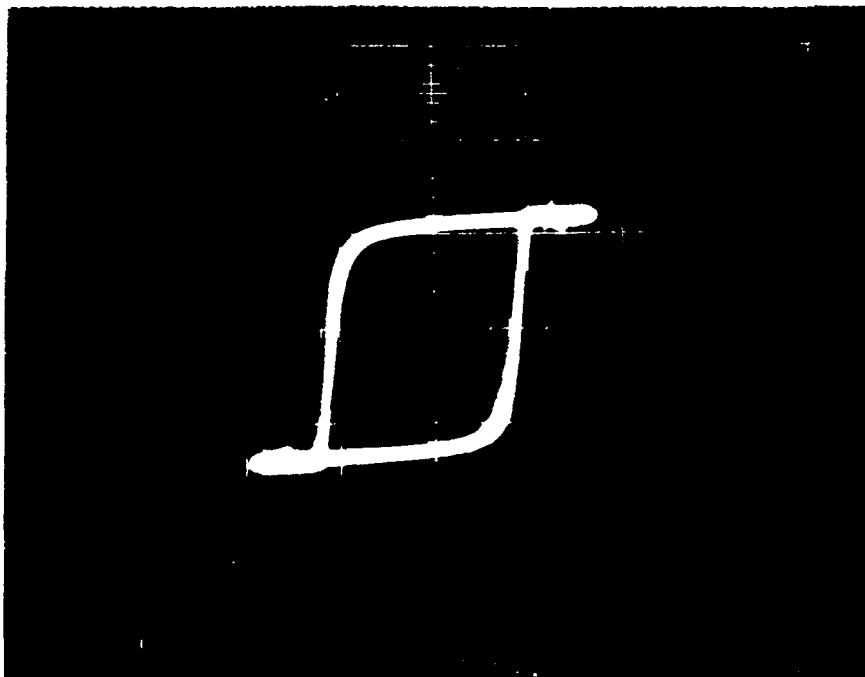


Figure 13. B-H Loop of a Minature, Tape-Wound Core at Room Temperature

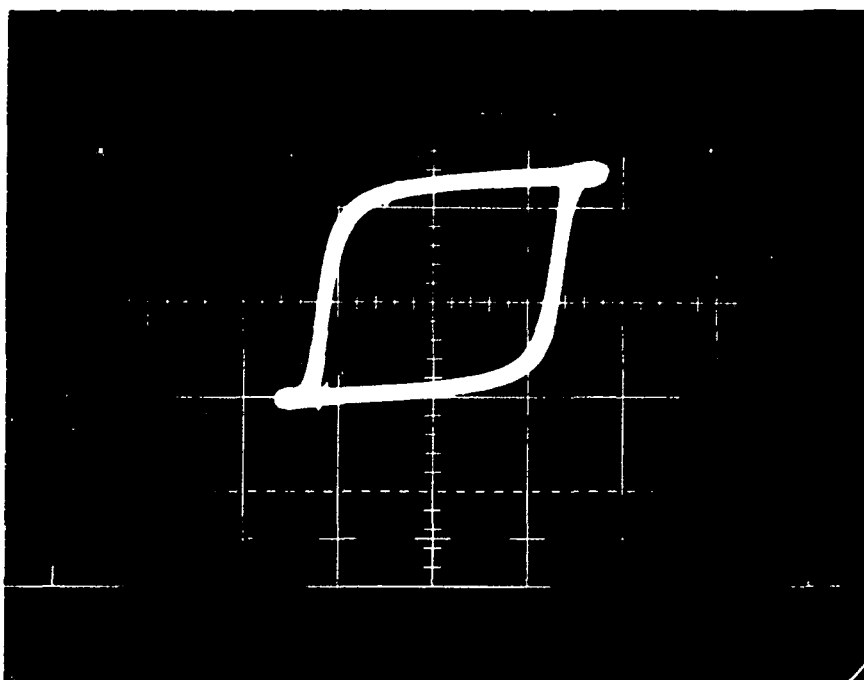


Figure 14. B-H Loop of the Tape-Wound Core of Figure 13 at LN_2 Temperature

SECTION III

CAPACITOR (MOS) IMPACT DETECTOR MDE

Capacitor-type impact detectors are also suitable for an outer planets MDE. Like the pressure cell MDE, the capacitor impact detector MDE has been previously flown. The detectors are metal-oxide-silicon (MOS) capacitor structures. A meteoroid impact on the capacitor causes an electrical discharge across the oxide at the point of impact. The stored energy causes the damaged region to clear, and the capacitor recharges. The recharge current is detected in associated circuitry and recorded as an impact event. The capacitor-type detectors differ significantly from the pressure cell detectors in that they will detect much smaller particles (to 10^{-15} gms) and they are self-clearing such that there is no significant loss of detector area with each impact.

Impact Detector Characteristics

Figure 15 illustrates the detailed structure of the MOS capacitor. The silicon substrate (back-electrode), the thermally-grown oxide (SiO_2 dielectric) and the evaporated aluminum front electrode are all evident in the figure. The dimensions correspond to those of MOS structures fabricated during these investigations (the drawing is not to scale) and the battery and resistor are included for illustration purposes.

Tests have shown that the applied field across the capacitor should be approximately 10^6 volts/cm. Manufacturing processes have been developed which yield large area dielectrics which will withstand the high field. This process includes electrical burn-in at fields greater than the operating field.

When the capacitor is impacted, the electrical signal observed across the recharging resistor has a very sharp rise time (in the microsecond range). The magnitude of the voltage is determined by the energy drained from the capacitor during the discharge. From the peak recharge current and voltage, a typical R-C recharge is observed where the time constant is determined by the recharge resistor and the MOS capacitor. For a 4000 Å SiO_2 dielectric, the applied voltage is typically 40 volts for a field of 10^6 volts/cm. The discharge voltages are usually 50 to 90% of the applied voltage. Each capacitor (3.8 x 3.8 cm and 4000 Å SiO_2) will have a capacitance of 10^{-7} farads. The capacitor will detect particles in the low mass range from 10^{-12} to 10^{-15} gms with velocities near 10 kilometers per second. The impact energy is much less than the electrical energy stored on the capacitor, and the discharge is initiated by partial penetration and mechanical damage which reduces the electrical field strength

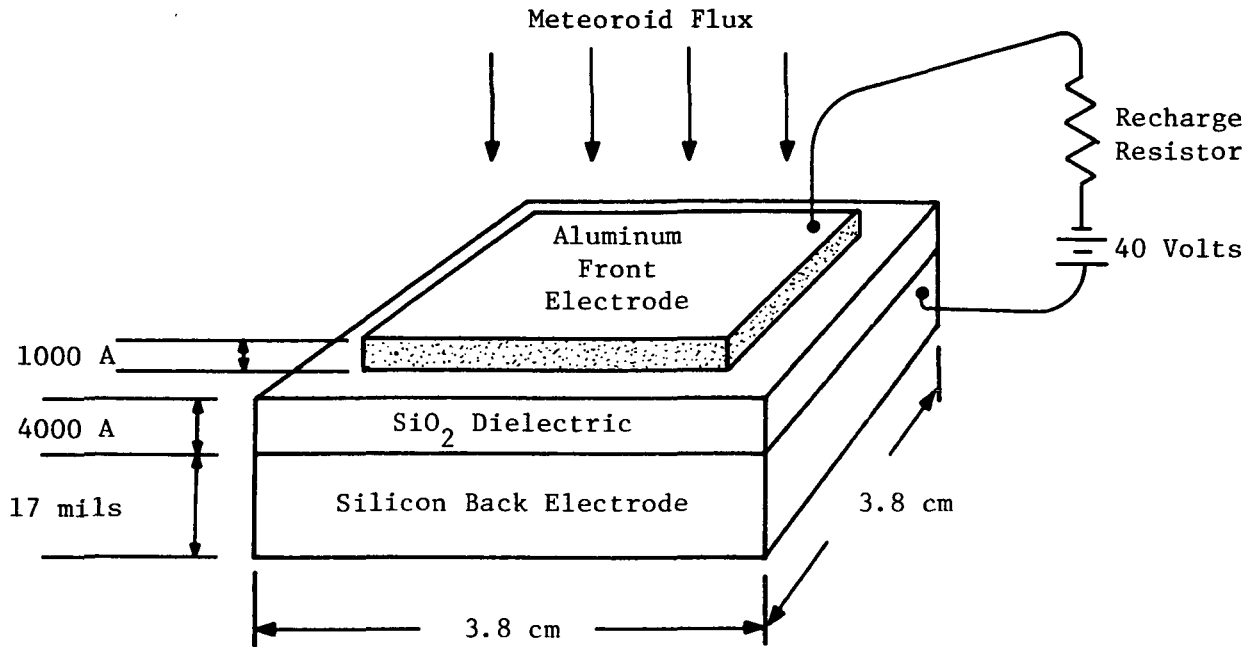


Figure 15. Sketch of Capacitor Impact Detector

of the dielectric under the impact. The reduced field strength of the dielectric coupled with the crater of the impact which increases the field in this region initiates an electrical discharge. The much larger electrical energy vaporizes the electrode and the dielectric in a small area around the impact point. Optical inspection shows electrical and/or thermal damage extending for several projectile diameters from the point of impact. The damaged region is circular and appears to be recrystallized or solidified SiO_2 which results from the conduction of heat away from the impact and electrical discharge region. The threshold for the transduction of the mechanical impact to an electrical discharge occurs over a velocity mass relationship as shown in Figure 16. These results verify that the capacitor will function as a cumulative counter of micrometeoroid impacts in the low mass range. At higher mass or larger diameter particles near 1 mil, the MOS capacitor behaves as a penetration detector. The particles penetrate into the silicon resulting in brittle fracture of the substrate. However, the electrical discharge signal is identical to the signal for smaller particles.

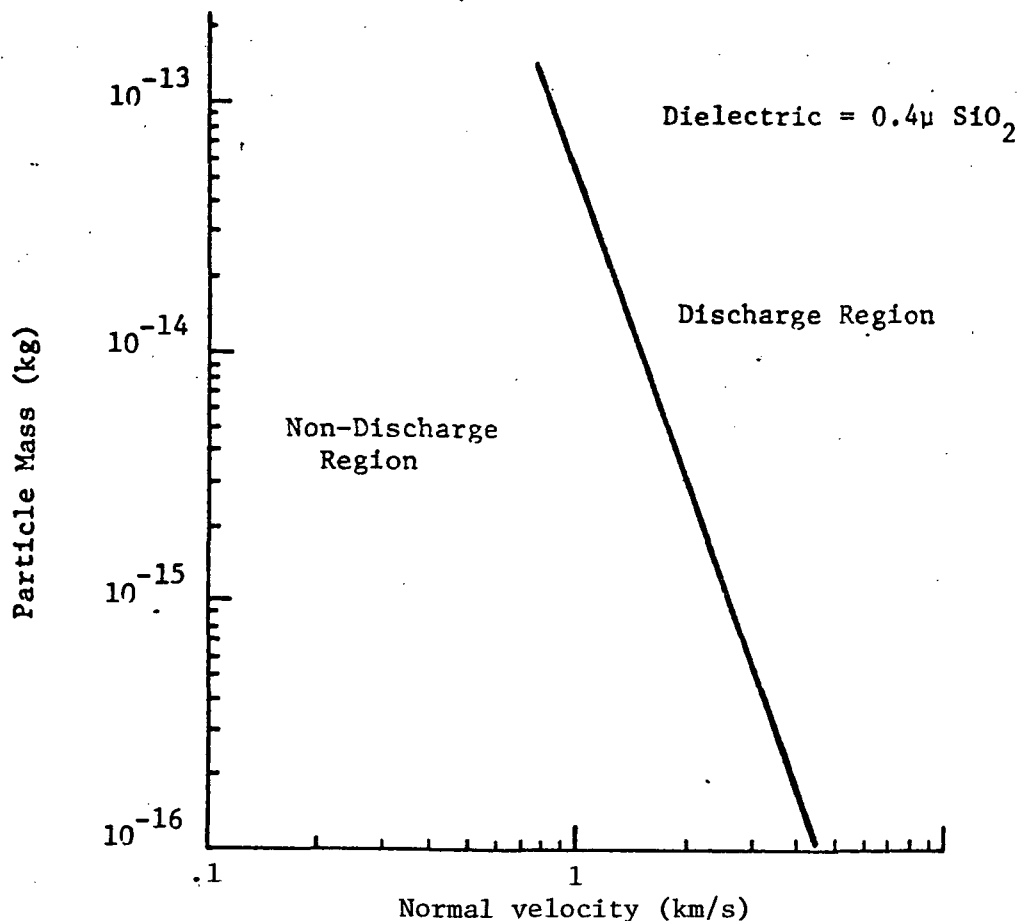


Figure 16. Impact Detector Calibration Curve

Impact Detector Fabrication

The capacitor-type detectors are fabricated from standard semiconductor fabrication procedures. Individual capacitors are fabricated on commercially available silicon wafers by growing a thermal oxide on the wafer and depositing an aluminum front electrode over the thermal oxide dielectrics. The starting silicon is typically low resistivity, e.g., $0.1 \Omega \text{ cm}$, p-type, large diameter wafers. The wafers are sawed into squares, polished, and thermally oxidized to provide the desired dielectric thickness.

To achieve a large detector area, a capacitor array analogous to a solar panel can be utilized. An epoxy-glass printed circuit board, for example, can provide a light-weight mount for electrically isolating the capacitor and for mechanical mountings, and standard thermal compression (TC) bonding is utilized for electrical connections.

Figure 17 is a photograph of an impact detector panel consisting of a 4×4 array of MOS capacitors. This was fabricated as a prototype of a detector panel suitable for an outer planets mission. The individual MOS structures were fabricated on 17 mil thick wafers, 5 cm in diameter. These were sawed into $3.8 \times 3.8 \text{ cm}$ squares. The thermal oxide dielectric is 4000 Å thick, and the aluminum front electrode as well as a back contact

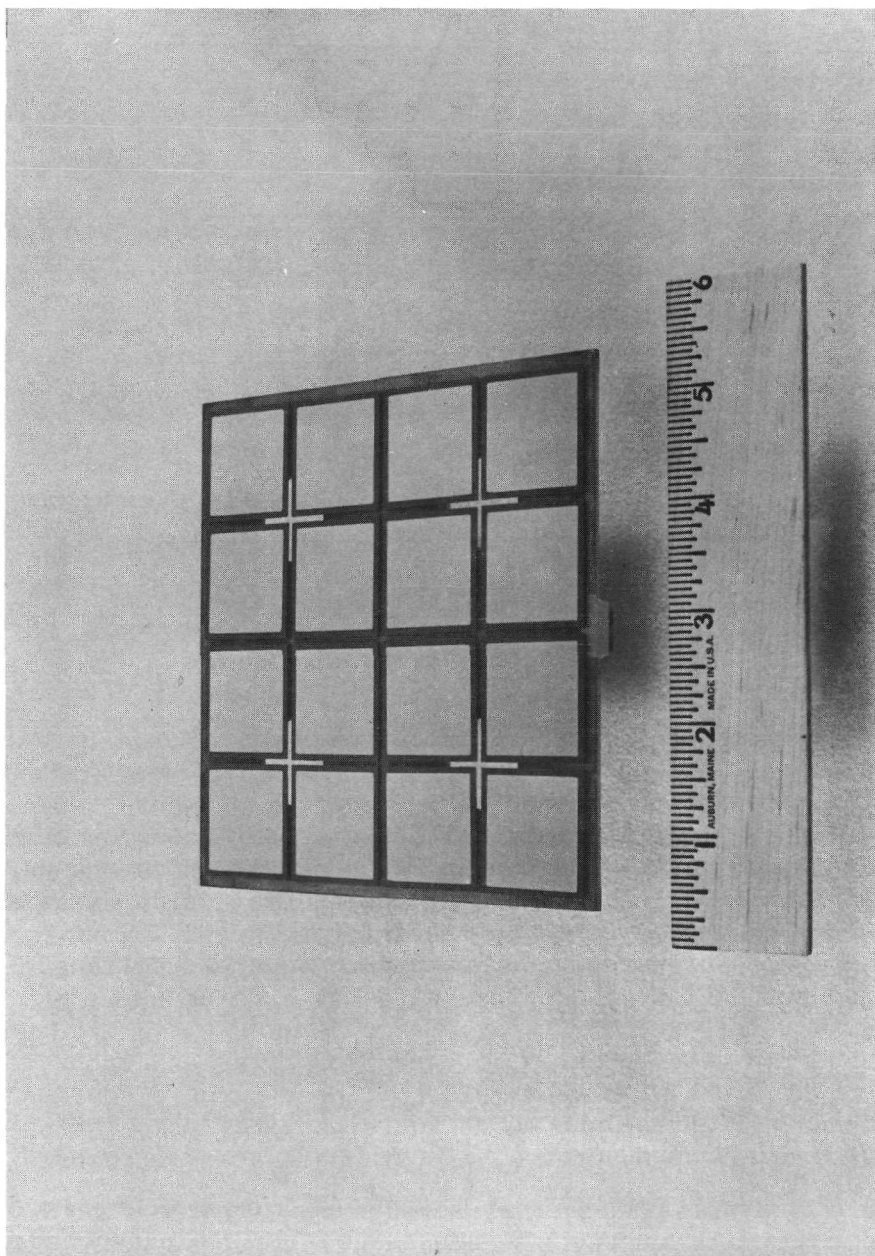


Figure 17. Photograph of an Impact Detector Panel

area are 1000 \AA , thermally evaporated aluminum. The individual MOS structures are arrayed on copper-coated epoxy-glass printed circuit board that provides for mechanically mounting and interconnecting the capacitor to monitoring instrumentation. Figure 18 shows additional detail of the capacitor mounting, and Figure 19 is an illustration of the backside of the panel array showing interconnection details. Four backside contacts are made through each of four holes in the printed circuit board. The resistors shown are part of the instrumentation circuitry. This prototype panel was delivered to LRC for experimental evaluation.

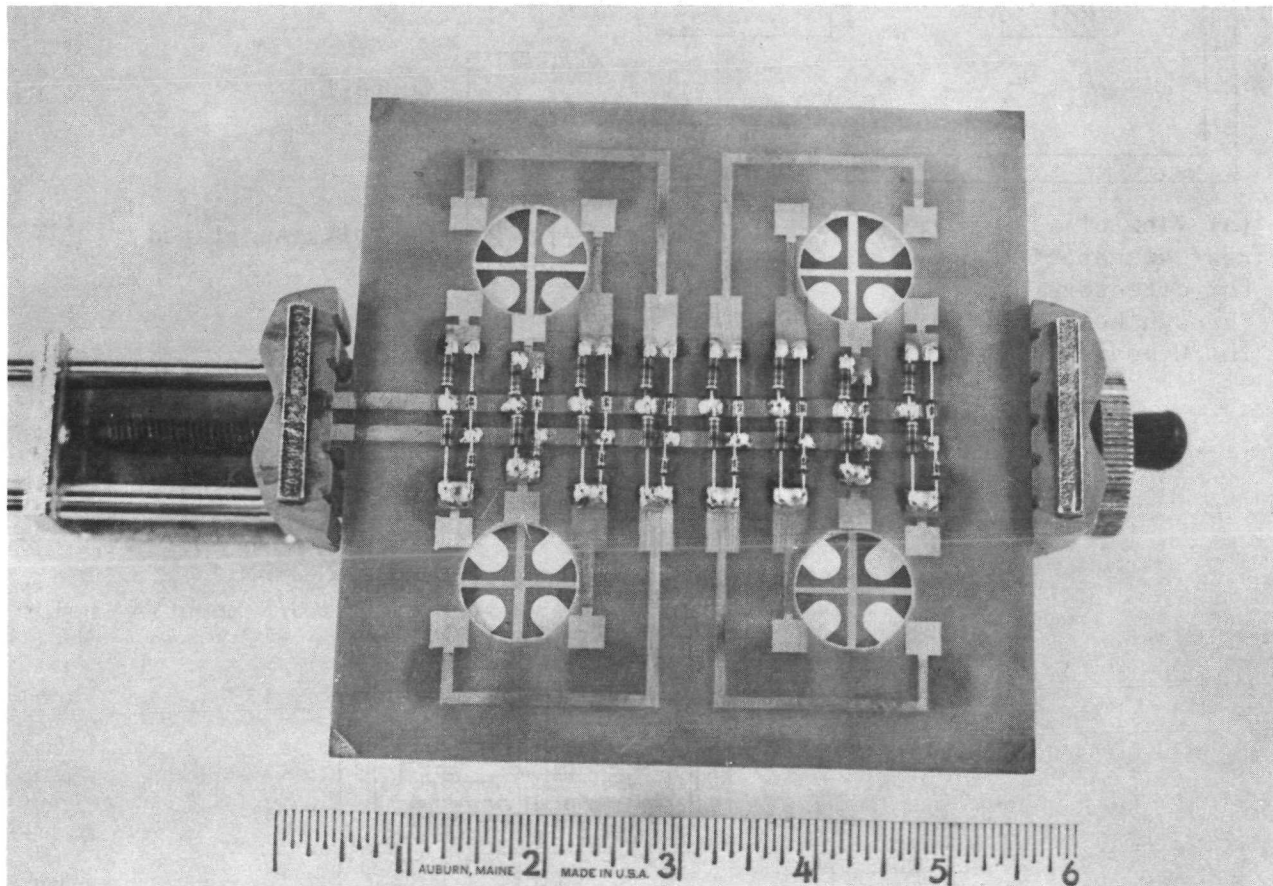


Figure 18. Photograph of the Backside of the Impactor Detector Panel Showing Interconnection Details

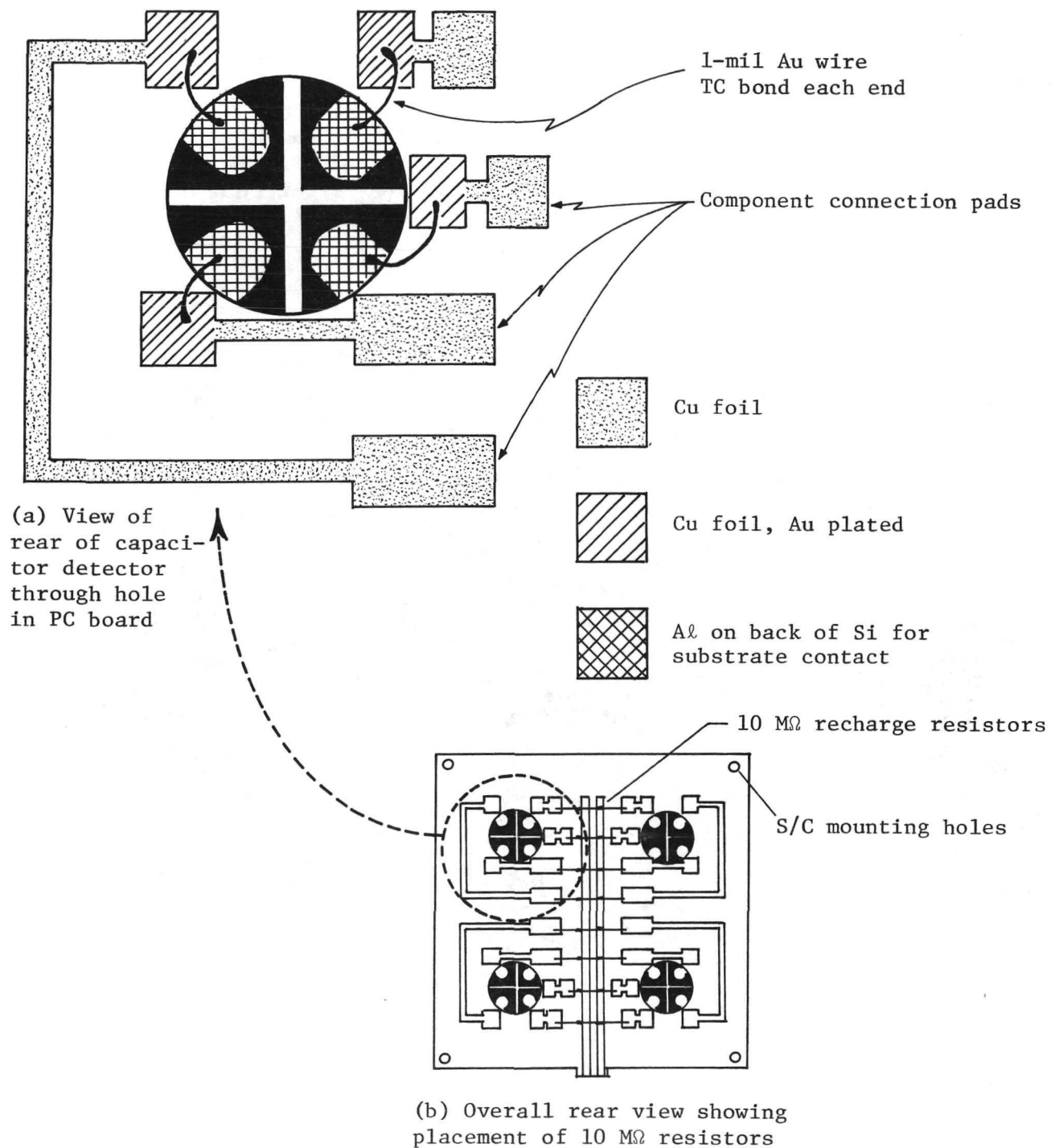


Figure 19. Sketch Showing Capacitor Array Interconnection Details

Impact Detector Instrumentation

Instrumentation requirements for the impact detector are extremely simple. Figure 20 is a simplified block diagram of a capacitor-type MDE. A power conditioner supplies all of the voltage requirements of the experiment, i.e., logic level voltages to the electronics and a 40 volts bias voltage to the capacitor detectors (assuming a 4000 Å dielectric).

Each capacitor in the array is biased through a series resistor, $R_1, R_2 \dots, R_4$. In the event of a meteoroid encounter, the impacted capacitor discharges, clears itself as the discharge occurs, and recharges through the series resistor. The recharge current also flows through a 1 MΩ resistor in the instrument compartment causing a voltage drop at node N_1 . This voltage drop is coupled to an event counter and recorded as a meteoroid encounter. The event counters are recycling counters with parallel outputs, and the interface circuits multiplex the parallel counts from the two counters to the spacecraft data subsystem as serial words.

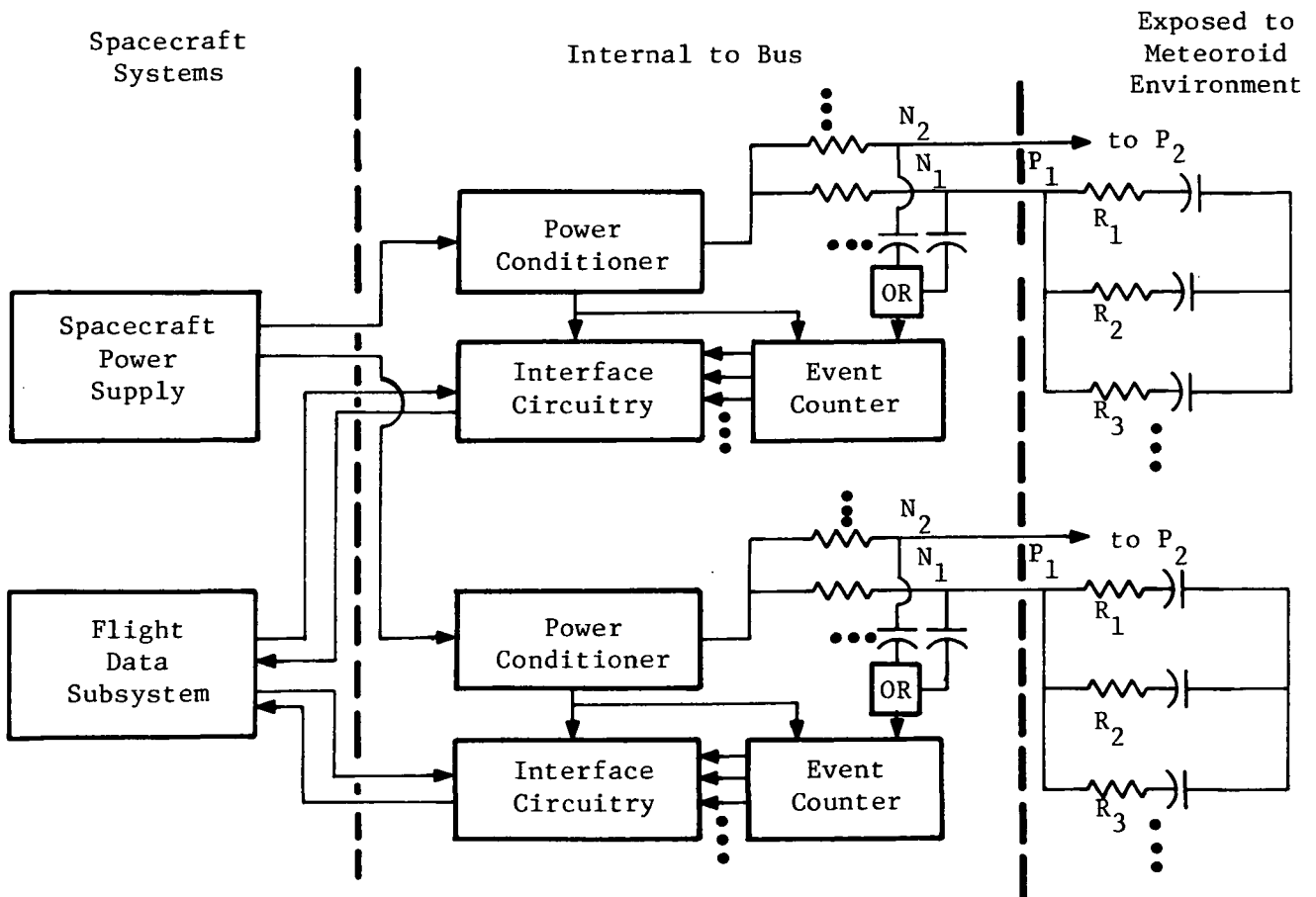


Figure 20. Simplified Block Diagram of the Impact Detector Experiment

The value of the capacitor and the series resistor determines the response time for the capacitor-type experiment. If the series resistors are $10\text{ M}\Omega$ and the capacitors are 10^{-7} farads, a single capacitor can respond to a meteoroid encounter every five seconds or less. The $10\text{ M}\Omega$ series resistors will also isolate any capacitor that fails in a shorted mode and will prevent it from compromising the remainder of the target area. An analog signal indicative of steady-state current from the power supply, e.g., a first order integration of the voltage at N_1 , will provide a measure of any area lost because of a shorted capacitor.

Figure 21 is a block diagram of a capacitor-type MDE with 22 detector panels, each panel consisting of a 4×4 array of detectors as illustrated in Figure 17. This provides a total detector area of approximately 0.5 m^2 . In this example, two redundant electronic systems are used to instrument a group of eleven panels each.

Each of the two groups of detector panels is supplied from a single power conditioner in the electronic chassis. Impact events on either of the two groups are registered in an associated counter and subsequently interfaced to the spacecraft telemetry system as illustrated. Each event counter is a recycling, 1024 bit counter (10 binaries), and the 10 parallel outputs are multiplexed to the spacecraft data subsystem serially upon command. The length of the proposed counter is a compromise between exceeding the capacity of the counter and increasing the number of binaries (with the attendant weight and power penalties) and also the length of the serial word to be read to the spacecraft. For the electronic configuration illustrated, the chassis and enclosed electronics would require approximately 330 cm^3 , weight approximately 700 grams, and dissipate approximately 500 mW (assuming 54L logic). The panels will weigh approximately 140 gms and dissipate negligible power. Each interface circuit will require a word-gate and bit-rate from the spacecraft data subsystem and will read-out a 10-bit serial word upon bit-rate commands. There are numerous modifications to this proposed configuration that would be satisfactory and would not significantly alter the weight and power requirements.

The capacitor-type MDW places no special requirements on the spacecraft telemetry or on the data acquisition duty cycle. The two, ten-bit serial word readouts would be adequate, for example, if the experiment were interrogated on a cycle of several hours. If interrogated more frequently, the serial word could be reduced in length. As proposed, the experiment requires word-gate and bit-rate commands for each of the two counters. The electronics will function without any temperature control over a temperature range of -55°C to $+125^\circ\text{C}$, and detectors will function over a much wider range. There are no data storage requirements external to the electronics. The experiment should present no special problems or requirements such as RFI or magnetic interference or special data requirements.

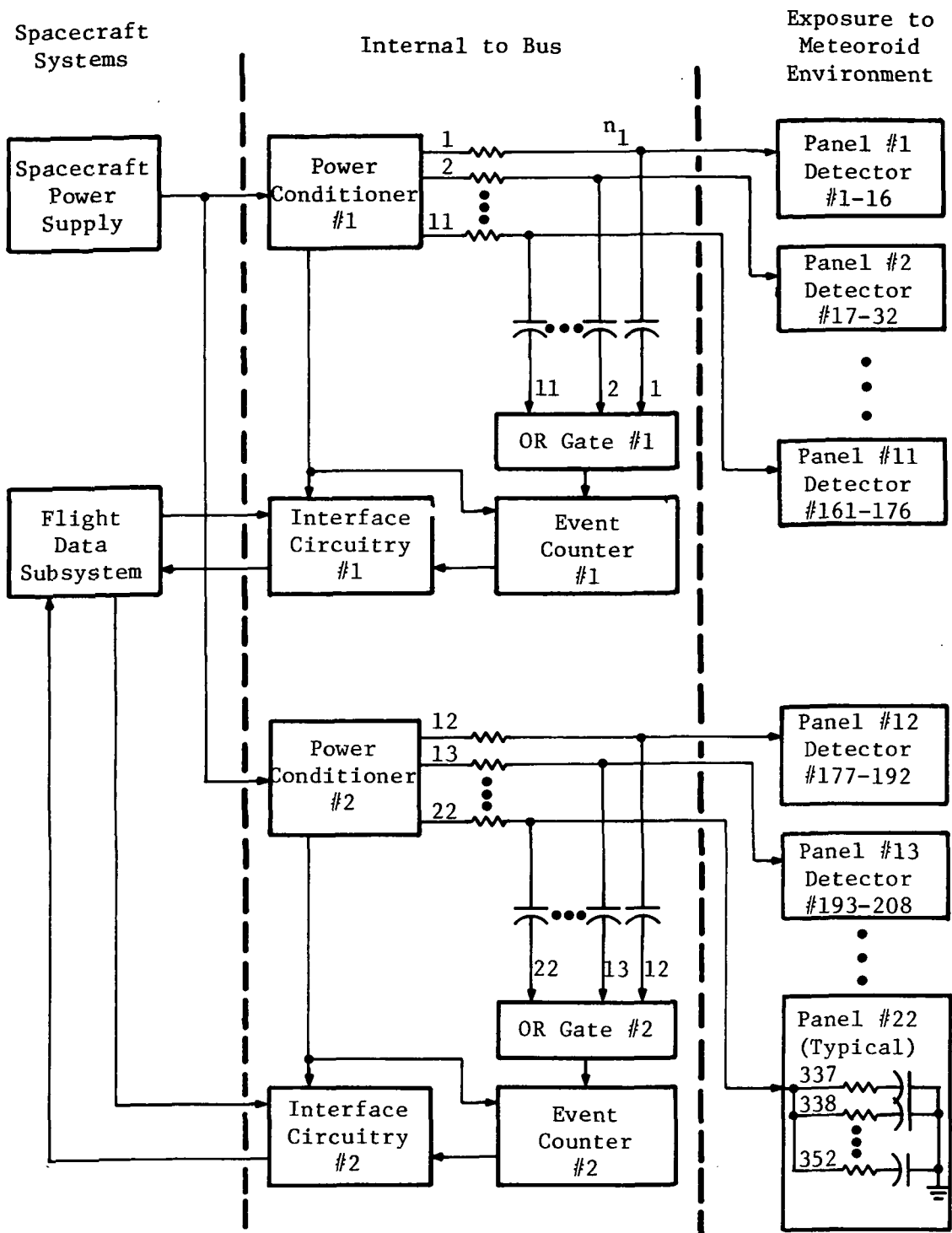


Figure 21. Simplified Block Diagram of the Capacitor-Type Impact Experiment

Conclusions

The results of these investigations indicate that a meteoroid detection experiment suitable for the outer planets missions can be deployed with pressure-cell detectors and with MOS impact detectors. In either case, the electronic requirements are simple, and weight and power requirements are minimal. A 234-cell pressure cell experiment utilizing the Pioneer cells with helium gas and a protective bumper shield, for example, can be deployed which will weigh approximately 2400 g. The electronics would utilize high-reliability fuses to isolate a firing cell and, consequently, have a significantly improved response time--i.e., on the order of fractions of a second.

A capacitor-type impact detector is also a feasible detector for an outer planets MDE. An array of capacitors providing a total detector area of 0.5 m^2 , for example, would require 500 mW and weigh approximately 700 g. Compared to the pressure cell experiment, a capacitor-type MDE would have the significant advantage of an essentially constant detector area throughout the entire mission.

An important area of investigation that should be completed in the future is to characterize both the pressure cell and capacitor detector at temperatures below that of liquid nitrogen. Moreover, the conceptual designs discussed herein must be reviewed in relation to specific mission profiles and specific spacecraft requirements.

SECTION IV

CALIBRATION OF MOS DETECTOR

As discussed previously, a calibration curve for 4000 Å SiO_2 detector has been obtained. Briefly, the calibration is a result of numerous impact observations and an empirical fit for penetration-type curve to divide the regions of discharge and non-discharge for the sensor. Even with this calibration there are at least three unanswered matters of concern:

- 1) Does the calibration depend on the operating voltage of the MOS detector?
- 2) Does the calibration maintain the penetration-type characteristic for a wide range of front electrode and SiO_2 thicknesses and for electrodes other than aluminum and dielectrics other than SiO_2 ?
- 3) Does the calibration based on a penetration-type characteristic have a bound in terms of particle size or mass below which extrapolation is invalid? (Is there a threshold for particle mass or size required to initiate discharge that is not predicted by the penetration-type calibration?)

Answers to these matters are important for two reasons. First, it is very time consuming and expensive to calibrate a given sensor. Variations in the thickness of the dielectric and electrode are inevitable in fabrication. Extremely tight tolerances can be expensive, especially when they are of secondary importance. Therefore, one should establish the effect of variations in thickness on calibration. A second and possibly more important consideration is whether or not selectivity in terms of particle size or mass can be achieved by varying applied voltage, dielectric thickness, and/or electrode thickness. In some instances the selectivity may be desirable; however, a threshold effect can seriously bias or misrepresent a given particle distribution.

Two approaches have been used to gain additional insight regarding calibration. A number of MOS sensors with various thicknesses of dielectric and front electrodes have been fabricated and impacted in the particle accelerator at Goddard Space Flight Center. Major objectives of the series of experiments were to determine

- 1) if the operating voltage influenced the calibration
- 2) if penetration of the dielectric by the impacting particle is necessary and sufficient to initiate an electrical discharge of the MOS detector
- 3) if materials other than SiO_2 for the dielectric and aluminum for the electrode can be used in the fabrication of the MOS detector. The emphasis here was indirectly associated with the fabrication of sensors where SiO_2 and aluminum were considered marginal.

It was expected that the results of these experiments could provide insight into the matter of selectivity. Direct observation concerning selectivity for the 4000 Å SiO_2 used in the most extensive calibration was considered impractical since the smallest particles available in the Goddard facility had been used in the original work. Therefore, the emphasis was toward thicker oxides even though similar calibration of such an extensive nature did not exist.

A second technique became necessary when the relative inefficiency for controlling particle size and velocity in the Goddard facility became apparent. The reasoning was that for oxide thicknesses less than 4000 Å, one may achieve discharge with aerosols or small particles accelerated to sonic velocities. A system was fabricated and demonstrated to be feasible. This approach was used for thin oxides, typically 1000 Å of SiO_2 and 500 Å of aluminum as a front electrode. Major objectives of these experiments were 1) to control the particle velocity and vary the particle size and mass in an attempt to establish deviations from the penetration-type calibration and 2) to investigate the threshold or selectivity of MOS detectors of particle size and mass.

Experimental results and analysis of these two experiments are included in subsequent sections. As a matter of introduction, it should be stated that the fabrication procedures were essentially the same except for geometry and mechanical considerations. Therefore, only a brief description of each is given in the appropriate section. In addition, the electronic readout is essentially the same in principle although the instruments and techniques are different. The point here is that the observed results can be compared without fundamental consideration of the detector geometry or the method of electronic readout.

Hypervelocity Micro-Particle Impact Experiments

Capacitor-type micro-particle detectors were fabricated using standard MOS technology. The silicon wafers were 0.01 Ω -cm n-type with varying thicknesses of SiO_2 thermally grown to provide the dielectric. In some instances SiN_3 was R-F sputtered onto the surface of the silicon wafer. Front electrodes were usually varying thicknesses of aluminum. A few units contained a gold front electrode. Electrical contacts were provided by thermal-compression bonds. The active capacitor area was approximately 15 cm². The MOS sensors prepared for the tests conducted at Goddard Space Flight Center are described in Table I.

The particle accelerator at Goddard Space Flight Center utilizes electrostatic acceleration of micro-particles with a diameter from a fraction of a micron to a few microns. The ordinary velocities achieved by these particles range from 1 to 10 KM/sec. Therefore, they are characterized as hypervelocity micro-particles and provide a suitable simulation of micrometeoroids of interest for the MOS capacitor-type detectors.

Table I
MOS Particle Detection Sensors

<u>Wafer No.</u>	<u>Dielectric</u>	<u>Metallization</u>	<u>Clearing voltage</u>
5	10,000 Å SiO_2	500 Å Al	160 Volts
9	4,000 Å SiO_2	2000 Å Al	100 Volts
11	10,000 Å SiO_2	2000 Å Al	160 Volts
15	4,000 Å SiO_2	1000 Å Al	100 Volts
17	10,000 Å SiO_2	1000 Å Al	160 Volts
19	20,000 Å SiO_2	1000 Å Al	300 Volts
21	40,000 Å SiO_2	1000 Å Al	300 Volts
24	4,000 Å SiN_3	500 Å Al	100 Volts
27	1,000 Å SiN_3	500 Å Al (VDS)	30 Volts
30	2,000 Å SiN_3	500 Å Al (VDS)	40 Volts
35	4,000 Å SiN_3	500 Å Al	75 Volts
37	4,000 Å SiO_2	500 Å Al	160 Volts
38	4,000 Å SiO_2	1000 Å Al	160 Volts
39	4,000 Å SiO_2	570 Å Au	100 Volts
40	10,000 Å SiO_2	500 Å Al	160 Volts
41	10,000 Å SiO_2	1000 Å Al	160 Volts
42	10,000 Å SiO_2	570 Å Au	100 Volts

Although programming capabilities are available (selection of particle size and velocity with desired limits), for the sake of efficiency, the facility was operated in a mode which provided particles selected from a rather broadly defined range of particle size and velocity.

A total of 288 events were recorded during the Goddard tests. Details of these events are included in Appendix A. The salient features of the experimental technique used to obtain this data can be briefly described. The sensors were mounted in an evacuated chamber and positioned so that the accelerated particles could impact normal to the front electrode. A bias voltage was applied to the capacitor. The capacitor discharge was detected on an oscilloscope operated in the single-sweep mode and on a strip chart recorder. The recharge current through a known resistance resulted in the measured discharge voltage. Photographs of the discharge signal displayed on the oscilloscope were taken in a few instances. The photographs were used primarily as a means to obtain an accurate measure of the discharge voltage amplitude. In Appendix A the recorded values of discharge voltages were obtained from these photographs.

The reliability of the particle event was considered in some detail. To provide confidence that a particle had in fact impacted the sensor each time the facility recorded a firing event, an optical detector viewed the particle trajectories required to achieve a sensor impact. Even though the facility recorded the parameters of a particle (size and velocity), a concurrence by the optical detector was necessary to record a significant event. Visual inspection of the light flash accompanying capacitor discharge provided additional confidence in the matter of reliability. For the 10,000 Å SiO_2 detectors biased at 60 volts, 34 out of 35 impacts resulted in a capacitor discharge. Each recorded capacitor discharge was accompanied by a particle identification by the optical detector. Conversely, when an event was recorded by the facility but the capacitor did not discharge, the optical detector did not identify or register a particle with the exception of one event. Therefore, the optical detector was considered a reliable indicator as to whether a facility event should result in a particle impacting the MOS detector. A total of 106 uncertain events were recorded. Numerous reasons can be given for the uncertainty or malfunctions. However, the high degree of correlation between the optical detector and 10,000 Å SiO_2 detector discharge signals provided sufficient confidence that details were not pursued. In fact, a typical procedure was to impact a given sensor until at least 10 particles were identified by the optical detector.

The direct information obtained with each facility event was 1) the event number, 2) capacitor discharge or non-discharge, 3) particle identified or particle uncertain, 4) particle diameter, 5) particle velocity, and 6) detector bias. Indirect information was recorded to calculate particle mass, momentum, energy, and discharge voltage.

Three MOS detectors with 10,000 Å SiO_2 dielectric and with 500, 1000, and 2000 Å aluminum front electrodes received primary attention.

In addition, a sensor with a 570 Å gold front electrode was included in these tests. With either a 60-volt or 25-volt bias applied, the detectors were impacted with the full range of particle parameters provided by the Goddard facility. Each detector received at least ten impacts identified optically.

With 60 volts applied to the 10,000 Å dielectric MOS detectors, 34 out of 35 particle events resulted in a capacitor discharge. The range of particle mass and velocity for the 35 events are shown in Figure 22. The extremes for the particle diameter were 0.63 to 3.2 microns. The discharge voltage amplitude was approximately 75 percent of the applied voltage.

With 25 volts applied to the 10,000 Å dielectric MOS detectors, less than 58 percent of the identified impacts resulted in capacitor discharge. In addition, there was no discernible correlation between the front electrode thickness and the number of capacitor discharges. The particle parameters (mass, velocity) for each unit covered a comparable range of values as shown in Figures 23, 24, and 25. The particle parameters for the 25-volt experiments are bounded by approximately the same extreme values as those for the 60-volt experiments. Therefore, there is definitely a bias dependency which must be considered in calibration of the MOS detectors.

For the impacts which were recorded as not initiating a discharge, there is the possibility that a millivolt-type discharge did occur. For most of the impacts, the vertical sensitivity of the oscilloscope was set at 5 V/cm, and discharge signals on the order of a volt were required to trigger the scope. To check this matter, the vertical sensitivity was increased to 0.05 V/cm for a few impacts. With the 25-volt bias applied to the 10,000 Å dielectric MOS sensors, millivolt-level pulses were observed for approximately 50 percent of the impacts which did not initiate large volt level discharges. This observation suggests that there are at least two types of interactions occurring between the impacting particle and the electrical properties of the sensor. However, there was no obvious correlation between particle parameters and discharge voltage level.

Regarding a penetration-type characteristic for the 10,000 Å SiO_2 MOS detector with a 25-volt bias applied, one could easily suggest a delineation between a region of discharge and non-discharge. However, the observations are so few that conclusions drawn upon the data would be very tenuous. Nevertheless, one matter concerning the data is worth mentioning. The particle parameters (mass, velocity) supplied by the Goddard facility appear to have a most probable distribution which results in events clustered about a mass-velocity relationship. Without sufficient data one probably fits to the characteristics of the facility rather than discharge characteristics of the sensor. To provide confidence in a

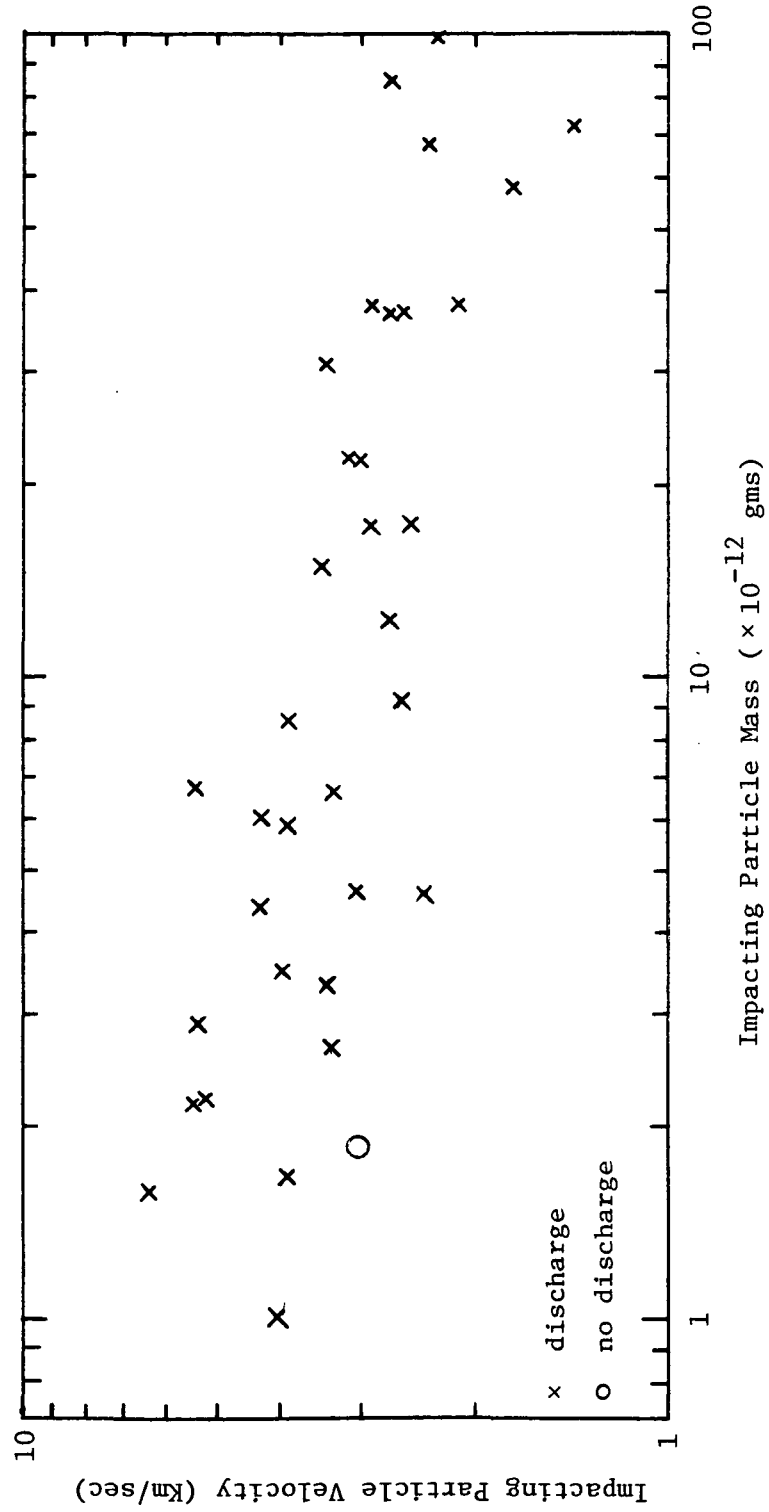


Figure 22. MOS Capacitor Discharge Characteristics When Biased at 60 Volts and Impacted by Hypervelocity Micro-Particles. (Data from MOS Units: 10,000 Å SiO_2 - 500 Å Al, 10,000 SiO_2 - 1000 Å Al, 10,000 SiO_2 - 2000 Å Al, 10,000 SiO_2 - 570 Å Au.)

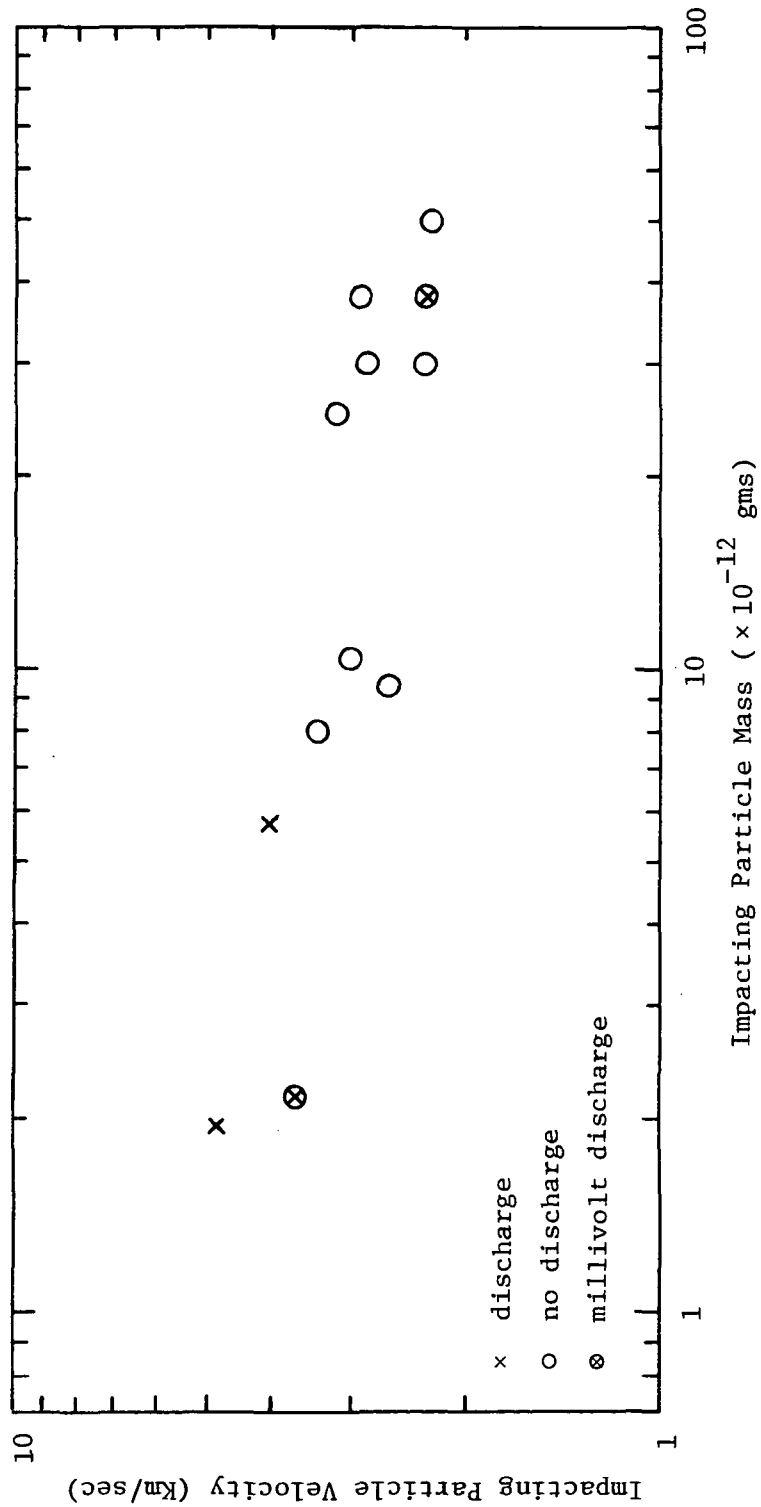


Figure 23. MOS Capacitor Discharge Characteristics When Biased at 25 Volts and Impacted by Hypervelocity Micro-Particles. (Data from MOS Unit: 10,000 A SiO_2 - 2000 A Al.)

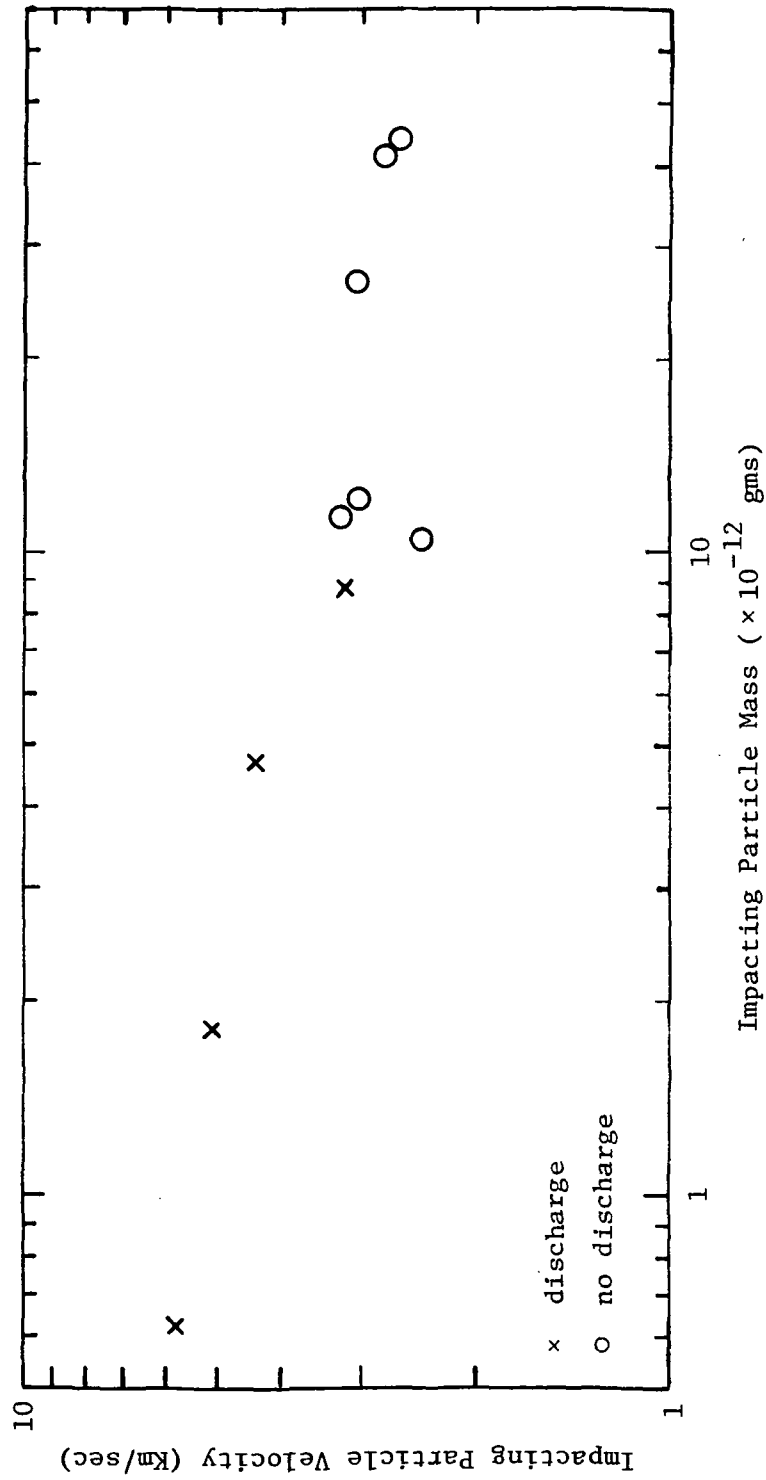


Figure 24. MOS Capacitor Discharge Characteristic When Biased at 25 Volts and Impacted by Hypervelocity Micro-Particles. (Data from MOS Unit: 10,000 A SiO_2 - 1000 A Al.)

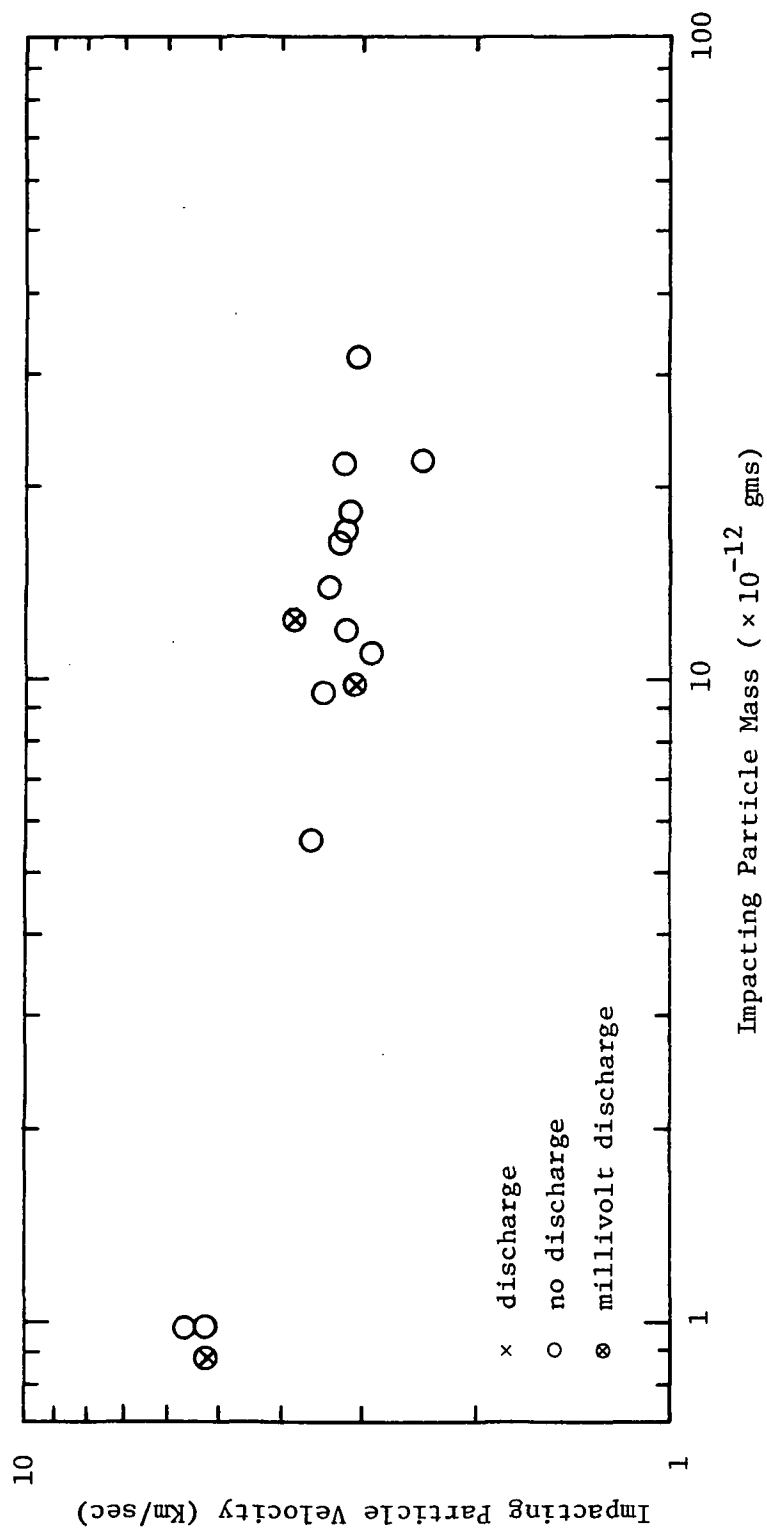


Figure 25. MOS Capacitor Discharge Characteristic When Biased at 25 Volts and Impacted by Hypervelocity Micro-Particles. (Data from MOS Unit: 10,000 Å SiO_2 - 500 Å Al.)

penetration-type characteristic, the extreme capability of the facility should be observed until bias for the most probable particle parameters is removed from the distribution of impact events. Utilizing the program capability to obtain these extreme values requires considerably more time than was available for the experiments reported under this contract.

To investigate whether the bias dependence was unique with the 10,000 Å SiO_2 , a series of tests was conducted for the 4000 Å SiO_2 MOS detector with a 2000 Å aluminum front electrode. With 40 volts applied to the detector, all identified impacts resulted in a capacitor discharge. However, with the bias reduced to 25 volts, capacitor discharge was observed, as shown in Figure 26, for approximately 50 percent of the impacts. Millivolt-level pulses were observed for those instances where the scope sensitivity permitted observations. Again, there was no discernible relationship from the data which suggested a possible mechanism for the bias dependence. In fact, the rather comparable behavior of the 4000 and 10,000 Å SiO_2 units adds further confusion. One might expect the transition from reliable discharge to problematic discharge to be field dependent or related to the energy stored on the capacitor; however, the data do not strongly suggest such a dependence.

MOS units with thicker dielectrics were also impacted. The thickest dielectric was 40,000 Å SiO_2 with 1000 Å aluminum front electrodes. With bias voltages from 150 to 600 volts, no capacitor discharges were observed for the typical particle impacts from the Goddard Facility. The bias of 600 volts for the 40,000 Å SiO_2 yields an electric field in the dielectric equal to the 4000 Å SiO_2 units operated at 60 volts. Therefore, one might conclude that the particles supplied by the facility could not initiate a capacitor discharge. However, the scaling of the bias is a rather uncertain matter based on the bias dependence of discharge for the 4000 Å and 10,000 Å SiO_2 units. For larger applied bias it is possible that the particles could initiate discharge. However, a larger power supply was not available at the time the experiments were conducted.

To gain additional insight into the thick SiO_2 unit performance, a variety of thicknesses from 10,000 Å to 40,000 Å SiO_2 should be impacted in the Goddard facility. Unfortunately, the 20,000 Å SiO_2 units that were impacted behaved erratically, and little information was gained from the tests. However, in principle, thick units should provide the type of data which correspond to a penetration-type initiation of capacitor discharge similar to earlier capacitor-type detectors utilizing thick dielectrics on the order of 60,000 Å.

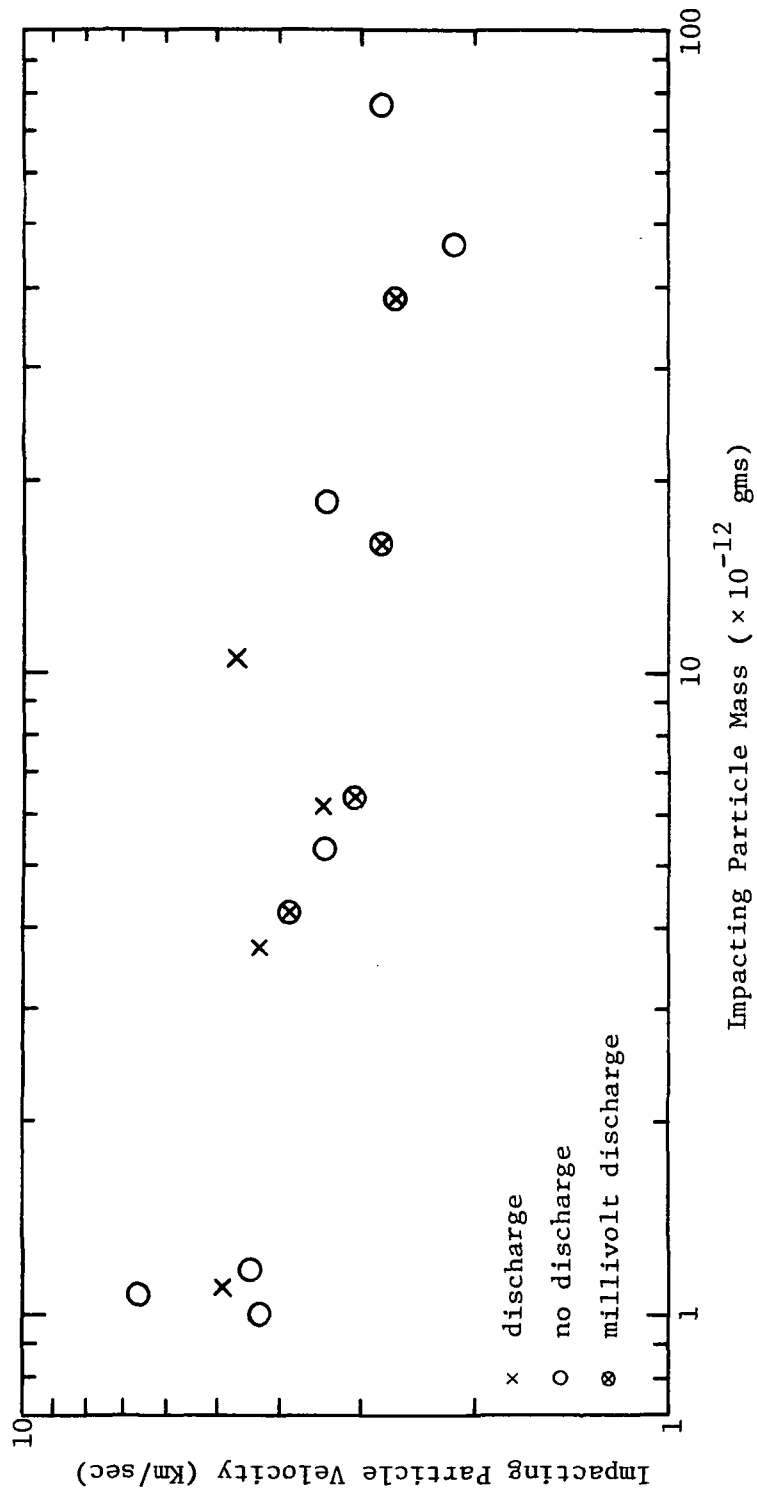


Figure 26. MOS Capacitor Discharge Characteristic When Biased at 25 Volts and Impacted by Hypervelocity Micro-Particles. (Data from MOS Unit: 4000 Å SiO_2 - 2000 Å Al.)

Finally, the matter of utilizing materials other than SiO_2 and aluminum to fabricate the MOS units was considered. A 10,000 Å SiO_2 unit with 570 Å of gold as a front electrode and a 4000 Å SiN_3 with 2000 Å of aluminum as a front electrode were impacted. In general, as shown in Figures 27 and 28, these units responded without major deviations from what was observed for typical units. The major exception was an excessive leakage current for the silicon nitride unit and the rather wide range of discharge voltage amplitudes observed. For an applied voltage of 32 volts, the discharge voltage ranged from 9 to 20 volts. Whether this is typical for SiN_3 units in general would be pure speculation at this point. However, the variation would not negate the use of SiN_3 dielectrics. Reducing the leakage current for the very thin films presents a more significant challenge.

Unfortunately, little information concerning calibration was obtained from the tests at Goddard Space Flight Center. The major deficiencies were the limited range of thick SiO_2 units available, the uncertainty of bias dependence for reliable capacitor discharge, and the narrow cluster of particle parameters obtained in the mode of operation chosen for the tests. Assuming that additional tests can be arranged in the facility, one should attempt to define the bias dependence of discharge for thick SiO_2 units ranging from 10,000 Å to 40,000 Å, possibly in steps of 5000 Å. Some programming or selection of particle parameters should be used to uniformly distribute the impact events with respect to particle velocity and mass. Finally, a clearly defined penetration characteristic for a few thicknesses should provide a relationship which can be used for extrapolation to thicknesses in the range of 4000 to 10,000 Å of SiO_2 .

Sonic Micro-Particle Impact Experiments

To obtain sonic micro-particles, micron-sized particles were injected into an air stream, and the air stream velocity subsequently increased after passing through a constrictive nozzle. The matters receiving primary attention during the development of the micro-particle accelerator were the nozzle, obtaining micron-sized particles, electronic signal processing, and system calibration. Each of these matters is discussed in subsequent sections. In addition, experimental results and a brief analysis of the response of the MOS detector to sonic micro-particles are presented.

Micro-particle accelerators. - Two methods of accelerating particles to sonic velocities have been investigated. Both methods utilize a constrictive nozzle and a pressure drop across the nozzle to achieve an increase in air stream velocity. Micro-particles are injected into the air stream and are accelerated to sonic velocities before impacting the MOS sensor. Velocities on the order of 1000 ft/sec can be achieved with the two systems.

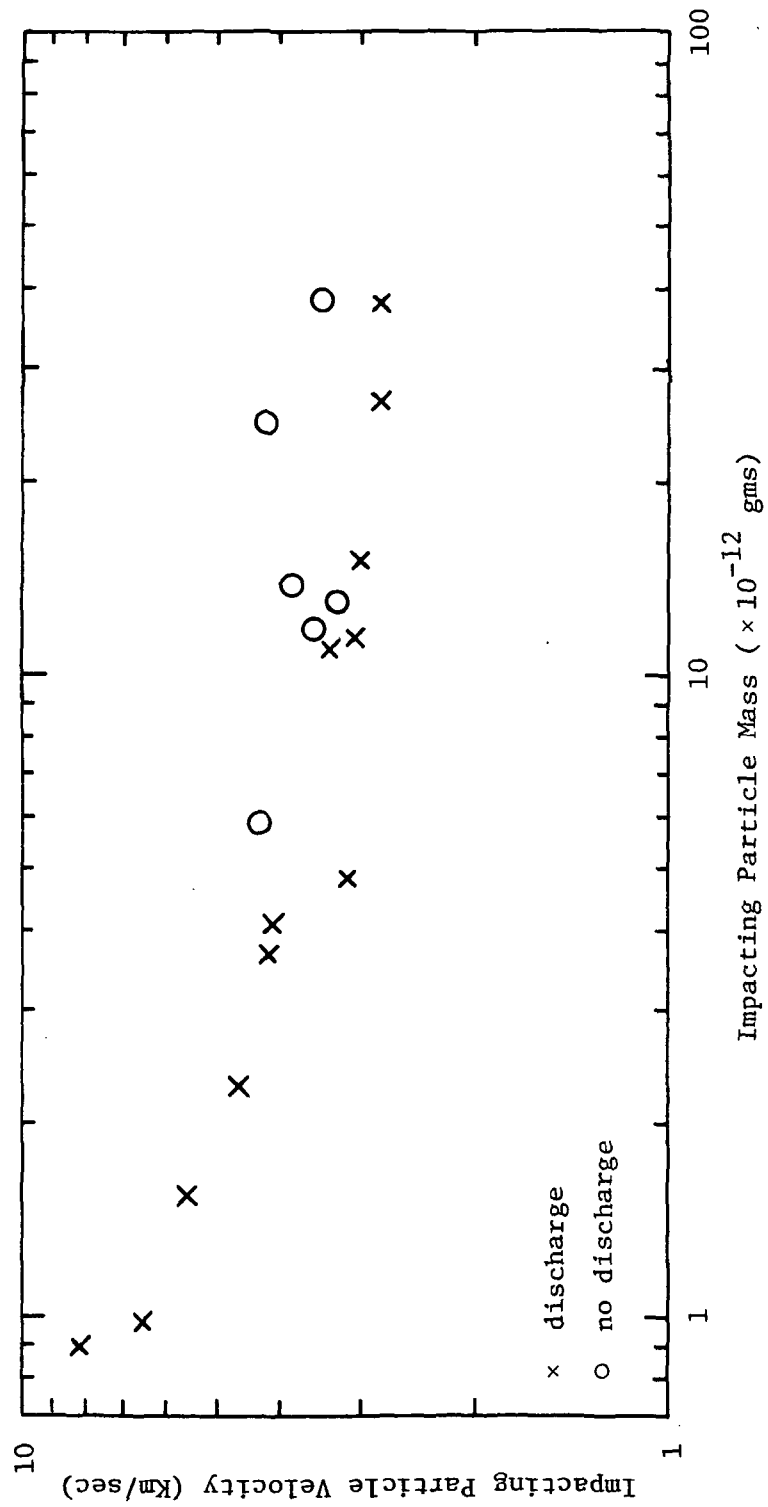


Figure 28. MOS Capacitor Discharge Characteristic When Biased at 32 Volts and Impacted by Hypervelocity Micro-Particles. (Data from MOS Unit: 4000 Å SiN₃ - 500 Å Al.)

Vacuum-operated particle accelerator: The vacuum-operated particle accelerator is illustrated in Figure 29. Using nozzles with output diameters of 0.026, 0.043, and 0.059 inch, air stream velocities of 1227 ft/sec, 1045 ft/sec, and 819 ft/sec, respectively, can be achieved. The vacuum port was connected to a carbon vane pump. The air volume sampled per unit time for a range of pressure drops across the 0.059-inch and the 0.043-inch nozzles are shown in Figure 30. The 0.026-inch diameter nozzle has been omitted primarily because of instabilities noted in the performance of the nozzle as the air stream velocity approaches 1200 ft/sec. Shown in Figure 31 is the air stream velocity versus the pressure drop across the 0.059-inch nozzle. The curve was obtained from well-established theory of nozzle performance using measured values of pressure at the vacuum port of the particle accelerator. For this system the micro-particles would be injected into the air stream before reaching the input to the nozzle. In principle, the input to the nozzle should be in contact with the particle environment to be measured.

Pressure-operated particle accelerator: The pressure-operated particle accelerator is illustrated in Figure 32. The pressure drop across the nozzle is achieved by applying pressures from 10 to 50 psi to the input with the output of the high-velocity nozzle referenced to near 1 atmosphere. Two interchangeable nozzles having output diameters of 0.043 inch and 0.059 inch have been developed and operated. The air volume sampled through the pumping port per unit time for various input air pressures to the high-velocity nozzle is shown for the 0.043-inch and 0.059-inch nozzles in Figure 33. Air stream velocity as a function of input pressure for the 0.059-inch nozzle is shown in Figure 34. The micro-particles are drawn into the air stream by venturi action of the adjustable pumping nozzle inserted around the high-velocity nozzle. This particle injection mechanism results in somewhat different performance of the pressure-operated particle accelerator as compared to the vacuum system. Whereas in the vacuum system the air volume sampled is determined by the velocity of the air stream through the high-velocity nozzle, the air volume sampled by the pressure-operated system depends on the interaction between the high-velocity and the pumping nozzles. The air stream exiting from the high-velocity nozzle into the pumping nozzle experiences a further pressure drop across the pumping nozzle. In turn, the pressure reference for the high-velocity nozzle is not constant at one atmosphere. The air volume sampled by the pumping nozzle depends on the pressure drop across the pumping nozzle. Due to the interaction of the two nozzles, the saturation of air volume sampled occurs well beyond the pressure which results in saturation air stream velocity. Actually the air stream velocity does not completely saturate at the predicted value as well, since the nozzle interactions have been neglected in the calculation of air stream velocity versus pressure to the high-velocity nozzle. Due to the rather complicated performance characteristics of the pressure-operated particle accelerator, relatively few impact tests were performed and little data were recorded. As a consequence, most of the emphasis in this report will be on the vacuum-operated micro-particle accelerator.

Particle suspension and dispersion methods. - Several methods of suspending particles in an air stream were attempted. The types of particles

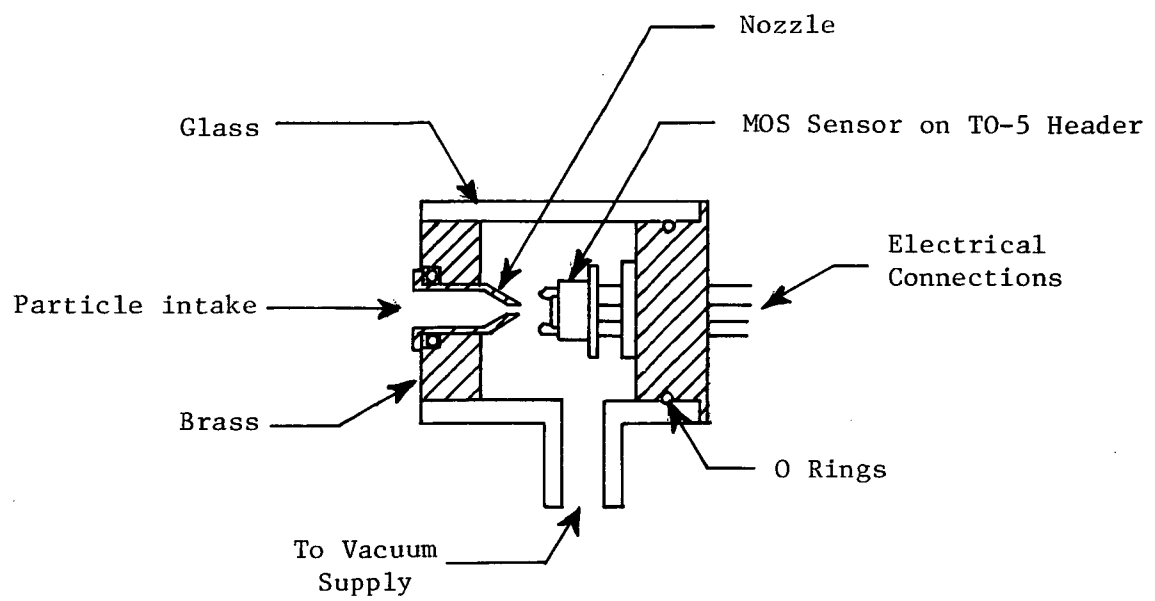


Figure 29. Vacuum Nozzle Particle Accelerator

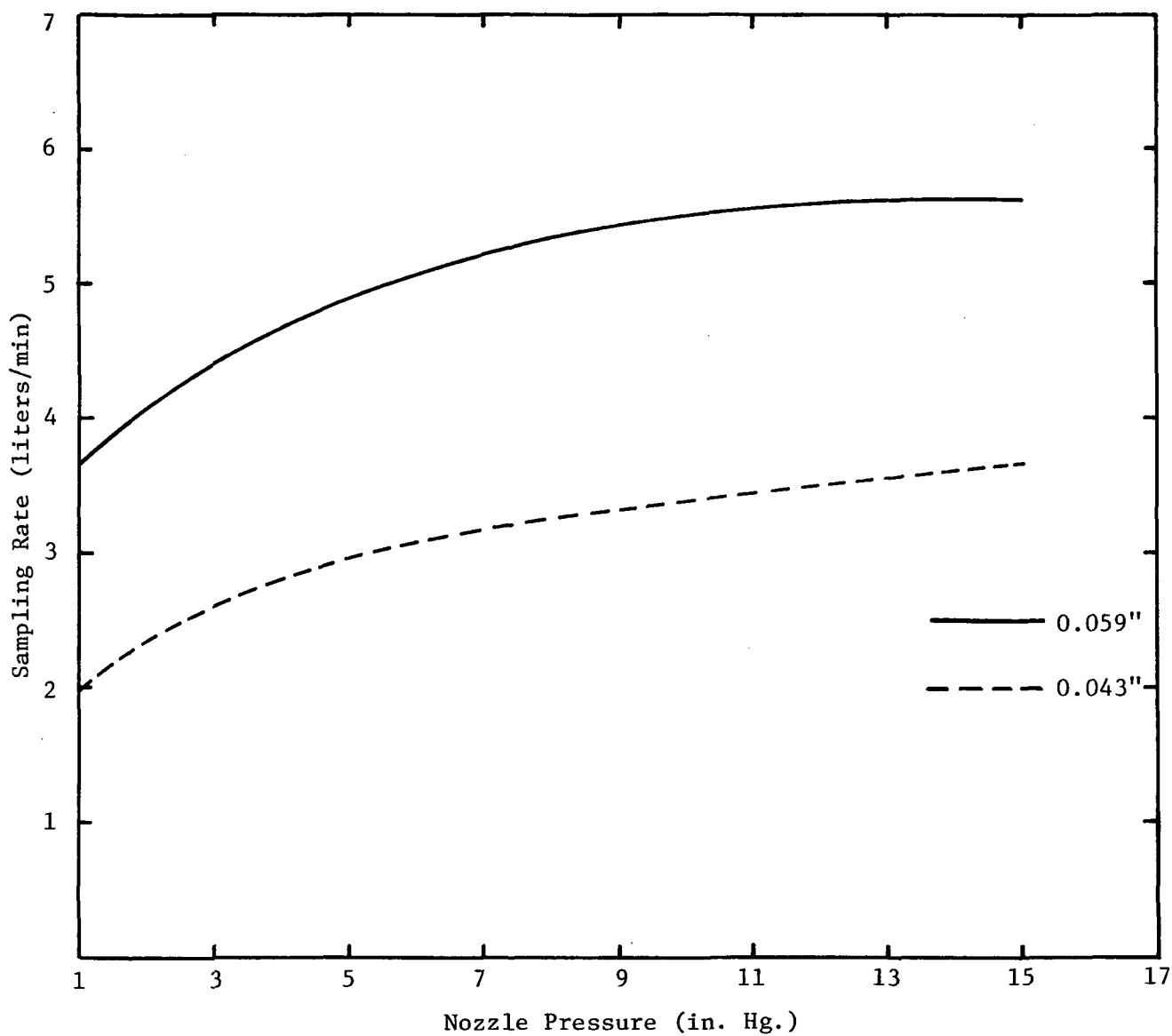


Figure 30. Sampling Rate of the Vacuum Nozzle Particle Accelerator

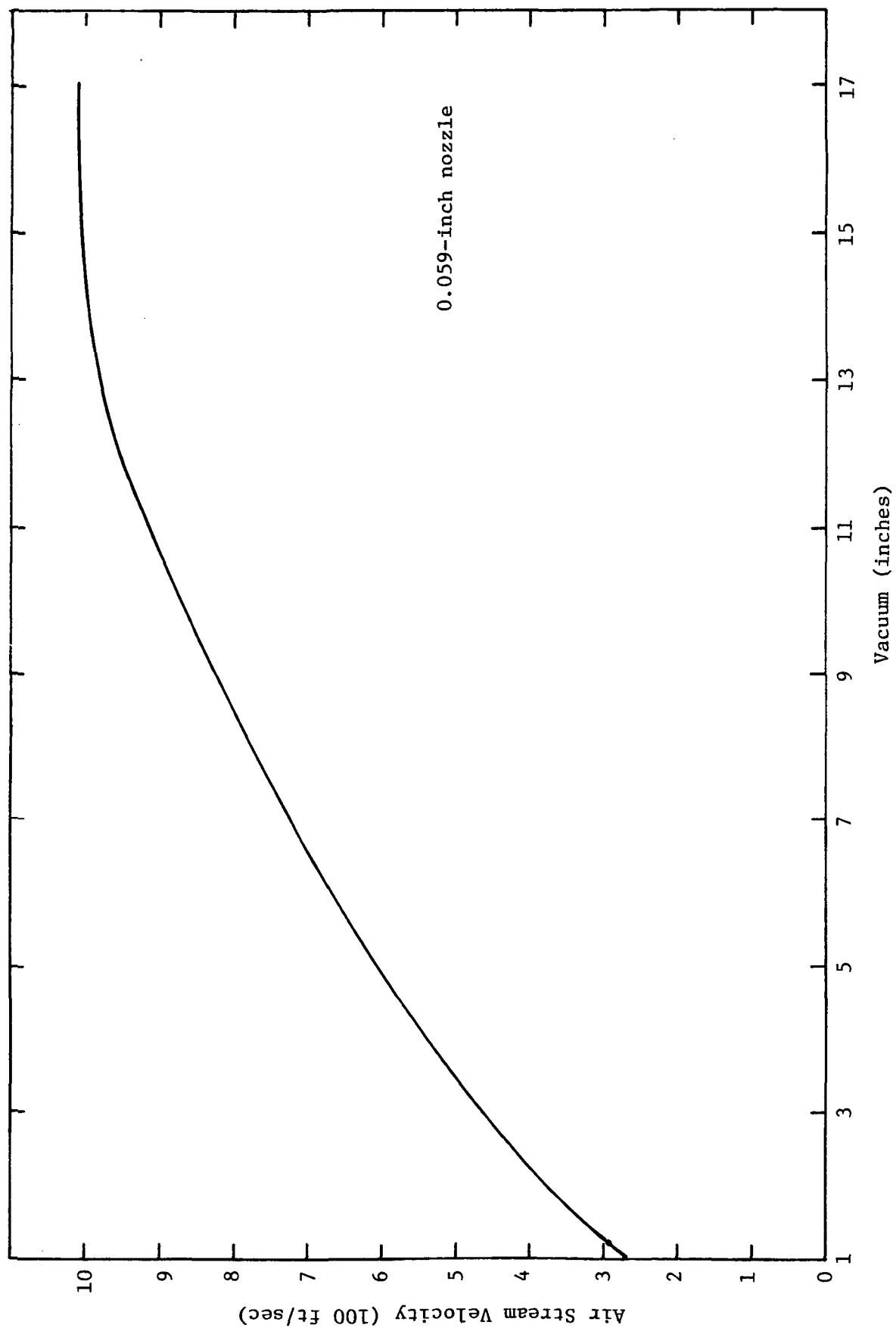


Figure 31. Air Stream Velocity of the Vacuum Nozzle Particle Accelerator

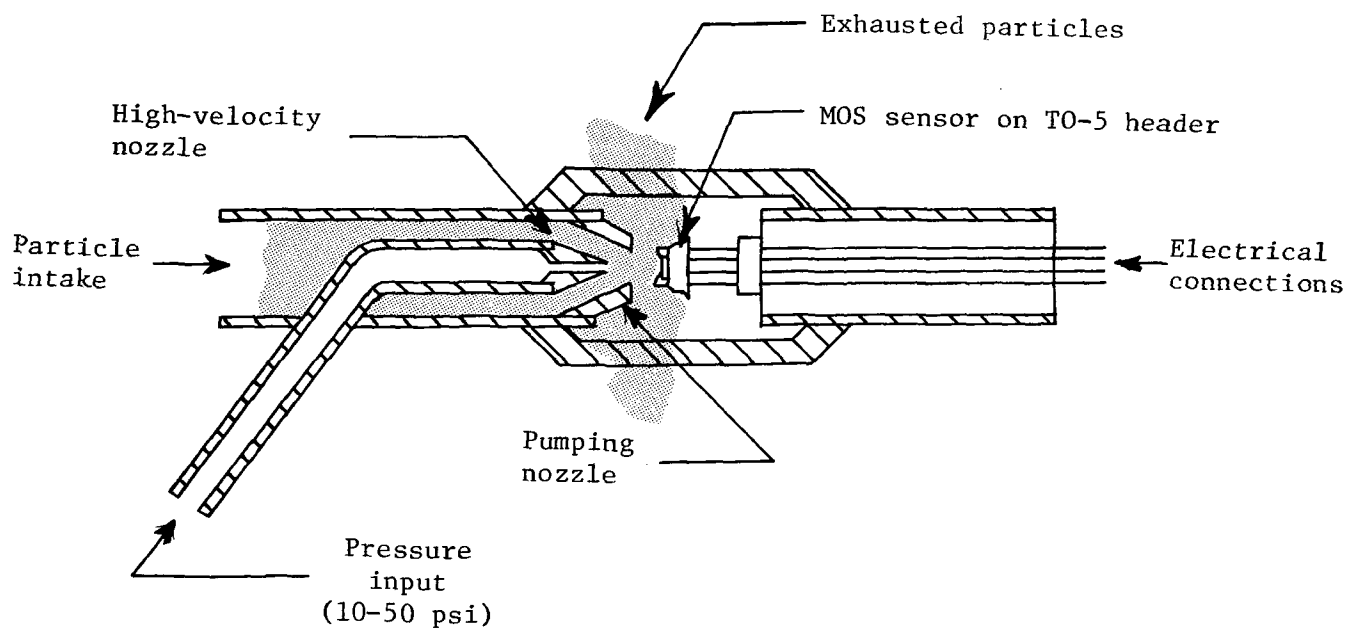


Figure 32. Pressure-Operated Particle Accelerator

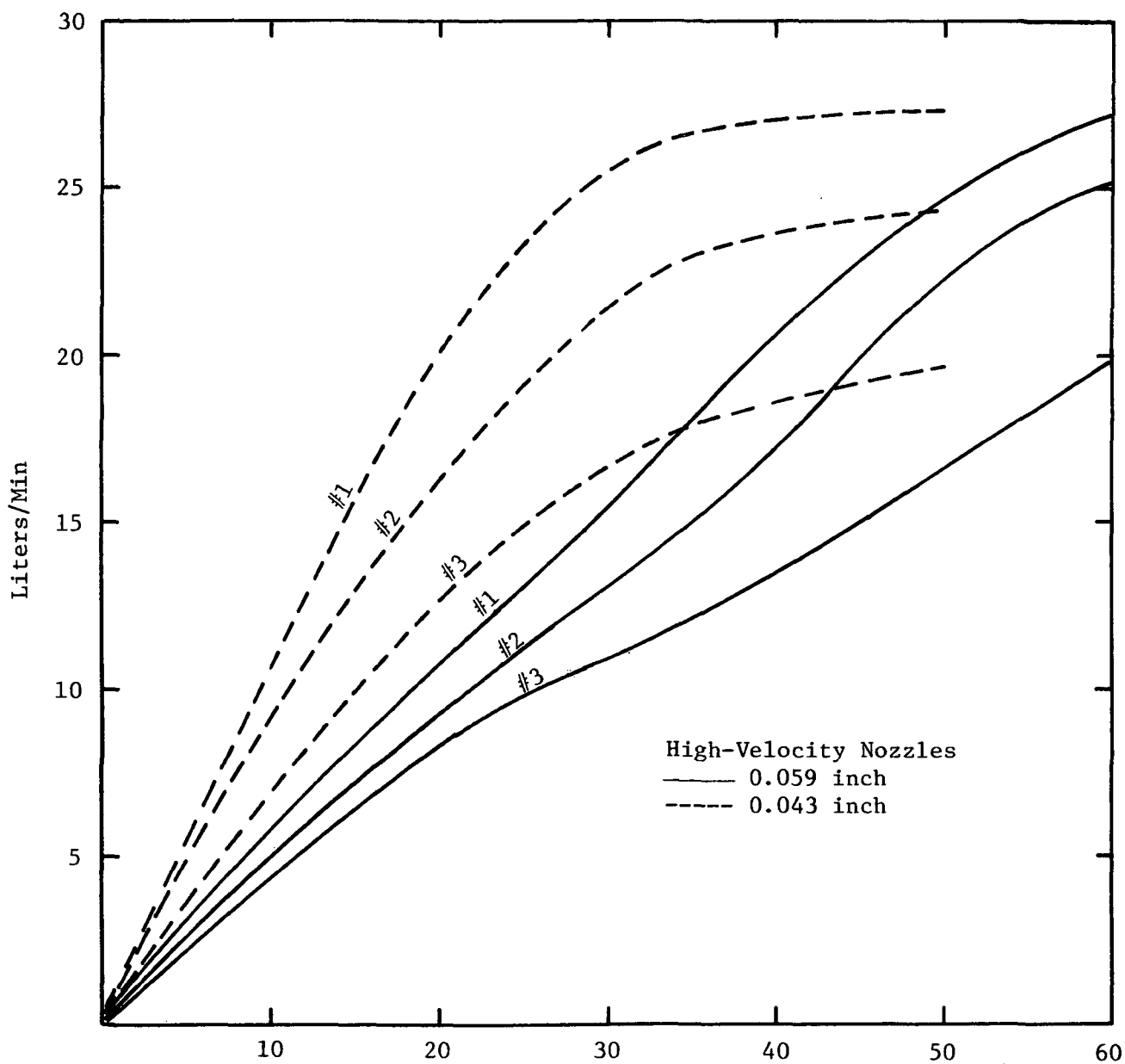


Figure 33. Sampling Rate of the Pressure-Operated Particle Accelerator

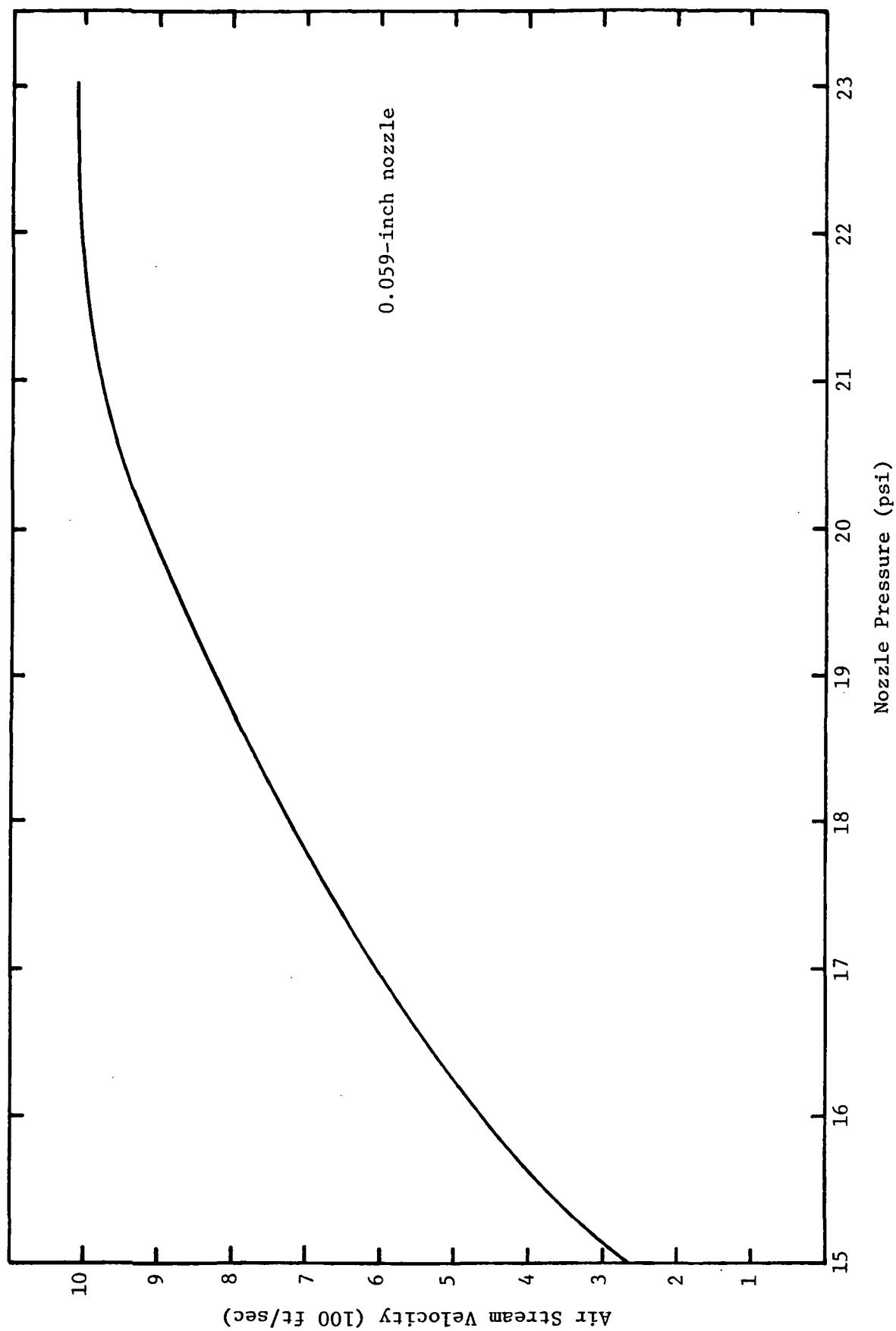


Figure 34. Air Stream Velocity of the Pressure-Operated Particle Accelerator

used for the tests were alumina particles (aluminum oxide), methylene blue particles, dioctylphthalate particles, and NaCl particles.

Alumina particle generation methods: The alumina particles were standard lapping compound. These particles ranged in sizes of 1 μ , 3 μ , 5 μ and 12 μ and had a hardness of 9 on the Mohs scale. Shown in Figure 35 are size distribution curves for these particles. One of the problems with these particles was the fact that they tended to conglomerate. The method used for suspending these particles was to mix the aluminum particles approximately 5:1 with a free flow agent called Aerosil 200 and then suspend the total mixture in isopropyl alcohol. This method worked satisfactorily for test purposes; however, after a few hours the larger particles would settle to the bottom of the solution. For the preliminary test purposes, a spray gun type of apparatus, shown in Figure 36, was used to disperse the particles. The isopropyl alcohol would evaporate after leaving the nozzle, and the particles were then drawn into the particle accelerator units. However, in actual test conditions, an Environmental Research Corporation Model 7300 fluid atomization generator was used. This unit operates on the venturi (spray gun) principle; however, it contained a baffle which imposed an upper limit to the particle diameter which could be generated. It also contained a 1 mili Curie radioactive source which was used to eliminate electrostatic charges on the particles. A schematic of this unit is shown in Figure 37.

Methylene blue generation methods: The methylene blue particles are made as follows: 0.789 gram methylene blue, 0.179 gram uranine, with the total being mixed in 250 ml of ethyl alcohol. The working solution was 25 ml of the concentrated solution, 35 ml ethyl alcohol, and 10 ml distilled H₂O. A Berglund Liu Model 50A monosphere aerosol generator which worked on the vibrating orifice principle was used to disperse these particles. This method of suspension and dispersion produced approximately 5- μ size particles. However, these particles were believed to be spongy on impact and would only produce a counting rate which was equal to about 5 percent of the total particles being dispersed. An Anderson six-stage impactor was used to collect and measure the particle sizes for calibration.

Dioctylphthalate generation method: The dioctylphthalate particles were made as follows. The dioctylphthalate was mixed in a 1:50 ratio by volume with ethyl alcohol. This solution was used without further dilution and was dispersed with the Berglund Liu aerosol generator which produced 10- μ diameter particles. These particles were very soft, and the impact energy was absorbed in the particle and thus produced no counts in the MOS sensors. An Anderson six-stage impactor was used to collect and measure the particle sizes.

NaCl generation method: The NaCl particles were made by mixing a saturated NaCl and isopropyl alcohol solution. This solution was used without further dilution and was dispersed with the Berglund Liu aerosol generator. These particles were approximately 8 μ in diameter and were collected and measured by the Anderson six-stage impactor. These particles would produce counting for a short time on the MOS sensors until the

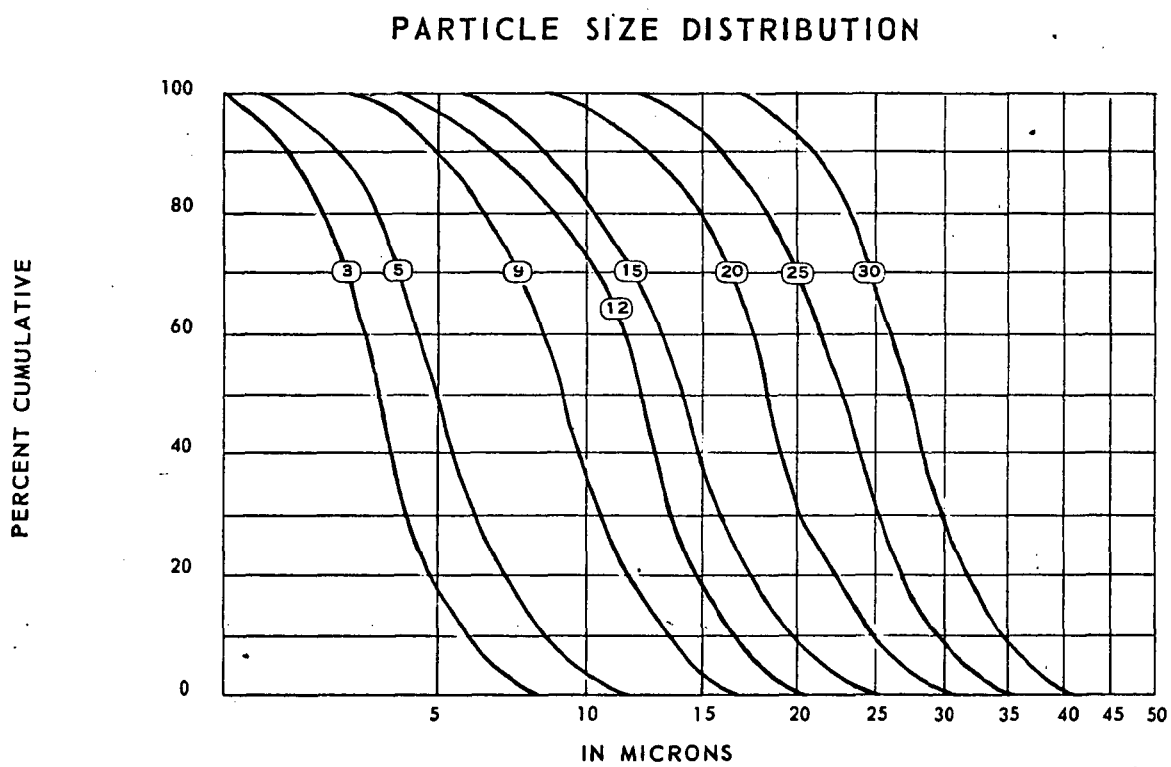


Figure 35. Alumina Particle Size Distribution

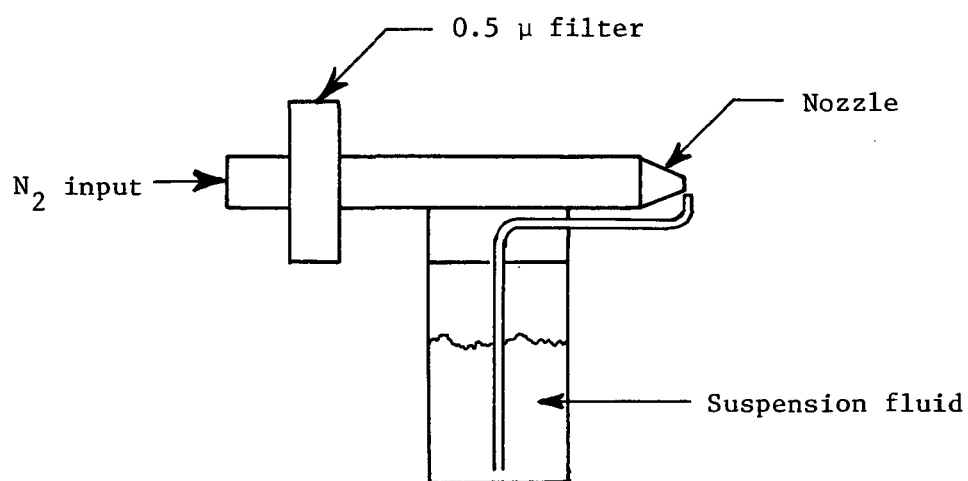


Figure 36. Spray Gun Type Particle Dispersion Unit

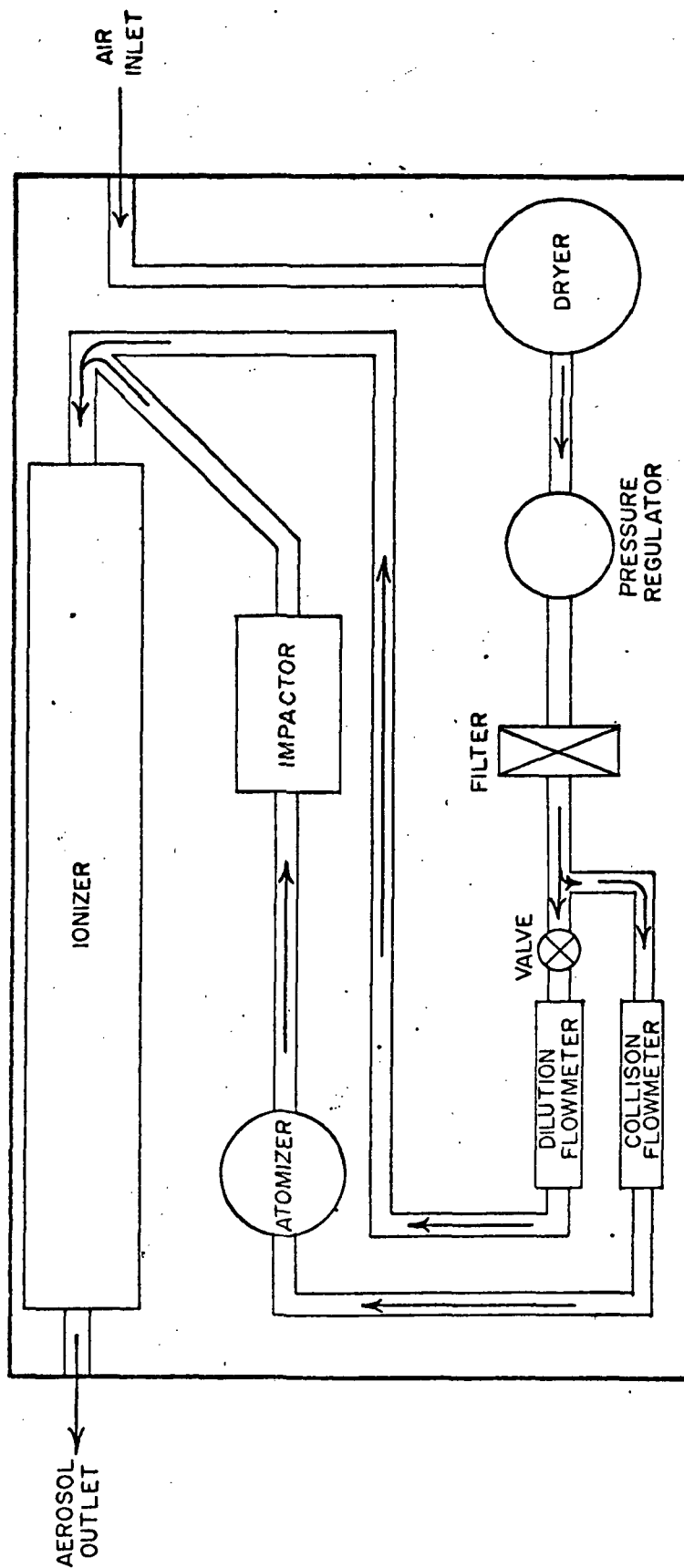


Figure 37. Schematic Diagram of the Fluid Atomization Aerosol Generator

aluminum "capacitor plate" was etched away by the NaCl solution. A method for preventing the corrosion problem must be developed before data can be obtained by the use of these particles.

Electronic readout techniques. - Since the recharge pulse is on the order of hundreds of nano-seconds in width and also varies in amplitude, a circuit was designed which would detect the recharge pulse and give a single pulse with consistent characteristics regardless of the recharge pulse amplitude. The detection circuit was fabricated employing a Fairchild μ A 710 high-speed differential comparator integrated circuit. The output of the detection circuit was connected to the input of a high-frequency electronic counter. This system is illustrated in Figure 38 and has been shown to be very accurate over the desired ranges of pulse widths and amplitudes.

Experimental results and analysis. - MOS sensors with thin SiO_2 layers and thin front electrodes were fabricated and impacted in the sonic-velocity micro-particle accelerators. In general, the sensor responded over a wide range in particle sizes and velocities with varying degrees of success. As a matter of introduction, it should be emphasized that the results to be reported in subsequent sections are tentative and should be reproduced with more experimental control than has been possible to date. The main difficulty has been a reliable particle size distribution which permits meaningful analysis of the experimental results.

The emphasis during the experimental phase of calibration of MOS sensors impacted with sonic velocity micro-particles has been on 1) MOS sensor fabrication, 2) experimental design, 3) interpretation of data, and 4) threshold for MOS discharge. Each of these areas will be discussed in some detail in the subsequent sections.

Fabrication of MOS sensors elements: The MOS sensors are basically capacitors fabricated by evaporating an aluminum "plate" on a dielectric (SiO_2) which is grown on silicon material. Standard I-C processes were used in the fabrication of these units. Following is a description of the fabrication process.

The silicon material was purchased from Monsanto and was p-type 0.01 Ω -cm, 1-1-1 oriented 1 1/4-inch diameter wafers polished on one side. The first step was to prepare the silicon and grow the SiO_2 dielectric. The wafers were cleaned by a standard silicon cleaning cycle which included the use of solvents and acids. The wafers were then loaded into the quartz tube of the oxidation furnace for the oxidation cycle. The furnace was at 1100°C and had 2000 cc/min of dry O_2 flowing through it. The oxidation time was varied to produce SiO_2 layers of 500 Å, 700 Å, 900 Å, 1000 Å, 1100 Å, 1500 Å, and 2000 Å.

The next step was to evaporate a metal contact ("plate") on the SiO_2 layer. The silicon wafers with the SiO_2 films were baked in a vacuum oven

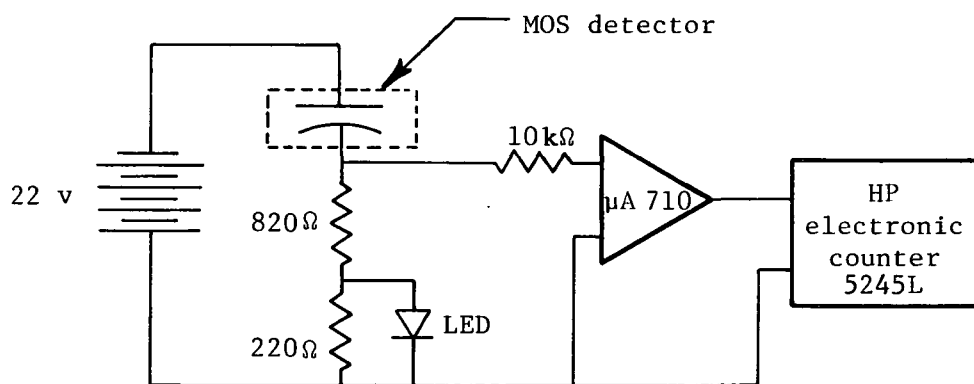


Figure 38. Schematic of the Recharge Pulse Detection Circuit

at 200°C under a vacuum of approximately 25 in. Hg. for 30 minutes in order to drive off any moisture that may have been absorbed by the SiO_2 layers.

The wafers were then placed in the evaporator on evaporation masks containing a 50 x 50 array of 15-mil diameter holes on 20-mil centers. A normal aluminum evaporation cycle to obtain a 500 Å thickness was carried out. The silicon wafers were then removed from the evaporator and waxed to a glass slide with apiezon wax. The side with the aluminum dots was turned down and protected by the wax while the SiO_2 was etched from the back of the wafers with hydrofluoric acid. After the etch step, the apiezon was cleaned from the wafers with several steps of boiling in trichloroethylene. The wafers were then placed back in the evaporator, and 1000 Å of aluminum was evaporated on the back of the wafers for electrical contact to the silicon. The wafers were then removed from the evaporator and were annealed in the vacuum oven at 200°C under 25 in. Hg. for 20 minutes to improve the adherence of the aluminum and thus enhance the wire bonding step.

The next step in the fabrication sequence was to scribe the wafers with a diamond scribing machine to form 100-mil squares containing approximately a 5 x 5 array of the 15-mil diameter MOS capacitor. Figure 39 is a representation of each element of the MOS array.

The 100-mil square silicon chips were mounted to 12 pin TO-5 gold-coated headers by a eutectic scrub technique. This operation was carried out on a TO-5 header holder which was heated to 450°C. The 100-mil square silicon chip was placed on the hot TO-5 headers and was scrubbed on the header surface in a random motion until a eutectic bond was formed between the silicon and the gold of the TO-5 header. This operation not only makes a very strong mechanical bond but also forms a good electrical contact as well.

The last step in the fabrication cycle is the bonding of 1-mil diameter gold leads from the MOS capacitor to the posts of the TO-5 header. This is accomplished by the use of a nail head bonder at a temperature of 320°C. Eleven of the MOS capacitors were connected to eleven posts on the TO-5 header, and the twelfth post was connected to the TO-5 header base which served as a common contact for the eleven capacitors. Figure 40 shows a photomicrograph of a completed MOS particle sensor. One important fact to note from the photograph is the active area of the sensor relative to the total area. The 11 units occupy approximately 20 percent of the area of the silicon chip. This factor should be recognized in the analysis of the counting of micro-particles by MOS units.

Experimental design: To test the performance of the MOS detectors when impacted by sonic-velocity micro-particles, MOS units varying in SiO_2 thickness from 700 Å to 2000 Å were inserted into the vacuum-operated micro-particle accelerator described earlier. The MOS units were impacted by all the micro-particles described earlier; however, the alumina particles have received more attention and will be considered in subsequent sections. The main reasons for the emphasis on alumina are the reliable discharge from

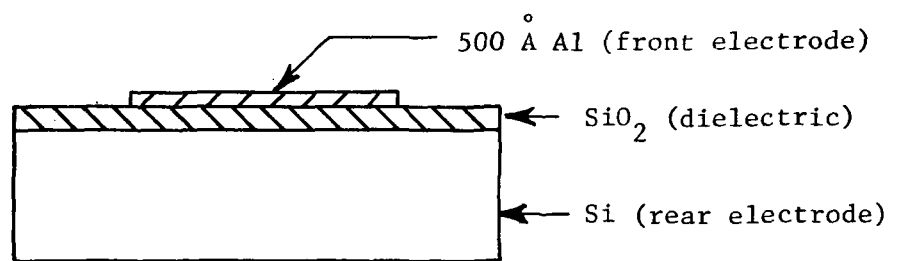


Figure 39. Cross Section of MOS Capacitor

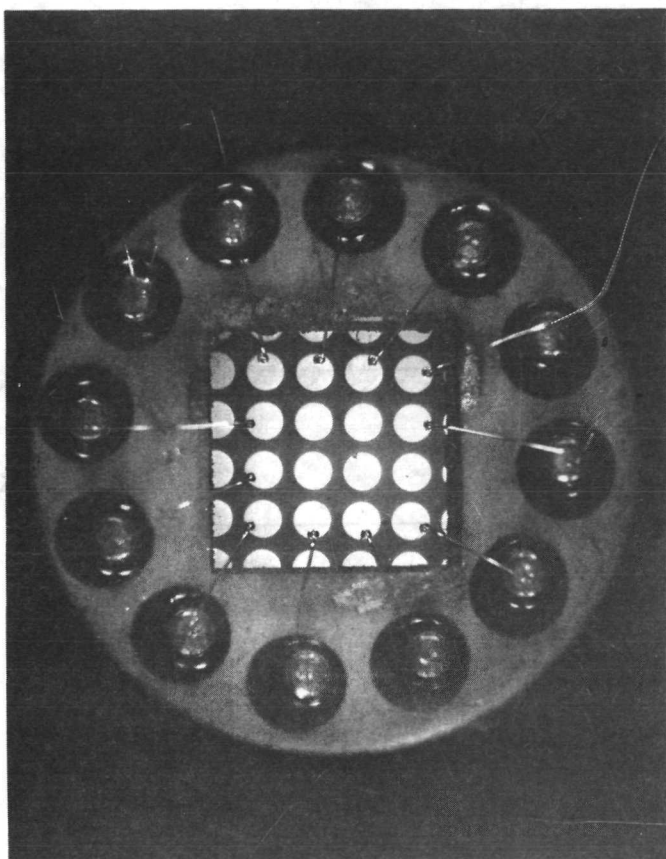


Figure 40. MOS Array Micro-Particle Detector

their impact, the availability of various distributions of alumina particles, and the relatively inert chemical property of alumina powder. The major disadvantage of the alumina particles is the broad distribution in particle size for a powder with a given mean size. This broad distribution complicates matters for two reasons: 1) It is very difficult to maintain the distribution through any reasonable sampling technique. 2) The counting efficiency of the MOS may vary drastically over the range in particle diameters. Consequently, the data recorded for alumina must in some way account for the particle size distribution.

The alumina particles were suspended in a free flow agent and mixed with isopropyl alcohol as described in a previous section. The mixture was dispersed into a manifold from a fluid atomization particle generator. Particles supplied to the manifold were sampled by the vacuum-operated micro-particle accelerator and by a Climet particle counter. This experimental arrangement is illustrated in Figure 41. The Climet particle counter utilizes light scattering from the micro-particles as a means of detecting a particle and its size. The particle size can be detected in eight ranges. However, half of the ranges were below 1 micron and were not recorded. The ranges of interest were 1-2, 2-4, 4-8, and 8- ∞ microns. Although absolute calibration was not attempted, the Climet was used as a reference to characterize the observed response of the MOS units. Therefore, it should be re-emphasized that the particle size distribution is only inferred from the Climet.

Interpretation of Data: During the contract period, over 300 MOS units have been fabricated. Oxide and electrode thicknesses have been varied, and in a few instances the geometry of the array has been altered. However, most of the units were a 5 x 5 array of 15-mil devices with approximately 1000 Å SiO_2 and 500 Å Al. Approximately 200 calibration experiments involving the MOS units have been completed. Many of these experiments dealt with preliminary design of the sonic-velocity micro-particle accelerator and will not be reported. For the experiments devoted primarily to calibration of the MOS detectors, only typical results will be reported.

Some general observations regarding the performance of the MOS units may be of interest. Of the 300 fabricated MOS units, all that were not initially shorted or excessively leaky (leakage current) would count sonic-velocity micro-particles. Typically, the MOS unit would count between 50,000 and 100,000 particles before failure. The modes of failure were either a shorted device or excessive leakage current. In both cases, the failure could occur in one or more of the 11 MOS devices in the array. Where one device caused the failure, disconnecting the faulty device restored counting for the unit; however, with a reduced active area. Although the counting of sonic-velocity micro-particles exhibited substantial variations from experiment to experiment, experimental control of particle size distribution is considered the primary source of the variations.

A typical calibration experiment would utilize the experimental arrangement illustrated in Figure 41. Alumina micro-particles were supplied to the manifold from the fluid atomization generator. The particle

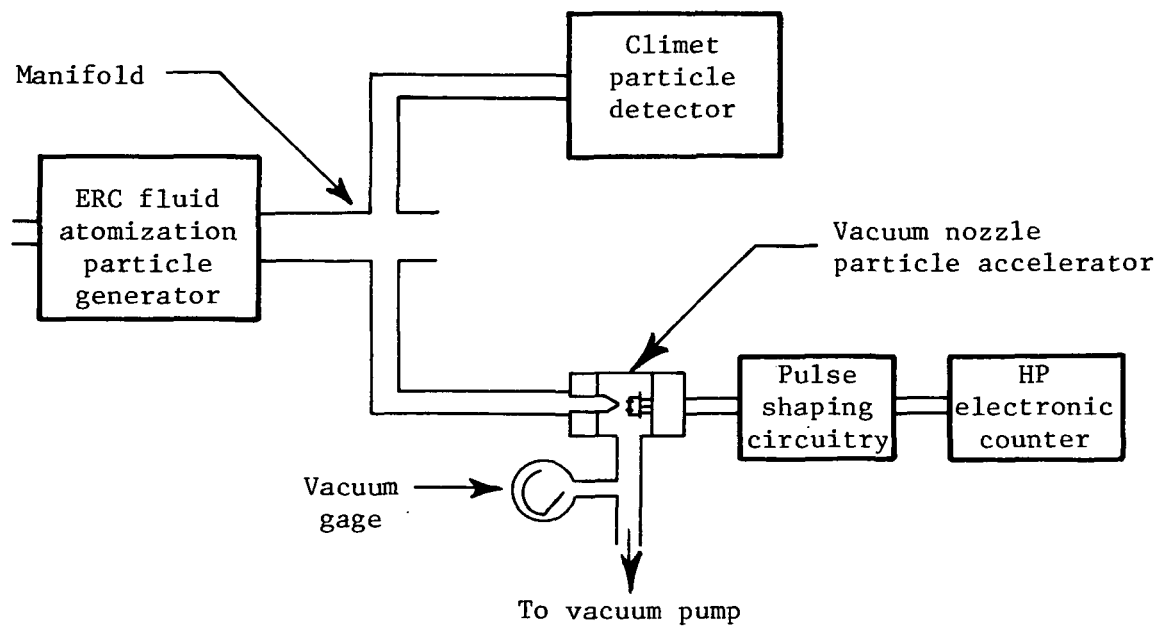


Figure 41. Data Collection System

concentration in the manifold was saturated so that sampling did not depend on ambient air leaking into the sampled volume. One might expect the particle size distribution to be approximated by Figure 35. However, non-uniform mixing of particles in suspension, the restrictive baffle in the generator, frictional forces in the air stream, and gravitational forces for lengthy air stream paths will alter the particle size distribution. Particles sampled from the manifold by the Climet indicate a rather drastic change in particle size distribution as shown in Figure 42. The four original distributions were essentially normally distributed about mean diameters of 1-, 3-, 5-, and 12-micron alumina particles.

Although the Climet total counts are in excess of 100,000 for a 30-second sampling time with a flow rate of 0.1 ft³/min, the MOS count was typically a few hundred counts in 30 seconds with a higher flow rate through the particle accelerator. Typical sets of data are shown in Table II. The factors which may account for this behavior are: 1) The active area of the MOS unit is only a fraction of the area impacted by micro-particles, 2) small micron particles will stream around the sensor due to back pressure, and 3) the MOS unit will respond to a selected range of particle diameters. To compare the data from the MOS unit with the Climet data, the different flow rates were taken into account. Using the nozzle flow rates in Figure 30 for the various nozzle pressures listed in Table II, the MOS counts were multiplied by the ratio of the Climet sampling rate to the MOS sampling rate. The column labeled "Flow rate corrected data" is the result of this multiplicative process.

To obtain a meaningful comparison between the MOS counts and the Climet data, some insight into the three factors (active area, particle streaming, and selective size counting) listed earlier is necessary. From the raw data it appears that at least 99 percent of the particles counted by the Climet are not counted by the MOS unit. A direct approach to account for the limited area and particle streaming has not been currently developed. The major effort to date in the interpretation of the data has been devoted to the matter of selective response for the MOS unit. The approach considered in detail utilizes the fact that the Climet counts in four size intervals. Thus the MOS counts are related to the Climet counts by

$$C = T_1 \alpha_1 N_1 + T_2 \alpha_2 N_2 + T_3 \alpha_3 N_3 + T_4 \alpha_4 N_4 = \sum_{j=1}^4 T_j \alpha_j N_j$$

where N_j is the Climet counts in the j^{th} particle size interval, T_j is the counting efficiency for particles in the j^{th} size interval, and α_j accounts for differences in sampling rates to the two units. The α_j could also account for changes in distributions resulting from heavy particle settling due to air stream friction or gravitational forces. However, the only correction employed is for the different sampling rates as discussed earlier. In this case,

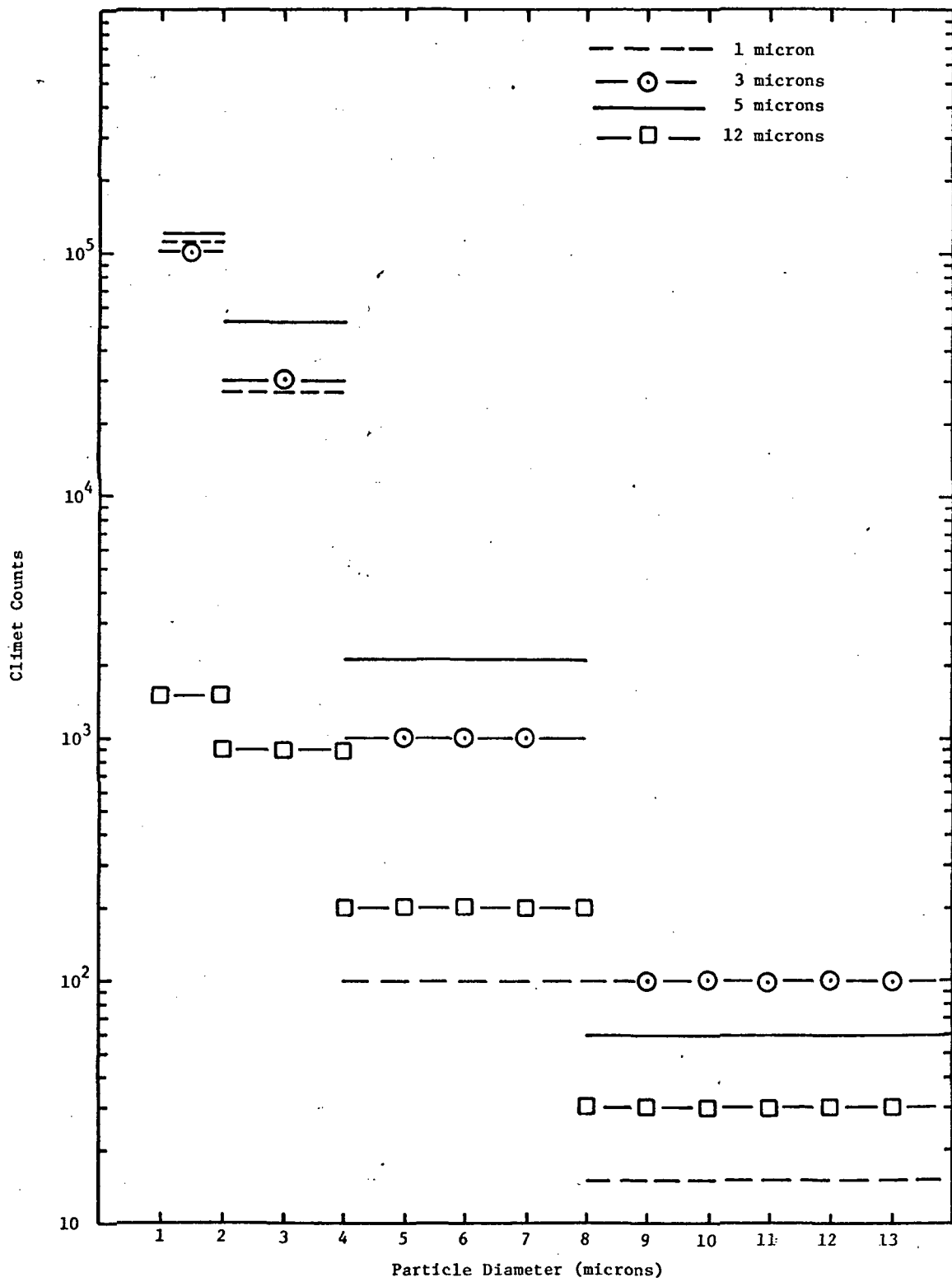


Figure 42. Histogram of Particle Distribution

Table II

Calibration Data for MOS Units Impacted by Sonic-Velocity Micro-Particles
 [15-mil dots, 1000 Å SiO₂, 0.059-inch nozzle, 500 Å Al, 20-volt bias]

Mean diameter of alumina in suspension	Nozzle pressure	Climet readings					MOS counts	
		1-2 μ	2-4 μ	4-8 μ	8-∞ μ	>4μ	Raw	Flow rate corrected
1 μ	1.0 in.Hg							
	3.0 in.Hg							
	5.0 in.Hg	112,263	28,601	88	15	105	11	2
		111,799	28,066	105	28	133	8	2
	8.0 in.Hg	106,834	26,226	100	36	136	15	3
		105,980	25,601	93	20	113	14	3
3 μ	10.5 in.Hg	102,903	24,646	86	15	101	36	7
		103,451	24,499	121	15	136	45	8
	15.0 in.Hg							
	1.0 in.Hg	106,021	34,103	1,021	155	1,176	95	32
		101,903	31,948	850	145	995	80	27
	3.0 in.Hg	101,317	31,329	920	129	1,049	220	61
3 μ		102,124	31,915	868	114	982	209	58
	5.0 in.Hg	102,092	31,218	856	90	946	523	131
		102,462	31,963	930	108	1,038	486	120
	8.0 in.Hg	102,795	31,409	857	104	961	1,023	234
		99,413	29,926	839	90	929	989	226
	10.5 in.Hg	98,073	29,458	821	115	936	1,538	339
3 μ		101,794	30,243	795	107	902	1,406	310
	15.0 in.Hg							

Table II (continued)

Mean diameter of alumina in suspension	Nozzle pressure	Climet readings					MOS counts	
		1-2 μ	2-4 μ	4-8 μ	8- ∞ μ	>4 μ	Raw	Flow rate corrected
5 μ	1.0 in.Hg	114,531	52,189	2,159	64	2,223	555	151
		116,705	53,295	2,134	64	2,198	464	126
	3.0 in.Hg	118,163	53,811	2,288	59	2,347	1,074	245
		120,112	54,849	2,202	60	2,262	1,048	239
	5.0 in.Hg	121,038	54,947	2,189	47	2,176	2,453	502
		120,975	55,671	2,416	52	2,468	2,443	500
	8.0 in.Hg	118,150	53,395	2,229	48	2,277	4,696	879
		118,683	52,478	2,115	51	2,166	4,395	823
	10.5 in.Hg	118,577	52,178	2,014	51	2,065	6,067	1,097
	15.0 in.Hg	119,868	52,699	1,990	46	2,036	5,518	998
12 μ	1.0 in.Hg	1,669	865	267	31	298	21	5.7
		1,738	929	233	31	264	27	7.4
	3.0 in.Hg	1,725	861	244	28	272	47	11
		1,760	880	236	23	259	47	11
	5.0 in.Hg	1,765	903	217	17	234	91	19
		1,805	886	232	29	261	98	20
	8.0 in.Hg	1,811	839	232	29	261	153	29
		1,829	903	194	23	217	133	25
	10.5 in.Hg	1,833	898	204	10	214	217	39
	15.0 in.Hg	1,921	879	215	21	236	191	35
		1,938	895	199	22	221	260	
		1,969	868	223	17	240	263	

Table II (continued)
^o [15-mil dots, 700 Å SiO₂, 0.059-inch nozzle, 500 Å Al, 20-volt bias]

Mean diameter of alumina in suspension	Nozzle pressure	Climet readings					MOS counts	
		1-2 μ	2-4 μ	4-8 μ	8-∞ μ	>4μ	Raw	Flow rate corrected
1 μ	1.0 in.Hg							
	3.0 in.Hg							
	5.0 in.Hg	105,354	28,923	117	9	126	16	3
		106,575	28,842	97	16	113	13	3
	8.0 in.Hg	103,274	27,514	118	22	140	33	6
		102,264	27,458	110	13	123	32	6
3 μ	10.5 in.Hg	99,668	25,884	115	15	130	46	8
		101,219	26,593	106	16	122	68	12
	1.0 in.Hg							
	3.0 in.Hg							
	5.0 in.Hg	82,170	32,746	1,462	177	1,639	964	263
		84,383	33,380	1,476	142	1,618	938	256
3 μ	8.0 in.Hg	82,195	32,311	1,419	127	1,546	1,923	439
		84,739	33,664	1,536	124	1,660	1,748	400
	5.0 in.Hg	84,860	33,669	1,459	151	1,610	3,389	695
		85,223	33,960	1,528	140	1,668	3,022	619
	8.0 in.Hg	84,986	33,042	1,398	104	1,502	4,906	919
		86,117	33,386	1,446	122	1,568	4,492	841
	10.5 in.Hg	86,816	33,537	1,330	111	1,441	6,176	1,117
		87,250	33,724	1,512	143	1,655	5,288	956
	15.0 in.Hg							

Table II (continued)

Mean diameter of alumina in suspension	Nozzle pressure	Climet readings					MOS counts	
		1-2 μ	2-4 μ	4-8 μ	8- ∞ μ	>4 μ	Raw	Flow rate corrected
5 μ	1.0 in.Hg	90,991	40,005	1,346	46	1,392	650	177
		92,219	39,835	1,372	52	1,424	578	157
	3.0 in.Hg	92,778	39,666	1,309	48	1,357	1,043	238
		93,375	40,399	1,411	61	1,472	1,040	237
	5.0 in.Hg	91,019	37,830	1,224	52	1,276	2,137	438
		93,395	38,310	1,220	58	1,278	1,944	398
	8.0 in.Hg	90,164	36,169	1,189	60	1,249	3,633	680
		90,271	36,606	1,225	65	1,290	3,172	594
	10.5 in.Hg	90,790	36,966	1,186	58	1,244	4,176	755
	15.0 in.Hg	91,458	36,644	1,126	70	1,196	4,040	731
12 μ	1.0 in.Hg	1,300	854	224	13	237	61	17
		1,331	649	158	12	170	51	14
	3.0 in.Hg	1,412	673	169	16	185	87	20
		1,536	703	151	9	160	104	24
	5.0 in.Hg	1,484	774	187	12	199	198	41
		1,588	822	191	12	203	185	38
	8.0 in.Hg	1,509	776	200	17	217	328	61
		1,578	784	180	7	187	366	69
	10.5 in.Hg	1,613	792	194	19	213	501	91
	15.0 in.Hg	1,618	788	186	13	199	452	82

$$\frac{C}{\alpha} = \sum_{j=1}^4 T_j N_j.$$

Since α depends on the sampling rate, the relationship holds for each nozzle pressure. Since there are four particle distributions, the T 's can, in principle, be determined from a 4×4 linear algebraic equation of the form

$$\frac{C}{\alpha} = \sum_{j=1}^4 T_j N_{ij}.$$

Using the 5 inches of Hg nozzle pressure data yields

$$C = -0.0043 N_1 + 0.017 N_2 + 0.043 N_3 + 0.093 N_4.$$

Obviously, the negative sign for the T_1 casts doubt upon the method. Similar results were obtained for the 8 and 10 inches of Hg nozzle pressure data. Therefore, one must conclude that this simple model does not properly account for either counting efficiency dependence upon particle size or variations in sampled distribution between the MOS unit and the Climet. From the above approach, it is not possible to determine where the difficulty occurs.

Another approach to the interpretation of the data is to plot separately the MOS counts versus Climet counts in each of the particle size intervals for the different nozzle pressures and for the four different particle distributions. Considering only one nozzle pressure, one obtains a plot of the variation in MOS count with the variation in Climet count in a particle size interval as the number of counts in that interval varies from the four particle size distributions. If all the MOS counts were due to particles in a given interval, then the MOS counts and the Climet counts should be identical. If the MOS did not count any particles from the interval considered, then the MOS counts should be independent of the Climet counts.

This approach is illustrated in Figures 43 and 44 for the 1000 \AA SiO_2 impacted by the 0.059-inch vacuum-operated nozzle. Obviously in Figure 43 the Climet count and the MOS count agree reasonably well. Note that the vertical and horizontal scales are identical. Recall that a correction for sampling rate has been included; however, no correction for active area or

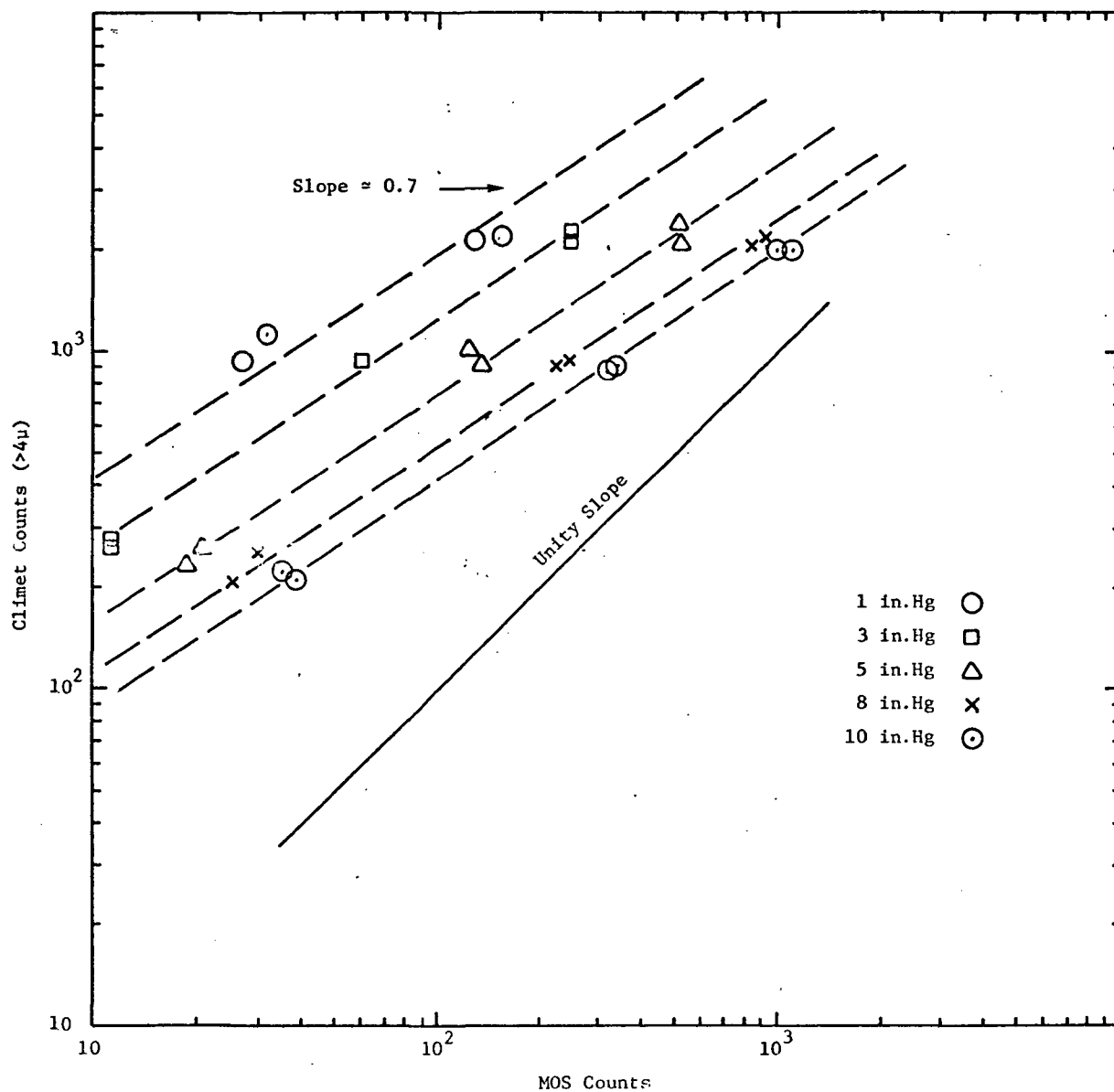


Figure 43. Correlation Between Climet and MOS (1000 \AA SiO_2)

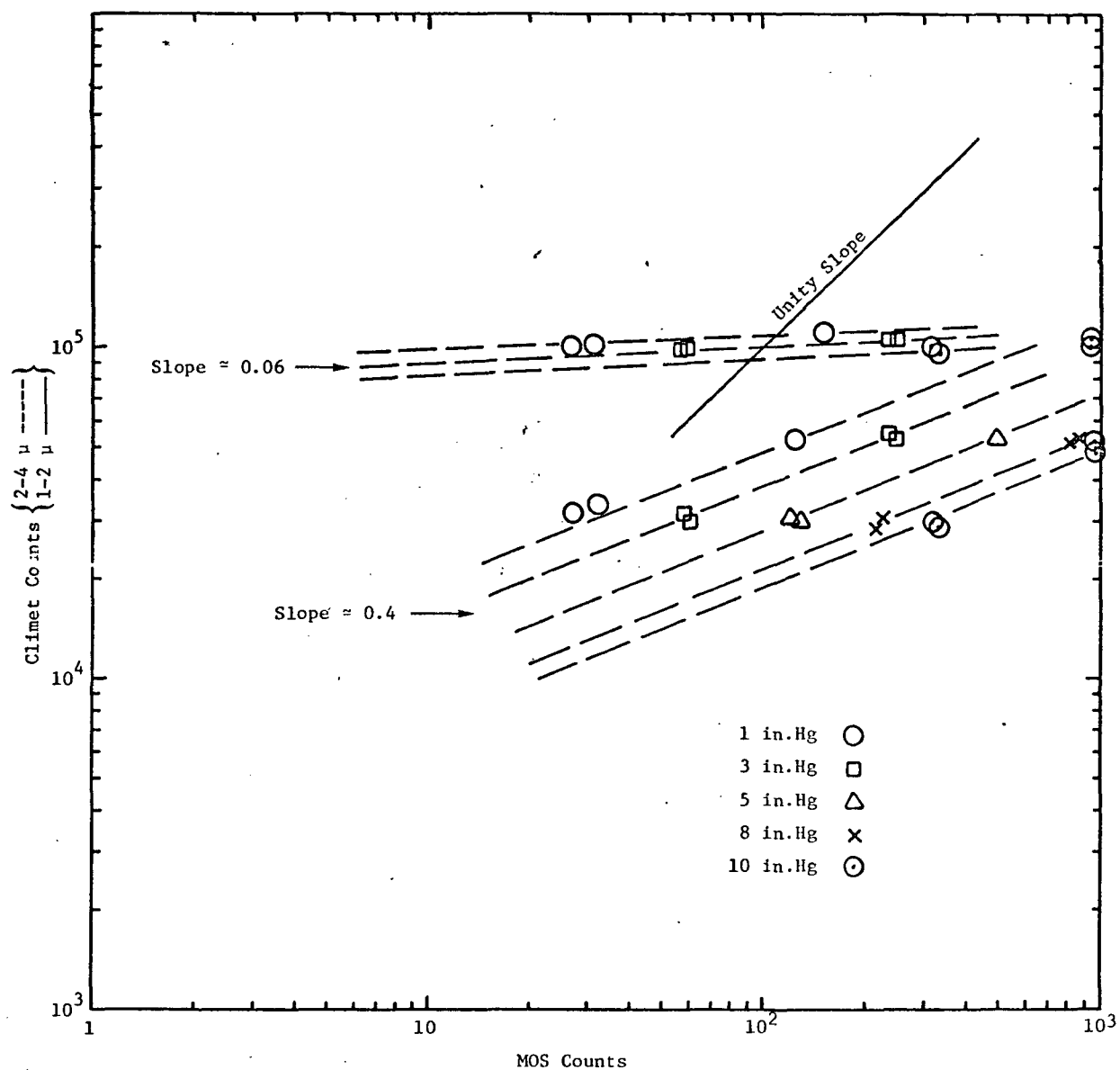


Figure 44. Correlation Between Climet and MOS (1000 \AA SiO_2)

particle streaming has been included. The data for 4-8 and 8- ∞ microns have been added to obtain the Climet count. The reason for adding the 4-8 and 8- ∞ micron data is that the slope in Figure 43 increases from about 0.6 to 0.7, which indicates a higher degree of correlation. For the other Climet intervals, the correlation is not nearly so obvious. Note in Figure 44 that the vertical and horizontal scales differ by 10^3 and that the slope of the curves is 0.4 and 0.06 for the 2-4 and 1-2 micron intervals, respectively.

Considering the above discussion and the apparent correlation of the MOS counting and the Climet counting of greater than 4 micron diameter particles, a tenuous model of performance can be offered. Apparently, the MOS unit responds selectively to the larger diameter particles. The selectivity could result from either small particles (less than 4 microns in diameter) streaming around the MOS unit or the small particles cannot initiate a discharge upon impacting the MOS unit. The fact that the MOS counts increase with pressure tends to support the latter explanation, since particle streaming should increase with air stream velocity assuming no air turbulence effects resulting in localized concentration variations.

The data for an MOS unit with 700 Å SiO_2 dielectric have been interpreted in a manner similar to Figure 43. The results are shown in Figure 45. Again the agreement between the MOS counts and the Climet counts of particles with greater than a 4-micron diameter suggests selective counting. It should also be noted that the 700 Å SiO_2 unit counted a larger fraction of the Climet counts than the 1000 Å SiO_2 unit. If one assumes the 700 Å SiO_2 unit has essentially a 100 percent counting efficiency for particles with greater than a 4-micron diameter accelerated to the air stream velocity, an area factor of approximately 3 would be necessary to bring the Climet data and the MOS data into agreement. The implications of this result have not been fully considered; however, one should recall that the active MOS devices occupy about 20 percent of the silicon area which is about four times the nozzle output area. Depending on how rapidly the air stream diverges near the MOS unit, a wide variation in active area effect is possible.

Threshold for MOS discharge: The observation that the MOS counts per cubic foot of particle environment sampled increases with an increase in pressure drop across the sonic nozzle, as illustrated in Figure 46, suggests that a threshold in alumina micro-particle velocity required to discharge the capacitor may exist. For the 700 Å and 1000 Å SiO_2 units, no such threshold has been observed. However, for the 2000 Å SiO_2 unit an 8-inch-of Hg vacuum applied to the sonic nozzle (air stream velocity of 780 ft/sec) was required for the micro-particles to discharge the MOS capacitors. This requirement was observed for the 1 μ , 3 μ , 5 μ , and 12 μ alumina powders. This indicates that the threshold is not size distribution dependent. However, the increase in the counts does suggest that the number of particles above the threshold for discharge increases with increasing velocity.

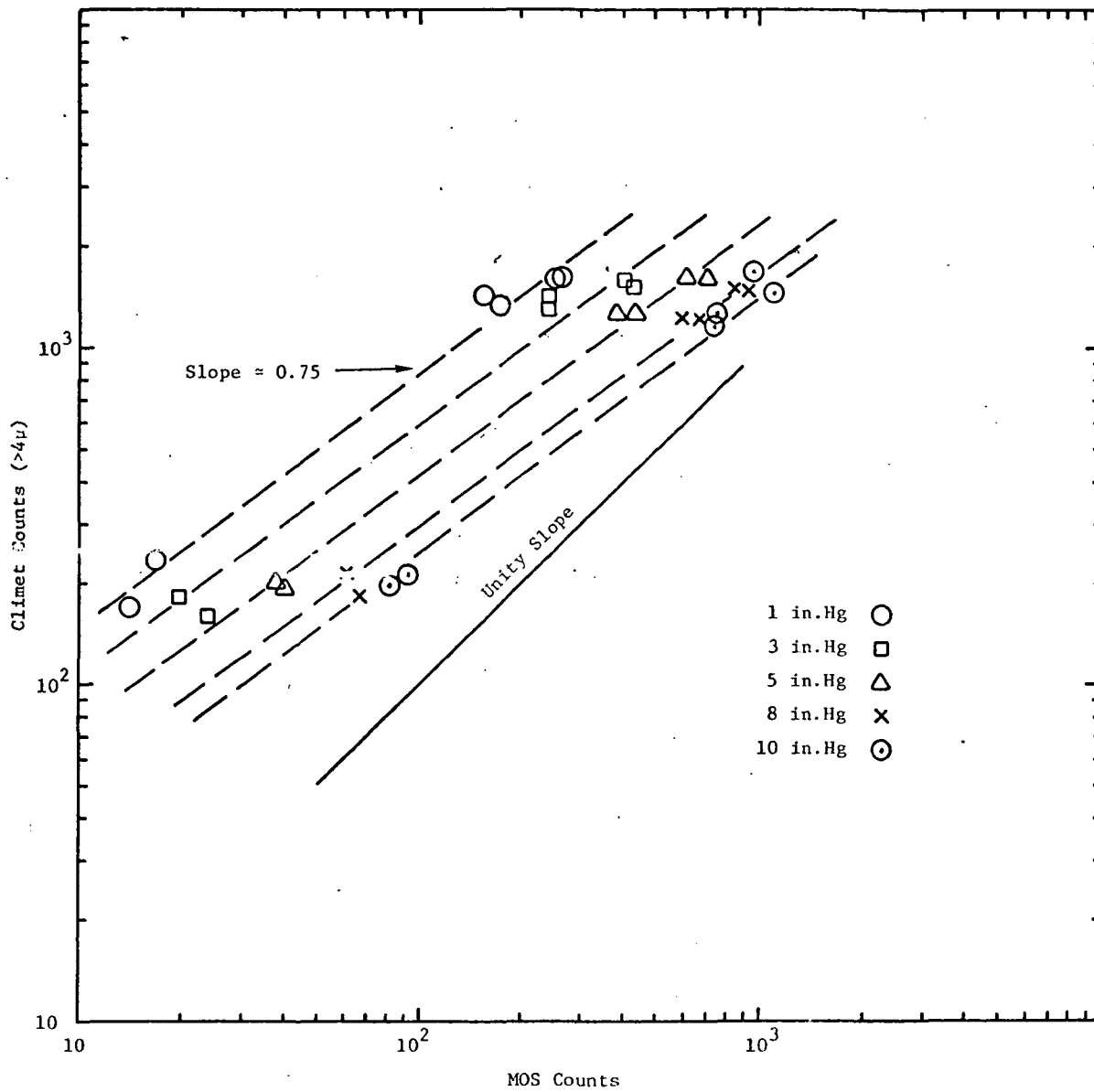


Figure 45. Correlation Between Climet and MOS (700 Å SiO₂)

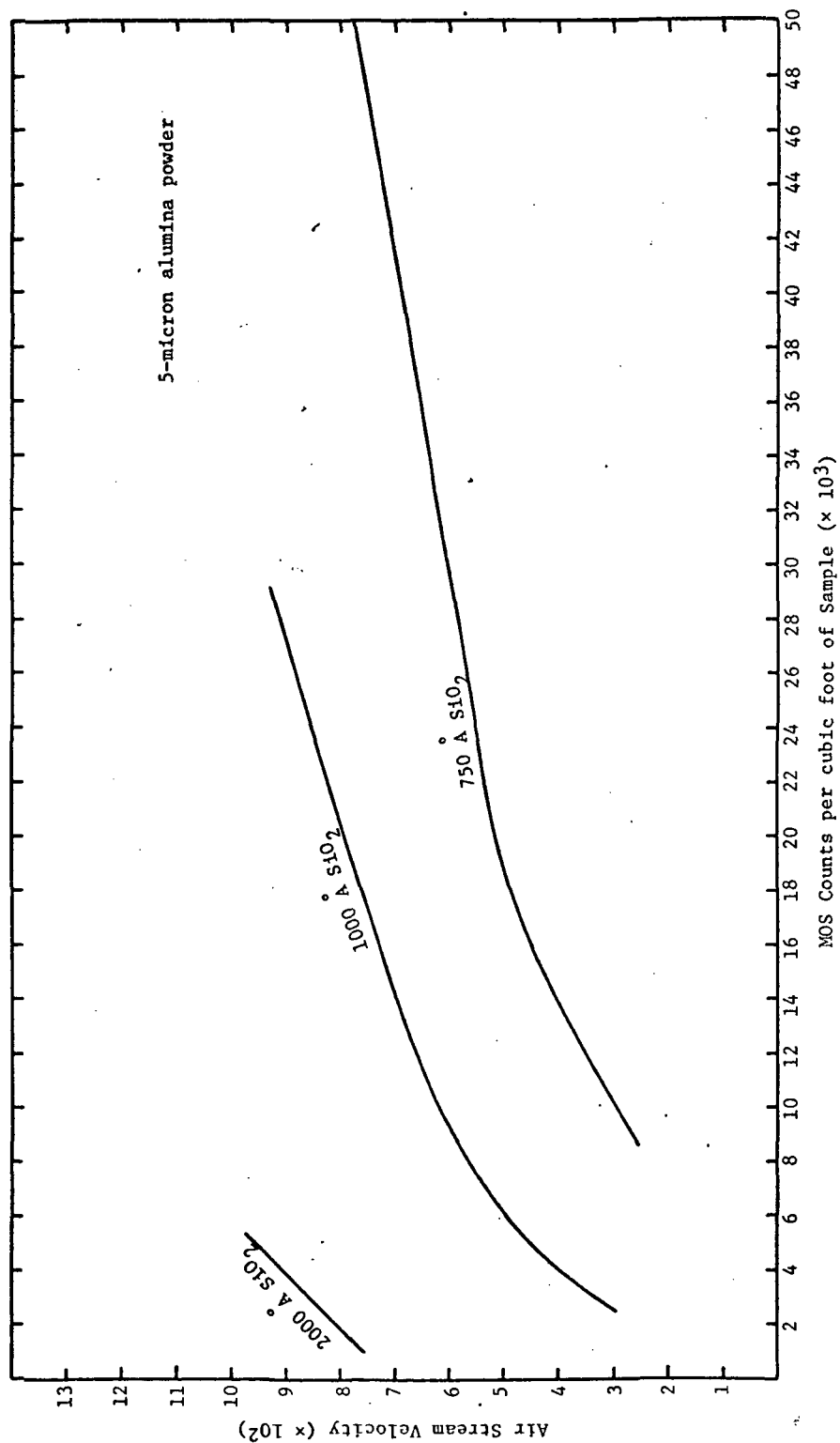


Figure 46. MOS Counts with Changes in Air Stream Velocity

A simple model to illustrate the threshold effect and change in MOS counts with changes in air stream velocity utilizes a correlation between particle momentum and MOS capacitor discharge. Assume that the particles to be sampled and accelerated to sonic velocities are given by Figure 47. In addition, assume that all sampled particles are accelerated to the air stream velocity. Using the assumption that a momentum threshold $P_T = M_T V_T$ must be exceeded by an impacting particle before the capacitor will discharge, the number of MOS counts (C_t) per second is given by

$$C_t = K N_o A M_T (V - V_T).$$

where A is the active area of the MOS unit, K is the counting efficiency for the particles and depends on the threshold momentum. Thus the MOS count should increase linearly with velocity with a slope

$$\frac{dC_t}{dV} = K N_o A M_T.$$

Obviously, the process leading to the results in Figure 46 are not properly described by this simple model. However, it is worth noting that the counting efficiency in Figure 46 increases with decreasing SiO_2 thickness and that the slope, $\frac{dC}{dV}$, approaches a constant as velocity increases. Whether a momentum mechanism can adequately explain these observations is yet unanswered.

Finally, it should be noted that the MOS counts show no indication of saturating with increasing air stream velocity. Obviously, the number of counts per cubic foot of sampled environment should not exceed the number of micro-particles in the sampled volume. In most instances, the MOS count is less than the number of 4- ∞ micron diameter particles sampled by the Climet. However, as the velocity increases, the MOS counts do exceed in some instances the Climet counts in the 4- ∞ micron ranges. Therefore, one may conclude that the threshold is also a function of air stream velocity and that particles less than 4 microns in diameter are counted at the highest velocities but with less efficiency.

Conclusion

Regarding calibration for the MOS capacitor, a complete understanding either phenomenologically or physically has not been obtained. However, attributes of the calibration have been identified. For hypervelocity particles and thick oxides, there is a bias-dependent discharge characteristic; hence, calibration can depend on the bias applied to the MOS unit. In addition, there appears to be an SiO_2 -thickness dependence in the ability

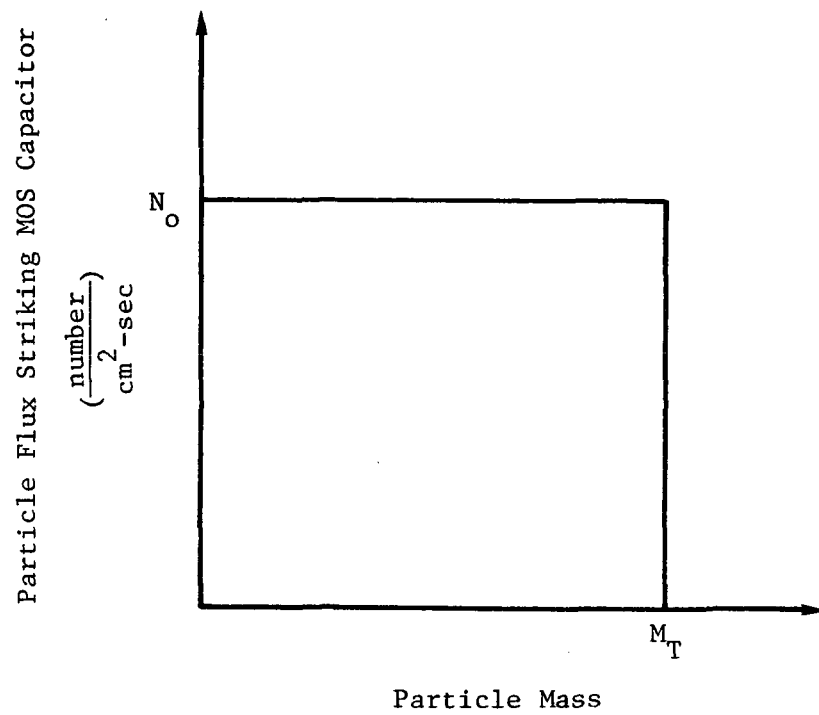


Figure 47. Particle Distribution for Momentum Threshold Model

of hypervelocity particles less than 10 microns in diameter to initiate MOS capacitor discharge. At least the 40,000 Å SiO_2 unit did not count the particles available at Goddard. It is still uncertain whether penetration-type calibration will apply to the oxides thicker than 10,000 Å. For thinner oxides near 1000 Å SiO_2 , a threshold effect has been observed.

However, uncertainties about the particle size distribution preclude a penetration-type analysis at this time. Tentatively it appears that the threshold is particle velocity dependent; however, an increase in counts with velocity indicates a particle size dependence as well. In fact, the results indicate that particles with less than a 4-micron diameter are not counted very efficiently by the MOS units tested to date.

REFERENCES

1. Parker, C. D. "Evaluation of a Gas Discharge Transducer and Associated Instrumentation for the Asteroid Belt Meteoroid Experiment," NASA Contract No. NASA CR-111848. Research Triangle Institute, Research Triangle Park, N.C. 27709 (Feb. 1971).
2. Parker, C. D. "Experimental Program to Determine Pressure Transducers," NASA Contract No. NASA CR-112273. Research Triangle Institute, Research Triangle Park, N.C. 27709 (Jan. 1973).
3. Private communication with Langley Research Center personnel.

APPENDIX A

Data from Hypervelocity Impact Studies at Goddard Space Flight Center

Sensor	Run	Discharge	Particle	Diameter micron	Mass 10 ⁻¹² gms	Velocity km/sec	m × v 10 ⁻⁷ gm-cm sec	$\frac{1}{2} mv^2$ 10 ⁻⁷ ergs	Bias Volts	Signal Volts
Sensor No. 9 [4000 Å SiO ₂ , 2000 Å Al, cleared to 100 volts]	178	S	P	CALIBRATION					40	
	179	S	P	1.17	6.49	3.17	20.57	32.61	40	27
	180	N	U	1.88	27.10	2.4	65.04	78.05	40	
	181	S	P	1.01	4.21	3.94	16.59	32.70	40	
	182	S	P	1.57	15.94	2.83	45.11	63.83	40	28.0
	183	S	P	2.12	38.70	2.64	95.20	125.66	40	28.0
	184	N	P	2.67	77.75	2.86	222.37	317.99	25	
	185	N	P	3.38	158.3	2.32	367.26	426.02	25	
	186	N	P	1.66	18.64	3.40	63.38	107.75	25	
	187	N	P	2.25	46.55	2.14	99.617	106.59	25	
	188	N	P	1.09	5.28	3.41	16.58	28.27	25	
	189	N	P	0.64	1.08	6.59	7.12	23.46	25	
	190	S	P	1.37	10.56	4.65	49.10	114.16	25	12
	191	S	P	0.97	3.77	4.32	16.29	70.38	25	
	192	N	P	0.63	1.04	4.35	4.52	9.83	25	
	193	N	P	0.66	1.17	4.42	5.17	11.43	25	
	194	S	P	1.14	6.09	3.45	21.01	36.25	25	9
	195	S	P	0.65	1.11	4.91	5.45	13.38	25	9
Sensor No. 21 [40,000 Å SiO ₂ , 1000 Å Al, cleared to 300 volts]	196	N	U	0.46	0.39	5.90	2.30	6.785	150	
	197	N	P	1.30	8.97	2.86	25.65	36.68	150	
	198	N	P	1.10	5.40	3.61	19.49	35.18	150	
	199	N	P	0.63	1.01	5.59	5.65	15.80	150	
	200	N	P	1.55	15.14	0.86	13.02	5.60	150	
	201	N	P	1.28	8.54	3.19	27.24	43.45	250	
	202	N	P	2.45	60.29	2.52	151.83	191.31	250	
	203	N	P	0.64	1.09	4.09	4.46	9.12	250	
	204	N	U	0.40	0.26	8.09	2.10	8.50	250	
<div> <div>S - discharge signal</div> <div>N - no discharge signal</div> <div>P - particle identified</div> <div>U - particle uncertain</div> </div>										

APPENDIX A (continued)

Sensor	Run	Discharge	Particle	Diameter micron	Mass 10 ⁻¹² gms	Velocity km/sec	$m \times v$ 10 ⁻⁷ gm-cm/sec	$\frac{1}{2} mv^2$ 10 ⁻⁷ ergs	Bias Volts	Signal Volts
Sensor No. 21 (continued)	205	FAULT								
	206	N	P	0.19	0.03	19.19	0.5757	5.53	250	
	207	N	P	0.25	0.07	11.09	0.7763	4.31	300	
	208	N	P	0.41	0.29	8.09	2.35	9.49	300	
	209	FAULT		0.31	0.12	8.61	1.03	1.033	300	
	210	N	P	1.39	11.07	1.90	10.52	4.45	300	
	211	N	P	3.26	141.1	2.48	350.00	434	300	
	212	N	P	3.31	148.5	1.99	295.5	294.04	300	
	213	N	P	3.43	165.4	1.84	304.34	278.99	400	
	214	N	P	1.77	22.69	3.09	70.12	108.33	400	
	215	N	U	1.15	6.28	3.76	23.62	44.27	400	
	216	N	P	1.17	6.56	3.29	21.60	35.50	400	
	217	N	P	2.07	36.33	2.89	104.99	151.72	400	
	218	N	P	1.24	7.81	3.09	24.14	37.29	500	
	219	N	P	1.24	7.76	3.69	28.64	52.83	500	
	220	N	P	0.81	2.15	4.22	9.07	19.15	500	
	221	N	P	0.87	2.70	3.45	9.315	16.07	500	
	222	N	P	1.39	10.91	3.25	35.46	57.62	500	
	223	N	U	FAULT					600	
	224	N	U	FAULT					600	
	225	N	P	0.78	1.92	3.99	7.66	15.29	600	
Sensor No. 19 [20,000 A SiO ₂ , 1000 A Al, cleared to 300 volts]	226	N	P	1.09	5.32	4.33	23.04	49.9	600	
	227	N	P	1.67	18.95	2.96	56.10	83.02	600	
	228	N	P	1.24	7.73	3.09	23.89	36.91	600	
	229	N	U	0.59	0.85	3.79	3.22	6.11	600	
	230	N	P	1.29	8.79	3.89	34.20	66.51	600	
	231	S	P	NO DATA						
	232	FAULT		NO DATA						
	233	N	U	NO DATA					300	
	234	N	P	NO DATA					300	
	235	N	P	NO DATA					300	

APPENDIX A (continued)

Sensor	Run	Discharge	Particle	Diameter micron	Mass 10^{-12} gms	Velocity km/sec	$m \times v$ $10^{-7} \frac{gm-cm}{sec}$	$\frac{1}{2} mv^2$ 10^{-7} ergs	Bias Volts	Signal Volts
Sensor No. 19 (continued)	236	N	U	NO DATA					300	
	237	N	U	NO DATA					300	
	238	N	P	NO DATA					300	
	239	N	U	0.67	1.22	4.64	5.66	13.13	300	
	240	N	P	NO DATA					300	
	241	N	P	2.15	40.63	2.59	105.23	136.27	300	
	242	N	U	0.59	0.85	5.49	4.67	12.81	300	
	243	N	P	1.19	6.83	4.99	34.08	85.034	300	
	244	N	P	2.30	49.93	2.79	139.30	194.33	300	
	245	N	P	1.90	28.14	2.91	81.89	119.15	400	
	246	N	U	NO DATA					400	
	247	N	P	0.96	3.61	3.41	12.30	20.99	400	
	248	N	P	0.17	0.02	21.39	0.428	4.58	400	
	249	S	P	0.58	0.81	6.39	5.18	16.55	400	
	250	N	P	1.53	14.56	3.60	52.42	94.35	400	
	251	N	P	1.80	23.98	3.49	83.70	146.04	400	
	252	N	U	1.66	18.80	3.69	69.37	127.99	400	
	253	S	U	1.73	21.26	3.44	73.14	125.80	400	
	254	FAULT		NO DATA					400	
	255	S	U	NO DATA					400	
	256	S	P	NO DATA					400	
	257	FAULT		FAULT					400	
	258	S	P	NO DATA					200	
	259	S	P	NO DATA					200	
	260	N	P	1.78	23.08	3.23	74.55	120.40	200	
	261	N	P	1.76	22.40	3.03	67.87	102.83	200	
	262	N	P	1.58	16.01	3.53	56.52	99.75	200	
	263	N	U	1.68	19.39	3.29	63.80	104.94	200	
	264	N	P	2.11	38.39	2.64	101.35	133.78	200	
	265	S	P	1.01	4.17	4.35	18.14	39.45	200	

APPENDIX A (continued)

Sensor	Run	Discharge	Particle	Diameter micron	Mass 10^{-12} gms	Velocity km/sec	$m \times v$ $10^{-7} \frac{gm-cm}{sec}$	$\frac{1}{2} \frac{mv^2}{10^{-7} \text{ ergs}}$	Bias Volts	Signal Volts
Sensor No. 19 (continued)	266	N	P	0.69	1.33	4.05	5.39	10.91	200	
	267	S	P	1.26	8.08	4.39	35.47	77.86	500	
	268	N	U	0.76	1.79	3.59	6.43	11.54	500	
	269	S	P	NO DATA					550	
	270	N	U	0.92	3.17	3.79	12.01	22.77	550	
	271	S	P	NO DATA					550	
	272	N	U	0.73	1.56	4.73	7.38	17.45	550	
	273	S	P	NO DATA					550	
	274	N	U	3.69	8.72	3.69	32.18	59.40	550	
	275	FAULT							32	
Sensor No. 24 [4000 Å SiN_3 , 500 Å Al, cleared to 100 volts]	276	NO DATA							32	
	277	NO DATA							32	
	278	NO DATA							32	
	279	NO DATA							32	
	280	N	U	4.89	1.27	4.89	6.21	15.2	32	
	281	N	U	3.13	10.88	3.13	34.05	53.29	32	
	282	S	P	3.42	9.20	3.42	31.46	53.8	32	
	283	S	P	4.33	2.61	4.33	11.30	24.47	32	
	284	S	P	3.01	15.42	3.01	46.42	69.85	32	
	285	S	P	3.35	11.16	3.35	37.35	62.57	32	
	286	S	P	3.12	4.80	3.12	14.98	23.37	32	18
	287	N	P	1.42	11.79	3.54	41.74	73.87	32	
	288	N	P	1.36	12.78	3.29	42.04	69.17	32	
	289	S	P	0.72	1.55	5.29	8.20	21.69	32	20
	290	S	U	1.85	25.66	3.09	79.29	122.50	32	
	291	S	P	1.41	11.56	3.04	35.14	53.42	32	20
	292	S	P	1.00	4.09	4.12	16.85	34.71	32	
	293	S	P	1.51	13.96	3.89	54.33	105.67	32	10
	294	N	U	0.58	0.80	8.02	6.42	25.73	32	
		N	P	0.63	1.03	5.09	5.24	13.34	32	
		N	P	2.13	39.41	3.49	137.54	240.0	32	

APPENDIX A (continued)

Sensor	Run	Discharge	Particle	Diameter micron	Mass 10^{-12} gms	Velocity km/sec	$m \times v$ $10^{-7} \frac{gm-cm}{sec}$	$\frac{1}{2} mv^2$ 10^{-7} ergs	Bias Volts	Signal Volts
Sensor No. 24 (continued)	295	S	P	0.62	0.98	6.49	6.36	20.64	32	9.5
	296	N	U	0.80	2.10	5.00	10.5	26.25	32	
	297	N	P	1.04	24.56	4.24	104.13	220.76	32	
	298	N	U	0.87	2.66	5.12	13.62	18.11	32	
	299	S	P	0.83	2.34	4.70	10.99	25.85	32	9.5
	300	N	P	1.14	5.99	4.35	26.06	56.67	32	
	301	N	U	0.62	0.96	6.59	6.33	20.85	32	
	302	N	U	0.66	1.19	5.54	6.60	18.26	32	
	303	S	P	0.97	3.68	4.19	15.42	32.30	32	10
	304	S	P	1.86	26.26	2.85	74.84	106.65	32	0.01
	305	S	P	2.12	38.71	2.80	108.39	151.74	32	0.01
Sensor No. 17 [10,000 Å SiO ₂ , 1000 Å Al, cleared to 160 volts]	32	N	U	1.20	6.98	3.79	26.45	50.12	60	
	33	N	U	2.76	85.96	1.87	160.74	150.30	60	
	34	S	P	2.98	108.50	2.32	251.72	291.99	60	
	35	S	P	1.04	4.61	3.09	14.25	22.01	60	
	36	S	P	1.01	4.20	4.29	18.02	38.65	60	
	37	S	P	0.95	3.49	4.02	14.03	28.20	60	44
	38	N	U	0.38	0.22	7.79	1.71	6.66	60	44
	39	S	P	0.83	2.37	5.34	12.66	33.79	60	44
	40	S	P	1.18	6.70	3.35	22.45	37.59	60	44
	41	S	P	2.44	59.34	1.79	106.22	95.07	60	
	42	S	P	0.89	2.87	5.39	15.47	41.69	60	44
	43	N	U	2.96	105.6	2.36	249.22	294.07	60	
	44	S	P	2.60	72.18	1.43	187.67	134.18	60	
	45	S	P	0.63	1.00	4.09	4.09	8.364	60	
	46	S	P	NO DATA					60	
	47	S	P	0.74	1.64	3.94	6.46	12.73	60	
	48	S	P	NO DATA					60	44
	49	N	U	0.20	0.03	19.29	0.5787	5.58	60	
	50	S	P	0.81	2.15	5.35	11.50	30.77	60	

APPENDIX A (continued)

Sensor	Run	Discharge	Particle	Diameter micron	Mass 10^{-12} gms	Velocity km/sec	$m \times v$ $10^{-7} \frac{gm-cm}{sec}$	$\frac{1}{2} mv^2$ 10^{-7} ergs	Bias Volts	Signal Volts
Sensor No. 17 (continued)	51	N	U	0.47	0.41	7.39	3.03	22.40	60	
	52	N	U	0.62	0.96	5.49	5.27	28.94	60	
	53	N	P	1.46	12.67	3.05	38.64	58.93	25	
	54	N	U	1.65	18.33	3.44	63.06	108.46	25	
	55	N	U	0.87	2.67	3.53	9.425	16.635	25	
	56	N	U	1.37	10.39	3.12	32.42	50.57	25	
	57	N	U	0.50	0.51	4.49	2.29	5.140	25	
	58	N	P	1.42	11.58	3.26	37.75	61.53	25	
	59	N	P	2.18	42.28	2.77	117.12	162.20	25	
	60	S	P	0.76	1.82	5.14	9.36	24.04	25	7
	61	N	P	1.88	26.93	3.09	83.21	128.57	25	
	62	N	U	0.95	3.49	2.87	10.01	28.99	25	
	63	N	P	2.18	42.45	2.65	112.50	149.05	25	
	64	N	P	0.40	0.25	7.39	1.85	6.83	25	
	65	N	U	0.63	1.00	6.79	6.79	23.05	25	
	66	N	P	1.37	10.48	2.46	25.78	31.71	25	
	67	S	P	0.53	0.62	5.80	3.597	10.42	25	9
	68	N	U	2.05	35.12	4.05	142.24	288.03	30	
	69	N	U	2.08	36.73	2.21	81.17	89.67	30	
	70	N	U	1.48	13.34	3.79	50.56	98.80	30	
	71	S	P	1.28	8.65	3.19	27.59	44.01	30	
	72	S	U	2.68	78.94	2.72	214.72	292.01	30	
	73	N	U	0.91	3.09	4.65	14.37	33.41	30	
	74	N	U	1.01	4.17	3.20	13.34	21.35	30	
	75	S	P	1.05	4.75	4.42	20.995	46.40	30	14
Sensor No. 42 [10,000 Å SiO ₂ , 570 Å Au, cleared to 100 volts]	76	S	P	1.63	17.82	2.51	44.73	56.13	60	48
	77	N	U	1.67	19.02	2.19	41.65	45.61	60	
	78	S	P	0.87	2.65	3.35	8.88	14.87	60	36
	79	S	P	NO DATA					60	44
	80	S	P	1.18	6.69	5.42	36.26	98.26	60	46

APPENDIX A (continued)

Sensor	Run	Discharge	Particle	Diameter micron	Mass 10 ⁻¹² gms	Velocity km/sec	m x v 10 ⁻⁷ gm-cm sec	$\frac{1}{2} mv^2$ 10 ⁻⁷ ergs	Bias Volts	Signal Volts
Sensor No. 42 (continued)	81	S	P	1.27	8.45	3.89	32.87	63.93	60	46
	82	N	P	0.78	1.97	3.01	5.93	8.92	60	
	83	S	P	2.75	84.97	2.71	230.269	312.014	60	
	84	N	U	0.60	0.90	5.53	4.98	13.77	60	
	85	S	P	NO DATA					60	46
	86	S	P	2.11	38.11	2.12	80.80	85.64	60	
	87	N	U	1.70	20.17	0.86	17.34	7.46	60	
	88	S	P	NO DATA					60	
	89	N	U	NO DATA					25	
	90	N	U	2.64	75.48	1.44	108.70	78.26	25	
	91	N	U	0.15	0.01	23.69	0.236	2.81	25	
	92	N	U	0.49	0.48	5.49	2.64	7.25	25	
	93	N	P	1.12	5.75	3.15	18.11	28.53	25	
	94	N	U	0.43	0.32	5.79	1.85	5.36	25	
	95	N	U	1.30	9.00	3.02	27.18	41.04	25	
	96	N	P	0.59	0.85	5.30	4.50	11.94	25	
	97	S	P	1.24	7.79	3.89	30.30	58.94	25	
	98	S	P	1.01	4.17	3.65	15.22	27.78	25	8
	99	N	U	0.48	0.44	4.82	2.12	5.11	25	
	100	N	P	1.04	4.55	1.64	7.46	6.11	25	
	101	N	P	0.78	1.92	4.89	9.39	22.96	25	
	102	N	U	0.75	1.73	5.41	9.36	25.32	25	
	103	N	P	1.05	4.75	3.99	18.95	37.81	25	
	104	N	U	1.95	3.04	2.94	8.94	26.30	25	
	105	S	P	1.60	16.76	2.90	48.60	70.48	25	
	106	N	U	1.73	21.19	3.29	69.72	114.68	25	
	107	N	P	1.69	19.61	3.14	61.58	96.67	25	
	108	N	P	0.74	1.65	5.09	8.40	21.37	25	
	109	S	P	0.56	0.72	7.39	5.32	19.66	25	
	110	N	U	1.07	5.00	4.43	22.15	49.06	25	
	111	S	P	0.90	2.98	4.82	14.36	34.60	25	

APPENDIX A (continued)

Sensor	Run	Discharge	Particle	Diameter micron	Mass 10^{-12} gms	Velocity km/sec	$m \times v$ $10^{-7} \frac{\text{gm-cm}}{\text{sec}}$	$\frac{1}{2} \frac{\text{mv}^2}{10^{-7} \text{ ergs}}$	Bias Volts	Signal Volts
Sensor No. 42 (continued)	112	N	U	0.45	0.37	4.79	1.77	4.25	25	
	113	N	U	0.38	0.23	6.79	1.56	5.30	25	
	114	N	U	1.25	7.97	3.70	28.82	53.32	25	
	115	N	U	NO DATA					25	
	116	S	P	2.26	47.12	1.92	90.47	86.85	25	
	117	N	U	0.75	1.73	5.49	9.49	26.07	25	
	118	N	U	1.25	7.99	3.11	24.85	38.64	25	
	119	S	P	1.45	12.43	2.79	34.68	48.38	25	
	120	FAULT							25	
	121	S	P	1.13	5.85	3.92	22.93	44.95	60	
	122	N	U	2.21	44.06	2.25	99.14	111.53	60	
	123	S	P	1.45	12.35	2.73	33.72	46.02	60	
Sensor No. 11 [10,000 Å SiO ₂ , 2000 Å Al, cleared to 160 volts]	124	N	U	1.20	7.00	3.80	26.6	50.54	60	46
	125	S	P	NO DATA					60	
	126	N	U	2.89	98.10	2.87	281.55	404.01	60	
	127	S	P	2.12	38.77	2.71	105.07	142.37	60	
	128	N	U	2.80	89.53	1.63	145.94	118.94	60	
	129	S	P	1.54	14.83	3.49	51.76	90.32	60	44
	130	S	P	NO DATA					60	46
	131	S	P	1.31	9.10	2.66	24.20	32.20	60	44
	132	S	P	2.10	37.95	2.94	111.60	164.01	60	44
	133	S	P	2.10	37.67	2.59	97.57	126.35	60	48
	134	S	P	NO DATA					60	
	135	N	U	0.81	2.15	3.09	6.64	10.26	25	
	136	N	U	0.83	2.32	4.80	11.14	26.73	25	
	137	S	P	0.78	1.92	4.99	9.58	23.90	25	8.5
	138	N	P	2.10	37.94	2.92	110.79	161.75	25	
	139	N	U	1.83	24.92	3.66	91.21	106.91	25	
	140	N	P	1.32	9.34	2.66	24.8	33.04	25	
	141	N	P	1.95	30.16	2.30	69.37	79.77	25	

APPENDIX A (continued)

Sensor	Run	Discharge	Particle	Diameter micron	Mass 10^{-12} gms	Velocity km/sec	$m \times v$ $10^{-7} \frac{gm-cm}{sec}$	$\frac{1}{2} mv^2$ 10^{-7} ergs	Bias Volts	Signal Volts
Sensor No. 11 (continued)	142	S	P	1.12	5.76	4.06	23.39	47.47	25	9
	143	N	P	2.31	50.36	2.27	114.32	129.75	25	
	144	N	P	1.83	25.05	3.20	80.15	128.26	25	
	145	N	U	1.05	4.79	4.89	23.42	57.27	25	
	146	N	P	1.26	8.08	3.46	27.96	48.37	25	
	147	N	P	1.37	10.53	3.01	31.69	95.40	25	
	148	N	P	1.95	30.12	2.89	87.04	125.78	25	
	149	N	U	1.50	13.89	1.20	16.67	10.0	25	
	150	S	P	0.81	2.15	3.69	7.93	14.64	25	
	151	N	U	1.56	15.48	3.23	50.0	80.75	25	
	152	S	P	2.11	38.25	2.30	87.98	101.17	25	0.03
	153	S	P	1.76	22.17	3.23	71.61	115.65	60	44
	154	N	U	0.66	1.18	6.03	7.12	21.45	60	
	155	N	U	0.41	0.28	5.79	1.62	4.69	60	
Sensor No. 5 [10,000 Å SiO ₂ , 500 Å Al, cleared to 160 volts]	156	S	P	1.95	30.29	3.45	104.5	180.26	60	44
	157	N	U	0.67	1.20	3.95	4.74	9.36	60	
	158	N	U	1.15	6.27	0.86	5.39	2.32	60	
	159	N	U	0.99	4.01	3.74	14.99	28.05	60	
	160	S	P	1.61	17.13	2.93	50.19	73.53	60	44
	161	N	U	0.62	1.0	4.69	4.69	10.99	60	
	162	S	P	0.93	3.32	3.40	11.29	19.20	60	46
	163	S	P	1.04	4.59	2.49	11.43	14.23	60	
	164	S	P	1.75	21.90	3.04	66.57	101.20	60	40
	165	S	P	3.23	137.3	2.39	328.15	392.14	60	
	166	S	P	1.14	6.01	4.33	26.02	56.34	60	
	167	N	U	2.52	65.12	2.44	158.90	193.85	60	
	168	S	P	2.56	68.39	2.39	163.45	195.33	60	
	169	N	U	0.72	1.55	3.71	5.75	10.67	60	
	170	S	P	0.73	1.57	6.44	10.11	32.56	60	
	171	N	P	1.75	21.89	2.40	52.54	63.04	25	

APPENDIX A (continued)

Sensor	Run	Discharge	Particle	Diameter micron	Mass 10^{-12} gms	Velocity km/sec	$m \times v$ $10^{-7} \frac{gm-cm}{sec}$	$\frac{1}{2} mv^2$ 10^{-7} ergs	Bias Volts	Signal Volts
Sensor No. 5 (continued)	172	N	P	0.62	0.98	5.23	5.125	13.40	25	
	173	N	P	1.59	16.54	3.36	55.60	93.36	25	
	174	N	P	1.43	11.97	3.19	38.18	60.90	25	
	175	N	U	2.05	35.38	3.15	111.45	175.53	25	
	176	N	U	1.19	6.92	3.60	24.91	44.84	25	
	177	N	P	1.66	18.63	3.13	58.31	91.26	25	
	178	N	P	1.39	11.01	2.90	31.93	46.30	25	
	179	N	P	1.50	13.85	3.39	46.95	79.58	25	
	180	N	P	1.74	21.65	3.19	69.07	110.16	25	
	181	N	P	NO DATA					25	
	182	N	P	2.01	32.94	3.06	100.80	154.22	25	
	183	N	U	0.60	0.88	5.59	4.92	13.75	25	
	184	N	U	0.62	0.98	6.05	5.93	17.58	25	
	185	N	P	0.62	0.99	5.70	5.64	16.08	25	
	186	S	P	1.45	12.48	3.79	47.30	89.63	25	
	187	N	P	1.61	17.01	3.19	54.26	86.55	25	
	188	N	P	1.32	9.47	3.49	33.05	57.67	25	
	189	S	P	1.34	9.85	3.12	30.73	47.94	25	0.01
	190	N	P	1.12	5.77	3.61	20.83	37.60	25	
	191	S	P	0.60	0.89	5.29	4.71	12.46	25	